

UNIVERSITY OF CALGARY

Flat Lenses for Circularly Polarized Electromagnetic Waves

by

Rudi Henry Phillion

A THESIS

SUBMITTED TO THE FACULTY OF GRADUATE STUDIES
IN PARTIAL FULFILMENT OF THE REQUIREMENTS FOR THE
DEGREE OF DOCTOR OF PHILOSOPHY

DEPARTMENT OF ELECTRICAL AND COMPUTER
ENGINEERING

CALGARY, ALBERTA

DECEMBER, 2010

© Rudi Henry Phillion 2010



UNIVERSITY OF
CALGARY

The author of this thesis has granted the University of Calgary a non-exclusive license to reproduce and distribute copies of this thesis to users of the University of Calgary Archives.

Copyright remains with the author.

Theses and dissertations available in the University of Calgary Institutional Repository are solely for the purpose of private study and research. They may not be copied or reproduced, except as permitted by copyright laws, without written authority of the copyright owner. Any commercial use or re-publication is strictly prohibited.

The original Partial Copyright License attesting to these terms and signed by the author of this thesis may be found in the original print version of the thesis, held by the University of Calgary Archives.

Please contact the University of Calgary Archives for further information:

E-mail: uarc@ucalgary.ca

Telephone: (403) 220-7271

Website: <http://archives.ucalgary.ca>

Abstract

A planar array of passive lens elements can be phased to approximate the effect of a curved dielectric lens. The rotational orientation of each element can provide the required phase shift for circular polarization. The array elements must be designed so that the hand of circular polarization changes as the electromagnetic wave passes through the lens. An element is presented that is based on an aperture-coupled microstrip patch antenna. Two lenses are designed; both operate in the Ku-band, have a diameter of 254 mm, and contain 349 lens elements. The elements have identical dimensions but the rotational orientation of each element is selected to provide a specific lens function. The first lens is designed to collimate radiation from a feed horn into a beam pointing 20° from broadside. The measured aperture efficiency is 48%, the cross-polarization discrimination ratio is 20 dB, and the -3 -dB-gain bandwidth is 17%. A simulation technique that assumes local periodicity for each element is used to predict the antenna performance. Guidelines are given for predicting the radiation pattern, gain, bandwidth, and cross-polarization discrimination ratio of a much larger array. The second lens acts as a Wollaston-type prism. It splits an incident wave according to its circular polarization components. The prism effect occurs because of the equal but opposite phase shifts applied to each hand of incident circular polarization.

Acknowledgements

I would like to thank all members of the Applied Electromagnetics Group for encouraging me throughout my studies. Special thanks are given to my supervisor, Michal Okoniewski, for his guidance, as well as to Greg McFeetors, Yen Ong, Adrian Sutinjo, Jeremie Bourqui, Billy Wu, Andrea Dukeshire, and Trevor Cameron for their keen interest in my work. I would also like to thank the following organizations for providing scholarships, which were awarded to me during my post-graduate studies: Alberta Ingenuity Fund, the Natural Sciences and Engineering Research Council of Canada, Alberta Informatics Circle of Research Excellence, Bell Canada, University of Calgary Faculty of Graduate Studies, the IEEE Antennas and Propagation Society, and Alberta Advanced Education and Technology.

Table of Contents

Abstract	ii
Acknowledgements	iii
Table of Contents	iv
List of Tables	vii
List of Figures	viii
List of Abbreviations and Symbols	x
1 Introduction	1
1.1 Motivation and Applications	1
1.2 Thesis Goals	3
1.3 Thesis Contributions	4
1.4 Layout of the Thesis Document	5
2 Applicable Theory	6
2.1 Horn Antennas as Spatial Feeds	6
2.1.1 Spillover and Taper Efficiencies	7
2.2 Array Antennas	10
2.3 Space-Fed Array Antennas	11
2.3.1 Array Lenses and Reflectarrays	12
2.3.2 Radiation Pattern of Space-Fed Arrays	13
2.3.3 Spillover and Taper Efficiency of Space-Fed Arrays	16
2.3.4 Bandwidth of Space-Fed Arrays	17
2.4 Lens Antennas	20
2.4.1 Dielectric Lenses	20
2.4.2 Bootlace Lens	21
2.4.3 Waveguide Lenses	22
2.5 Aperture-Coupled Microstrip Patch Antennas	23
2.5.1 Aperture-Coupled Elements for Space-Fed Antennas	24
2.6 Wollaston Prism	25
2.7 Floquet Modal Analysis	26
2.7.1 Computational Floquet Analysis	28
2.7.2 Four Element Floquet Analysis	30
2.8 Chapter Summary	32

3	Review of Relevant Literature	33
3.1	Array Lenses	33
3.1.1	Array Lenses Using Element Rotation	34
3.1.2	Array Lenses for Linear Polarization	36
3.2	Reflectarrays Using Element Rotation	38
3.3	Other Similar Configurations	39
3.4	Chapter Summary	41
4	Analysis and Design of a Circularly Polarized Array Lens Element	44
4.1	Using Rotation to Alter Transmission Phase	45
4.1.1	Scattering Parameters of a Rotated Array Lens Element	46
4.1.2	Ideal Phase-Shifting Element Characteristics	50
4.1.3	Practical Element Characteristics	51
4.1.4	From Scattering Parameters to Array Weights	52
4.1.5	Scattering Parameters of a Rotated Reflectarray Element	53
4.1.6	Element Factor	54
4.2	Element Bandwidth	55
4.2.1	Rotated Reflectarray Element Bandwidth	56
4.2.2	Reflectarray Element Bandwidth Simulation	59
4.2.3	Rotated Array Lens Element Bandwidth	63
4.3	Aperture-Coupled Stacked-Patch Element	64
4.3.1	Patch Element Transmission Bandwidth	65
4.3.2	Patch Element Phase Bandwidth	67
4.3.3	Effect of Incidence Angle	71
4.3.4	Effect of Rotation in a Fixed Array Lattice	72
4.3.5	Tolerance to Fabrication Errors	73
4.3.6	Patch Element Design Process	74
4.4	Four-Element Periodic Array Lens Simulation	77
4.4.1	$a_1^{r(0,0)}$ Incidence	80
4.4.2	$a_1^{r(+1,0)}$ Incidence	82
4.4.3	$a_1^{r(-1,0)}$ Incidence	84
4.5	Chapter Summary	85
5	Design, Modeling, and Measurement of Two Prototype Lenses	89
5.1	Modified Convex Lens Prototype	90
5.1.1	Antenna Simulation	92
5.1.2	Radiation Pattern Calculation	93
5.1.3	Aperture Efficiency Calculation	96
5.1.4	Cross Polarization Selectivity	99
5.1.5	Prototype Bandwidth	101

5.1.6	Antenna Measurements	101
5.1.7	Extrapolating to Larger Arrays	107
5.2	Wollaston-Type Prism	108
5.2.1	Radiation Pattern Measurement	110
5.3	Chapter Summary	113
6	Future Work, Contributions, and Conclusion	116
6.1	Future Work	116
6.2	Goals and Contributions	119
6.3	Conclusion	122
	Bibliography	124

List of Tables

3.1	Measured antenna performance published in literature	43
4.1	Range of phase difference for common bandwidth criteria	59
4.2	Reflectarray element parameters for $1/4$ wavelength separation	59
4.3	Reflectarray element parameters for $3/8$ wavelength separation	60
4.4	Reflectarray element parameters for $1/8$ wavelength separation	62
4.5	Parameter values of the aperture-coupled patch element	66
5.1	Calculated constituents of aperture efficiency	99

List of Figures

1.1	A lens antenna system	1
2.1	Illustration of the taper and spillover efficiencies	8
2.2	Conceptual array lens and reflectarray antennas	13
2.3	Wollaston prism	26
3.1	The array lens concept presented in this thesis	42
4.1	The coordinate system of the periodic array lens	47
4.2	Dipole and ground plane reflectarray element	57
4.3	Reflection phase using a $1/4$ wavelength separation	60
4.4	Circular polarization reflection magnitudes	61
4.5	Reflection phase using a $3/8$ wavelength separation	61
4.6	Reflection phase using a $1/8$ wavelength separation	62
4.7	Geometry of the aperture-coupled patch element	65
4.8	Variation of linear polarization coefficient magnitudes	67
4.9	Variation of linear polarization coefficient phases	69
4.10	Variation of the magnitude of four CP scattering parameters	70
4.11	Variation of the magnitude of S_{21}^{lr} with incidence angle	71
4.12	Variation of the phase of S_{21}^{lr} with incidence angle	72
4.13	Error between the phase of S_{21}^{lr} and the linear phase shift relationship	73
4.14	Variation of the magnitude and phase of S_{21}^{lr} due to fabrication errors	74
4.15	Configuration of the four-element simulation	78
4.16	The electric field in the four-element simulation: $a_1^{r(0,0)}$ incidence	81
4.17	Four Floquet mode magnitudes for $a_1^{r(0,0)}$ incidence	82
4.18	The electric field in the four-element simulation: $a_1^{r(+1,0)}$ incidence	83
4.19	Four Floquet mode magnitudes for $a_1^{r(+1,0)}$ incidence	84
4.20	The electric field in the four-element simulation: $a_1^{r(-1,0)}$ incidence	85
4.21	Six Floquet mode magnitudes for $a_1^{r(-1,0)}$ incidence	86
5.1	The entire Metal 2 layer of each lens	91
5.2	The modified convex lens and feed horn mounted in a plastic frame	92
5.3	Simulation of the lens when excited by the feed horn	97
5.4	Azimuth cut of the radiation pattern	103
5.5	Elevation cut of the radiation pattern	104
5.6	Reflection coefficient measured at the coax connector to the horn.	105
5.7	Measured beam direction and gain in that direction	106
5.8	Measured aperture efficiency and axial ratio	107

5.9	Beam splitting action of the array lens and Wollaston prism	109
5.10	Ray diagram representation of four scattering parameters	111
5.11	Wollaston-type prism array lens mounted in the anechoic chamber . .	112
5.12	Azimuth cut of the radiation pattern without the lens	113
5.13	Azimuth cut of the radiation pattern through the prism	114

List of Abbreviations and Symbols

Abbreviations

AAP	adaptive array processing
AESA	active electronically scanned array
AF	array factor
CP	circular polarization
DBS	direct broadcasting satellite
EF	element factor
FBA	fixed beam array
F/D	focal length to diameter ratio
IEEE	Institute of Electrical and Electronics Engineers
LCP	left-hand circular polarization
LP	linear polarization
MEMS	micro-electromechanical systems
PESA	passive electronically scanned array
PCB	printed circuit board
RCP	right-hand circular polarization
RF	radio frequency
TE	transverse electric
TEM	transverse electromagnetic
TM	transverse magnetic
T/R	transmit/receive
XPD	cross-polarization discrimination ratio

Symbols

A_i	total array weight
A_i^f	array weight due to the feed
A_i^e	array weight due to the element
$\angle A_i$	phase angle of the total array weight
$\angle A_{max}$	maximum acceptable phase difference between centre and edge elements
A_x	aperture length in x direction
A_y	aperture length in y direction
A_w	aperture width in both directions
B	fractional bandwidth
D	diameter
E	scalar electric field
\mathbf{E}	vector electric field
F	focal length
G	actual gain
G_{ap}	maximum gain of the aperture area
N	number of array elements
P_{inc}	power incident on the aperture
P_{rad}	radiated power
P_x	x dimension of the reflectarray's rectangular dipole
P_y	y dimension of the reflectarray's rectangular dipole
P_{x1}	x dimension of rectangular patch on the Metal 1 layer
P_{y1}	y dimension of rectangular patch on the Metal 1 layer
P_{x2}	x dimension of rectangular patch on the Metal 2 layer
P_{y2}	y dimension of rectangular patch on the Metal 2 layer
$\mathbf{R}_\psi^{\mathbf{XY}}$	matrix representing rotation about the z -axis by angle ψ
S_{11}^{lr}	scattering parameter: LCP at Port 1 due to RCP on Port 1
S_{11}^{rr}	scattering parameter: RCP at Port 1 due to RCP on Port 1
S_{21}^{lr}	scattering parameter: LCP at Port 2 due to RCP on Port 1
S_{21}^{rr}	scattering parameter: RCP at Port 2 due to RCP on Port 1
S_{11}^{ll}	scattering parameter: LCP at Port 1 due to LCP on Port 1
S_{11}^{rl}	scattering parameter: RCP at Port 1 due to LCP on Port 1
S_{21}^{ll}	scattering parameter: LCP at Port 2 due to LCP on Port 1
S_{21}^{rl}	scattering parameter: RCP at Port 2 due to LCP on Port 1
S_{12}^{lr}	scattering parameter: LCP at Port 1 due to RCP on Port 2
S_{12}^{rr}	scattering parameter: RCP at Port 1 due to RCP on Port 2
S_{22}^{lr}	scattering parameter: LCP at Port 2 due to RCP on Port 2
S_{22}^{rr}	scattering parameter: RCP at Port 2 due to RCP on Port 2

S_{12}^{ll}	scattering parameter: LCP at Port 1 due to LCP on Port 2
S_{12}^{rl}	scattering parameter: RCP at Port 1 due to LCP on Port 2
S_{22}^{ll}	scattering parameter: LCP at Port 2 due to LCP on Port 2
S_{22}^{rl}	scattering parameter: RCP at Port 2 due to LCP on Port 2
$\mathbf{S}^{\mathbf{XY}}$	scattering matrix without rotation in linear coordinates
$\mathbf{S}_{\psi}^{\mathbf{XY}}$	scattering matrix of rotated element in linear coordinates
$\mathbf{S}_{\psi}^{\mathbf{CP}}$	scattering matrix of rotated element in circular coordinates
$\mathbf{T}^{\mathbf{XY} \rightarrow \mathbf{CP}}$	coordinate transformation from linear to circular coordinates
T_x	transmission coefficient to incident x -polarization
T_y	transmission coefficient to incident y -polarization
$-T_x$	phase angle of T_x
$-T_y$	phase angle of T_y
$U(\theta, \psi)$	radiation intensity in the direction (θ, ψ)
U_f	radiation intensity of the feed
\mathbf{W}_f	radiation power density of the feed

$\mathbf{a}^{\mathbf{XY}}$	incident mode vector in linear coordinates
$\mathbf{a}^{\mathbf{CP}}$	incident mode vector in circular coordinates
a_1^x	mode incident on Port 1 in x -polarization
a_1^y	mode incident on Port 1 in y -polarization
a_2^x	mode incident on Port 2 in x -polarization
a_2^y	mode incident on Port 2 in y -polarization
a_1^l	mode incident on Port 1 in left-hand CP
a_1^r	mode incident on Port 1 in right-hand CP
a_2^l	mode incident on Port 2 in left-hand CP
a_2^r	mode incident on Port 2 in right-hand CP
$a_1^{l(m,n)}$	Floquet mode (m, n) incident on Port 1 in left-hand CP
$a_1^{r(m,n)}$	Floquet mode (m, n) incident on Port 1 in right-hand CP
$a_2^{l(m,n)}$	Floquet mode (m, n) incident on Port 2 in left-hand CP
$a_2^{r(m,n)}$	Floquet mode (m, n) incident on Port 2 in right-hand CP
$\mathbf{b}^{\mathbf{XY}}$	scattered mode vector in linear coordinates
$\mathbf{b}^{\mathbf{CP}}$	scattered mode vector in circular coordinates
b_1^x	mode scattered from Port 1 in x -polarization
b_1^y	mode scattered from Port 1 in y -polarization
b_2^x	mode scattered from Port 2 in x -polarization
b_2^y	mode scattered from Port 2 in y -polarization
b_1^l	mode scattered from Port 1 in left-hand CP
b_1^r	mode scattered from Port 1 in right-hand CP

b_2^l	mode scattered from Port 2 in left-hand CP
b_2^r	mode scattered from Port 2 in right-hand CP
$b_1^{l(m,n)}$	Floquet mode (m, n) scattered from Port 1 in left-hand CP
$b_1^{r(m,n)}$	Floquet mode (m, n) scattered from Port 1 in right-hand CP
$b_2^{l(m,n)}$	Floquet mode (m, n) scattered from Port 2 in left-hand CP
$b_2^{r(m,n)}$	Floquet mode (m, n) scattered from Port 2 in right-hand CP
c	speed of light
d_1	thickness of reflectarray dielectric layer
d_1	thickness of Dielectric 1 layer
d_2	thickness of Dielectric 2 layer
d_3	thickness of Dielectric 3 layer
$()_i$	array element index number
j	imaginary number
\mathbf{k}	wavenumber propagation vector
k_0	phase constant in free space
k_x	x -component of the phase constant
k_y	y -component of the phase constant
k_{xmn}	x -component of the phase constant of mode (m, n)
k_{ymn}	y -component of the phase constant of mode (m, n)
k_{zmn}	z -component of the phase constant of mode (m, n)
m	integer multiplier
n	integer multiplier
$\hat{\mathbf{n}}$	direction normal to the aperture surface
\mathbf{p}_i	element position vector
s	surface area of the aperture
u_x	separation distance along x between periodic elements
u_y	separation distance along y between periodic elements
$\hat{\mathbf{u}}_p$	unit vector of the desired polarization
x_i	x -coordinate of position vector
y_i	y -coordinate of position vector
z_i	z -coordinate of position vector
$\hat{\mathbf{z}}$	unit vector in z direction

Γ_x	reflection coefficient to x -polarization
Γ_y	reflection coefficient to y -polarization
$-\Gamma_x$	phase angle of Γ_x
$-\Gamma_y$	phase angle of Γ_y
Δ	phase difference between x and y polarizations

ϵ_{ap}	aperture efficiency
ϵ_{oth}	other efficiencies
ϵ_{po}	polarization efficiency
ϵ_{ph}	phase error efficiency
ϵ_{sp}	spillover efficiency
ϵ_{ta}	taper efficiency
ϵ_{tr}	transmission efficiency
ϵ_0	permittivity of free space
ϵ_r	permittivity of reflectarray dielectric layer
ϵ_{r1}	permittivity of Dielectric 1 layer
ϵ_{r2}	permittivity of Dielectric 2 layer
ϵ_{r3}	permittivity of Dielectric 3 layer
ζ	phase angle
ζ_x	phase between Floquet boundaries separated along x
ζ_y	phase between Floquet boundaries separated along y
ζ_i	phase angle of the array weight due to the element
ζ_1	phase angle of the array weight due to element 1
ζ_i^{lr}	phase angle of the LCP scattered due to RCP incidence
ζ_i^{rl}	phase angle of the RCP scattered due to LCP incidence
θ	polar angle from the z -axis
θ_d	polar angle of desired beam direction
θ_{mn}	polar angle of mode (m,n)
θ_0	polar angle to the edge of the aperture
$\hat{\theta}$	unit vector in the θ direction
λ	wavelength
λ_0	wavelength at the centre frequency
μ_0	permeability of free space
ϕ	azimuth angle from the x -axis in the xy -plane
ϕ_d	azimuth angle of desired beam direction
ϕ_{mn}	azimuth angle of mode (m,n)
$\hat{\phi}$	unit vector in the ϕ direction
ψ	element's rotational orientation angle in xy -plane
ψ_1	rotational orientation angle of element 1
ω	angular frequency
ω_0	centre frequency
ω_1	lower extent of the bandwidth

Chapter 1

Introduction

Lenses can be used to redirect, converge, or diverge electromagnetic radiation. For microwave applications, lenses are often used to converge radiation to or from a source antenna known as the feed. Together, the lens and the feed create an electrically-large aperture antenna. When the antenna is in receiving mode, the lens focuses the incident field from the aperture into the feed; in transmitting mode, the lens focuses the radiation from the feed into a narrow beam. These two modes of operation are shown in Fig. 1.1.

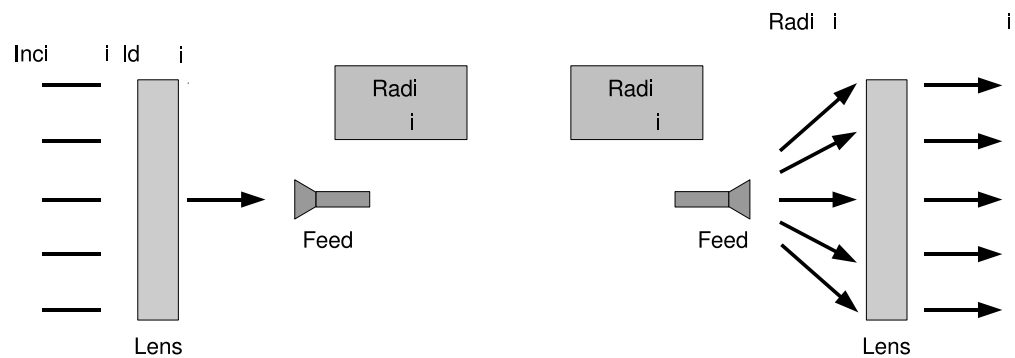


Figure 1.1: A lens antenna system operating in: a) receiving mode and b) transmitting mode.

1.1 Motivation and Applications

In communication systems, there is a choice of technologies for large, fixed-beam antennas, e.g., array antennas, reflector antennas, reflectarray antennas, dielectric

lens antennas. Furthermore, within these antenna groups exists a vast selection of geometries and configurations. The set of these well-established antennas is more than enough to meet most systems' criteria for radiation pattern, gain, side-lobe level, bandwidth, and radiation efficiency. However, the antennas for today's communication systems also have requirements on size, weight, material cost, packed volume, manufacturing cost, and tolerance to manufacturing errors. Meeting these mechanical requirements without compromising the electromagnetic properties is the current challenge for designers of large, fixed-beam antennas.

This thesis presents research on passive array lens antennas for circular polarization. This type of antenna fills a niche between reflectarray and dielectric lens antennas: it provides the cost and weight benefits of the reflectarray, while maintaining the advantages of a lens antenna. Unlike a dielectric lens that is a continuous surface, the passive array lens is a discretized surface that uses an array of antenna-based elements to approximate the effect of dielectric material properties. The array lens is illuminated by a feed to create a space-fed array antenna system.

Choosing an array lens over other lens configurations can provide benefits to weight and packed volume. Improvements in these areas are beneficial to space-born systems, especially during launch. Space-born communication systems often use circular polarization (CP) as it trivializes the Faraday rotation effect in the ionosphere. From a system's perspective, CP eliminates the need for polarization alignment of the transmitting and receiving antennas. The work in this thesis concerns only CP array lenses; therefore, it is most applicable to space-born antennas, especially those for direct broadcasting satellites (DBS).

1.2 Thesis Goals

This research was initiated by an inquiry into the properties of circularly polarized reflectarray antennas. Although well known, the concept of using element rotation to select the phase of the array weights was not always well understood. Much of the literature on this topic made no major distinction between the phase shifts created by rotation, those created by varying the element's resonant frequency, and those created using lengths of transmission line. The first objective of this project was to do a complete analysis of the phase shifts due to element rotation. Specifically, the following questions were to be answered:

- Both qualitatively and analytically, how does rotation create phase shift for an array element?
- What limits the bandwidth for this type of element?
- What effect does the angle of incidence have on the element response?
- What is the effect of scanning the array away from the specular reflection direction?
- Are there any additional advantages or disadvantages to the rotation technique?

By establishing the mechanism of phase shifts created by reflectarray element rotation, it became clear to me that a similar technique was possible for array lens elements. After that realization, the use of rotation to phase an array lens became the major thesis focus. The investigative goal of the thesis was to answer the questions listed above in the context of an array lens. The engineering goals of the thesis were to:

- Develop a suitable element that can be fabricated using printed circuit tech-

nology

- Design, analyze, fabricate, and test a prototype array

This document presents the process towards—and the accomplishment of—these goals.

1.3 Thesis Contributions

By accomplishing these goals, I have made contributions to the field of antenna engineering. These include analytical derivations, antenna designs, design guidelines, antenna modeling, and modeling guidelines; they have been experimentally validated by the measurement of two prototype antennas. Each contribution has also been published outside of this thesis. Chronologically, the contributions are as follows:

- The first contribution is the design of the lens element published in [1]. Simulation results of this design demonstrate that a lens element can provide phase shift by rotation. In this document, it is presented in Sec. 4.3.
- The second contribution is an analysis of the bandwidth for this type of array element [2]. Guidelines for improving the element bandwidth are given in Sec. 4.2.1.
- Next, a prototype high-gain lens was contributed [3]. As shown in Sec. 5.1, the prototype creates a narrow beam with good aperture efficiency.
- A modeling technique for this type of antenna is contributed in [4] and is presented in Sec. 5.1.1. The high-gain lens prototype is modeled and guidelines are given for modeling much larger antennas.

- The next contribution is the presentation of a prototype prism-array that exploits the interesting cross-polarization properties of element rotation [5]. The design is given in Sec. 5.2.
- The final contribution is the derivation of the scattering parameters for a rotated array lens element. It is presented in Sec. 4.1.1. It is included in an IEEE Transactions on Antennas and Propagation paper that has been accepted for publication [6].

1.4 Layout of the Thesis Document

This document is a comprehensive report on the antenna research I performed at the University of Calgary in the years 2007–2010. Chapter 2 presents the branches of antenna theory that are applicable to this research. It includes a discussion of horn antennas, array antennas, and lens antennas. Chapter 3 reviews relevant publications of other authors. Many of these publications present space-fed array antenna prototypes. Chapter 4 describes the design of a novel lens element that uses rotation to phase shift the array weights. The element’s bandwidth and incidence angle limits are presented. Chapter 5 contains the analysis and measurement of two prototype antennas. One prototype acts as a modified convex lens and the other as a Wollaston-type prism. Chapter 6 is the conclusion of the thesis. Possibilities for future work are outlined, and the research contributions are summarized.

Chapter 2

Applicable Theory

Many branches of antenna theory are used to design and analyze the array lenses presented in this thesis. Horn antennas, lenses, and antenna arrays are all mature subjects; therefore, the discussion of these topics in Secs. 2.1, 2.2, and 2.4 focuses on the details relevant to array lenses. More recent antenna topics are planar space-fed arrays and aperture-coupled microstrip-patch antennas. The operation, advantages, and disadvantages of these devices are discussed in Secs. 2.3 and 2.5. The Wollaston prism, an optical device to which one of the prototype lenses is compared, is described in Sec. 2.6. Finally, Floquet Modal Analysis, an analysis technique for periodic structures, is presented in Sec. 2.7. Much of the theory presented in this chapter is available in general form in one or more antenna textbooks, including: [7], [8], [9], [10]. These and other texts will be referenced throughout this chapter.

2.1 Horn Antennas as Spatial Feeds

A horn antenna is simply a metal waveguide that has been flared to a larger opening [7, p.651]. On its own, it finds use as a moderate gain antenna or as a calibration standard. Of particular importance is the use of a horn antenna to excite a larger, nearby structure. In this configuration the horn is known as the feed element in a space-fed antenna system. Reflector antennas, lens antennas, reflectarray antennas, and array lens antennas are all systems that use a feed element to illuminate a

nearby structure. This structure, referred to as the aperture, can be a curved or planar surface. The ratio of the distance between the feed and the aperture to the size of the aperture is known as the focal-length-to-diameter ratio and is abbreviated as F/D . This term is commonly used, even if the aperture is not circular.

For a space-fed antenna in transmitting mode, the task of the feed element is to convert a wave from a transmission line into a wave traveling in space towards the aperture. A horn is well suited to this task as it easily connects to a waveguide transmission line, it radiates most of the power into a beam in the forward direction, and it has very low ohmic loss.

2.1.1 Spillover and Taper Efficiencies

When used as a feed, the horn should have a radiation pattern that illuminates the entire aperture while minimizing the power that spills over the aperture. These two goals are quantified as components of the aperture efficiency: the taper and spillover efficiencies. They both depend on the horn's radiation pattern as well as the F/D ratio. For a given horn, the taper efficiency is increased as the feed moves away from the aperture (it more uniformly illuminates the aperture); however, this also decreases the spillover efficiency (more energy spills over the aperture). This trade-off is illustrated in Fig. 2.1; the configuration on the left has a large F/D ratio and poor spillover efficiency; the configuration on the right has a small F/D ratio and poor taper efficiency. The product of these two efficiencies will be maximized at one specific distance, known as the optimum F/D ratio for a particular feed horn.

Spillover efficiency (ϵ_{sp}) is simply the ratio of the power incident on the radiating

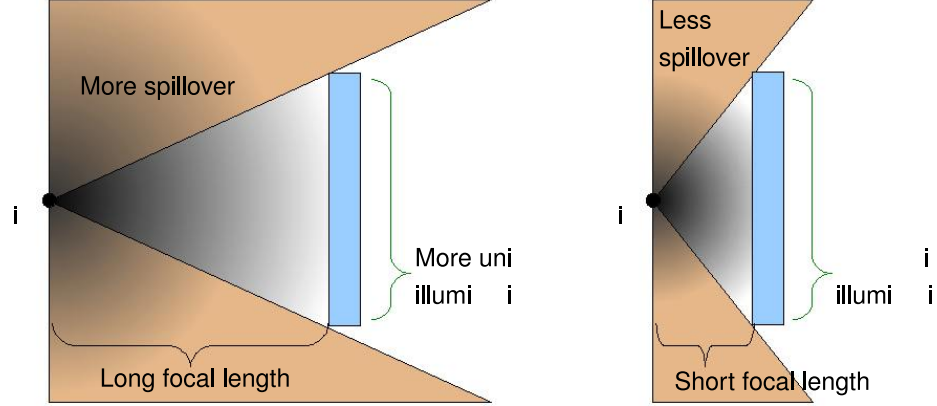


Figure 2.1: Illustration of the trade-off between the taper and spillover efficiencies. The thin rectangle represents the array whereas the triangles show the angular extent of the spillover.

aperture (P_{inc}) to the power radiated by the feed (P_{rad}):

$$\epsilon_{sp} = \frac{P_{inc}}{P_{rad}}. \quad (2.1)$$

For a circular aperture of diameter D centred at $(0, 0, F)$, which is excited by a feed at the coordinate origin, the spillover efficiency can be written as [10, p.384]:

$$\epsilon_{sp} = \frac{\int_0^{2\pi} \int_0^{\theta_0} U(\theta, \phi) \sin \theta \, d\theta \, d\phi}{\int_0^{2\pi} \int_0^{\pi} U(\theta, \phi) \sin \theta \, d\theta \, d\phi}, \quad (2.2)$$

where U is the radiation intensity and θ_0 is the polar incidence angle at the edge of the aperture:

$$\theta_0 = \tan^{-1} \left(\frac{D}{2F} \right). \quad (2.3)$$

The taper efficiency (ϵ_{ta}) calculates the uniformity of the field strength in the aperture:

$$\epsilon_{ta} = \frac{\left(\iint |E| \, ds \right)^2}{s \iint |E|^2 \, ds}, \quad (2.4)$$

where $|E|$ is the magnitude of the electric field over the surface s . For the same circular aperture as above, this area is:

$$s = \frac{1}{4}\pi D^2. \quad (2.5)$$

The maximum gain (G_{ap}) for an aperture of this size is given by the standard formula for directivity [7, p.86]:

$$G_{ap} = 4\pi \frac{s}{\lambda^2} = \left(\frac{\pi D}{\lambda}\right)^2, \quad (2.6)$$

where λ is the wavelength:

$$\lambda = \frac{2\pi c}{\omega}, \quad (2.7)$$

c is the speed of light and ω is the temporal angular frequency. The actual gain (G) of a space-fed antenna system will be reduced by the spillover and taper efficiencies:

$$G = G_{ap}\epsilon_{sp}\epsilon_{ta}\epsilon_{oth}, \quad (2.8)$$

where ϵ_{oth} represents all other reductions in gain. These can be due to radiation efficiency, polarization efficiency, feed blockage efficiency, reflection efficiency, transmission efficiency, and phase error efficiency depending on the specific configuration of the space-fed antenna. One prototype antenna presented in this thesis is designed for high gain; thus the F/D ratio is chosen to maximize the product of the spillover and taper efficiencies.

The choice of feed will also influence the aperture antenna's radiation pattern. For passive, space-fed arrays, the magnitude of the array weights are determined from the radiation power density of the feed; this will be discussed in Sec. 2.3. Although tapered feed patterns reduce aperture efficiency, they also improve side-lobe level by providing tapered weights across the array.

2.2 Array Antennas

Array antennas consist of a set of radiating elements organized into a geometrical pattern. Typically, each radiating element is itself a practical antenna; arrays of dipoles, horns, and microstrip patches are all common. Due to mutual coupling with the surrounding elements, both the impedance and radiation pattern change when an antenna is placed in an array. This is a well-known effect and the waveguide simulator technique can be used to simulate the array environment [11].

If the radiation pattern of each element is identical, the radiation pattern of the entire array can be decomposed into an array factor (AF) and an element factor (EF). The element factor is determined by the type of elemental antenna (e.g. dipole, horn, patch) and the array factor is a function of the excitation distribution across the array. For a large array of low-gain elements, the array factor has the greatest influence on the directivity and side-lobe level of the radiation pattern. The element controls the polarization and the radiation efficiency. The bandwidth is limited by the element factor, but it can also be limited by the array factor as will be shown in Sec. 2.3.4. The array factor of a generic array is given by:

$$AF(\mathbf{k}) = \sum_{i=1}^N A_i e^{j\mathbf{k} \cdot \mathbf{p}_i}, \quad (2.9)$$

where \mathbf{k} is the wavenumber vector, N is the number of elements, A_i is the complex array weight, and \mathbf{p}_i is the position of the element in the array:

$$\mathbf{p}_i = (x_i, y_i, z_i). \quad (2.10)$$

The main advantage of an array antenna is its ability to synthesize various radiation patterns by adjusting the array weights, i.e., adjusting the magnitude and phase

of the field radiated by each element. Array antennas are often categorized by the versatility of their radiation pattern. Active electronically scanned arrays (AESAs) are used mainly in military radars. Each AESA element contains a transmit/receive (T/R) module, which can transmit a different magnitude, phase, and even frequency to perform various radar functions. Similar systems for communications are said to use adaptive array processing (AAP); a complete receiver is associated with each element, and the radiation pattern is formed by digital processing. Passive electronically scanned arrays (PESAs) are the most common type of radar system. A variable phase shifter is associated with each element, but all of the radio-frequency (RF) power is generated by a single source. The collection of transmission lines, power dividers and couplers used to distribute the RF power is known as the feed network. Fixed beam arrays (FBAs) do not have any active components associated with each element. The feed network distributes power from a single source to each passive element. For both PESAs and FBAs, the feed network decreases the gain by contributing additional ohmic loss to the antenna system. These losses increase for larger arrays as more power division stages are required.

2.3 Space-Fed Array Antennas

A spatial feed is a type of feed network that is both simple and efficient. The RF power is generated by a single source; but, the feed network is replaced by a feed antenna, which distributes power to each element by wave propagation through space. The feed antenna is typically a moderate gain antenna with good radiation efficiency. It is designed so that its major lobe directs most of the power onto the

array. A spatial feed causes a reduction in gain, most notably by spillover and taper effects. However, unlike the losses associated with a transmission-line feed network, these losses do not increase with array size. Therefore, spatial feeding is most beneficial for large arrays that have hundreds or thousands of elements.

2.3.1 Array Lenses and Reflectarrays

As shown in Fig. 2.2, array lens and reflectarray antennas are both space-fed, electrically-large array antennas. The trade-offs between a reflectarray and an array lens are similar to those between a curved reflector and a dielectric lens. A reflectarray is conceptually simpler, has low loss, and is easier to construct mechanically if it can be supported from behind. On the other hand, an array lens eliminates the feed blockage that is typical of reflectarrays; this allows the use of large feed antennas or multiple feeds without compromising the radiation aperture. Of particular importance is the array lens' improved tolerance to surface errors. Small deviations in the flatness of a millimeter-wave reflectarray can lead to significant phase errors. On the other hand, surface deviations in array lenses have a smaller effect on the total path length; and hence, the resulting phase errors are smaller [12, p.22] [9, pp.625–627]. This feature will simplify the mechanical structure needed to maintain a flat array surface. Another lens advantage is that the feed is physically covered by the array. In some applications it is important to conceal the feed, e.g., aesthetic or aerodynamic reasons.

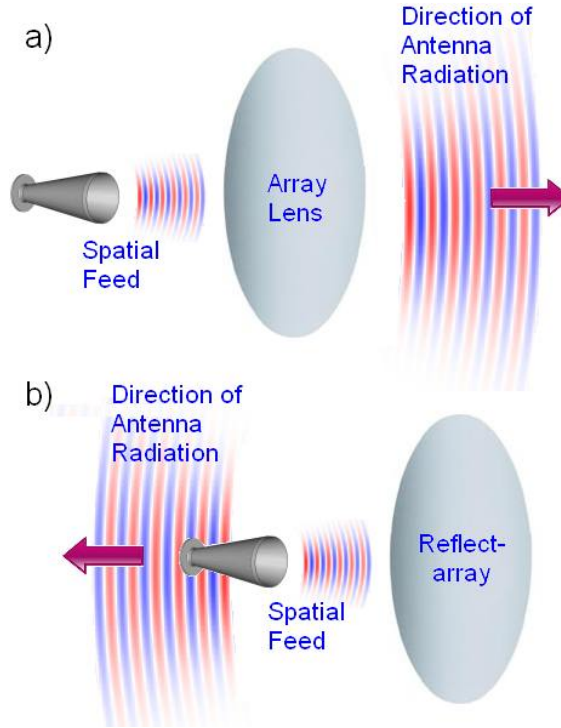


Figure 2.2: Conceptual operation of: a) the array lens and b) the reflector-array. A conical horn feeds both antennas from the left.

2.3.2 Radiation Pattern of Space-Fed Arrays

The array weights of a space-fed array are modified by the feed system and by each element thus blurring the distinction between element factor and array factor. Typically, the element factor is considered constant—even if the elements have slight variations in geometry—and the array weights are decomposed into a component due to the feed and a component due to the element.

$$A_i = A_i^f A_i^e, \quad (2.11)$$

where A_i^f is the complex weight due to the spatial feed, and A_i^e is the complex weight provided by the element. For a specific element, the array weight due to the feed is

determined by the feed's radiation pattern at the element's location:

$$A_i^f = \mathbf{E}(\mathbf{p}_i) \cdot \hat{\mathbf{u}}_p, \quad (2.12)$$

where $\mathbf{E}(\mathbf{p}_i)$ is the electric field at point \mathbf{p}_i in the feed's radiation pattern and $\hat{\mathbf{u}}_p$ is a unit vector representing the desired polarization of the electric field.

For many configurations, the magnitude of A_i^f can be approximated using the feed's far-field radiation pattern and the phase of A_i^f can be approximated using the feed's phase centre. Consider a feed placed such that its phase centre is at the coordinate origin and its major lobe points in the $+z$ direction. The array is planar with all elements in the $z = F$ plane. The distance F is large enough such that the elements are outside of the reactive near-field region of the feed antenna. Then, the weights can be approximated by:

$$A_i^f = \sqrt{|U_f(\theta_i, \phi_i)|} e^{-j\frac{\omega}{c}|\mathbf{p}_i|}, \quad (2.13)$$

where U_f is the far field radiation pattern of the feed. Since the phase centre of the feed is at the coordinate origin, the phase delay to each element is proportional to the length of its position vector:

$$|\mathbf{p}_i| = \sqrt{x_i^2 + y_i^2 + F^2}. \quad (2.14)$$

The direction (θ_i, ϕ_i) towards each element is known as the incidence angle and is defined by:

$$x_i = |\mathbf{p}_i| \sin \theta_i \cos \phi_i \quad (2.15a)$$

$$y_i = |\mathbf{p}_i| \sin \theta_i \sin \phi_i \quad (2.15b)$$

$$F = |\mathbf{p}_i| \cos \theta_i. \quad (2.15c)$$

The second portion of the total array weight is the component provided by the element. It can be expressed as:

$$A_i^e = |A_i^e|e^{j\zeta_i}. \quad (2.16)$$

The magnitude and phase of this weight ($|A_i^e|$ and ζ_i), have different significances depending on the type of space-fed array. For an AESA, they can be controlled by a variable amplifier and phase shifter at each element. For a PESA, the phase is controlled by a variable phase shifter. The magnitude can be controlled using an attenuator, and unwanted magnitude variations are caused by losses, e.g., the loss values associated with each phase state. For a space-fed FBA, the phase is determined by the phase-state geometry of the element. Unwanted magnitude variations are again caused by losses. These losses can vary with incidence angle and frequency. The space-fed FBAs presented in this thesis are designed carefully to ensure that both the magnitude and the phase remain relatively constant over incidence angle and bandwidth.

The phases of the array weight provided by the element (ζ_i) are selected to provide a beam-forming task. Often, this task is to first correct for the phase delays from the spatial feed before performing a secondary task. By substituting Eqns. 2.13, 2.14, and 2.16 into Eqn. 2.11, it is evident that the phase of the total array weight is:

$$-A_i = \zeta_i - \frac{\omega}{c} \sqrt{x_i^2 + y_i^2 + F^2}. \quad (2.17)$$

Thus, selecting:

$$\zeta_i = \frac{\omega_0}{c} \sqrt{x_i^2 + y_i^2 + F^2} \quad (2.18)$$

will cancel the phase delays from the spatial feed at the frequency ω_0 . Simply correcting for the spatial feed will result in a pencil beam directed towards $+z$, known

as the broadside direction. A secondary task can be achieved by superimposing the required phase shifts, e.g., to steer the beam to a direction (θ_d, ϕ_d) select the phase shifts to be:

$$\zeta_i = \frac{\omega_0}{c} \sqrt{x_i^2 + y_i^2 + F^2} - \frac{\omega_0}{c} (\sin \theta_d \cos \phi_d x_i + \sin \theta_d \sin \phi_d y_i). \quad (2.19)$$

For any choice of ζ_i , the geometry of each FBA element is dimensioned to provide that phase state.

To summarize, the complex weights of a passive space-fed array are due to the feed, the positions of the elements, and each element's geometrical phase state. The total array weights are the combination of these effects. They can be used in Eqn. 2.9 to determine the array factor, which has the greatest influence on the directivity of the radiation pattern. To more fully characterize the radiation pattern, the cross-polarization response must also be included. This can be done by representing each element with a scattering matrix instead of a single value of A_i^e . This approach is presented using Floquet Modal Analysis in Sec. 2.7.

2.3.3 Spillover and Taper Efficiency of Space-Fed Arrays

Due to their discrete nature, the spillover and taper efficiencies of space-fed arrays can be simplified from integrals to summations. The spillover efficiency can be simplified by approximating the power incident on each element as the radiation power density of the feed at the centre of each element ($\mathbf{W}_f(\mathbf{p}_i)$), flowing in the direction of the aperture surface ($\hat{\mathbf{n}}$), multiplied by the area of one element (s/N):

$$\epsilon_s = \frac{\sum_{i=1}^N [\mathbf{W}_f(\mathbf{p}_i) \cdot \hat{\mathbf{n}}] \frac{s}{N}}{P_{rad}}. \quad (2.20)$$

The taper efficiency can be simplified using the same approximation: that the field is constant over each element. This approximation is valid if the spatial variation of the feed's radiation pattern is negligible over the small area occupied by each element. It can be applied to large arrays with horn feeds. Using this approximation, the taper efficiency depends only on the magnitude of the array weights:

$$\epsilon_{ta} = \frac{\left(\sum_{i=1}^N |A_i| \right)^2}{N \sum_{i=1}^N |A_i|^2}. \quad (2.21)$$

In Sec. 5.1.3, these equations are used to predict the aperture efficiency of an array prototype.

2.3.4 Bandwidth of Space-Fed Arrays

The bandwidth of an array antenna can be limited by the element factor or by the array factor. In this section, the limitations caused by the array factor are examined. For some array phasing techniques, the phase shift of the array weight provided by the element (ζ_i) does not depend on frequency. One example is the element rotation phasing technique, which is the technique used in this thesis (see Sec. 4.1.4). Because the phase shift is frequency independent, a simple inequality can be derived to indicate the upper limit of the product of bandwidth and aperture diameter. In this section, the limit is derived for an array factor designed to have a narrow beam at broadside.

To cancel the phase delays from the spatial feed and generate a narrow beam at broadside, the phase shifts should be selected according to Eqn. 2.18 at the centre

frequency: ω_0 . At this frequency, the phase of the total array weight (Eqn. 2.17) will be zero for every element.

At a different frequency (ω_1) the phase delays do not cancel; instead, the phase of the total array weight is different for each element:

$$_A_i = \frac{\omega_0}{c} \sqrt{x_i^2 + y_i^2 + F^2} - \frac{\omega_1}{c} \sqrt{x_i^2 + y_i^2 + F^2}. \quad (2.22)$$

If this variation causes the array factor to degrade beyond an acceptable range, then the antenna is beyond its frequency limit. This variation in phase is largest between elements at the edge of the array and those in the centre. If element 1 is at the centre of the array:

$$x_1^2 + y_1^2 = 0, \quad (2.23)$$

and element 2 is at the edge of the array:

$$x_2^2 + y_2^2 = \frac{1}{4}D^2, \quad (2.24)$$

then the phase difference between the edge and centre elements at frequency ω_1 is:

$$_A_2 - _A_1 = \frac{(\omega_0 - \omega_1)}{c} \left(\sqrt{\frac{1}{4}D^2 + F^2} - F \right). \quad (2.25)$$

The variation grows larger as ω_1 moves away from the centre frequency. If ω_1 is at the lower extent of the frequency bandwidth, then the fractional bandwidth (B) is given by:

$$B = \frac{2(\omega_0 - \omega_1)}{\omega_0}, \quad (2.26)$$

and the phase difference between elements 1 and 2 can be expressed as:

$$_A_2 - _A_1 = \pi \frac{D}{\lambda_0} B \left(\sqrt{\left(\frac{F}{D}\right)^2 + \frac{1}{4}} - \frac{F}{D} \right). \quad (2.27)$$

Thus, for a given F/D ratio, the phase difference is proportional to both the bandwidth and the diameter in wavelengths. As mentioned above, as the phase variation increases, the pattern of the array factor degrades: the beamwidth and side-lobe-level both increase. The system specifications will dictate the maximum acceptable value of phase difference,

$$-A_2 - A_1 \leq -A_{max}, \quad (2.28)$$

and this creates a limit on the product of bandwidth and array diameter:

$$B \frac{D}{\lambda_0} \leq \frac{-A_{max}}{\pi} \left(\overline{\left(\frac{F}{D}\right)^2 + \frac{1}{4} - \frac{F}{D}} \right)^{-1}. \quad (2.29)$$

Since the maximum gain of the aperture is a function of the diameter squared (Eqn. 2.6), the largest fractional bandwidth over which the edge and centre elements maintain an acceptable phase difference is:

$$B \leq \frac{-A_{max}}{\sqrt{G_{ap}}} \left(\overline{\left(\frac{F}{D}\right)^2 + \frac{1}{4} - \frac{F}{D}} \right)^{-1}. \quad (2.30)$$

Or, conversely, the maximum gain of the aperture (at ω_0) is limited to:

$$G_{ap} \leq \left(\frac{-A_{max}}{B} \right)^2 \left(\overline{\left(\frac{F}{D}\right)^2 + \frac{1}{4} - \frac{F}{D}} \right)^{-2}. \quad (2.31)$$

It should be reinforced that these limitations are for arrays whose elemental phase shifts do not vary with frequency. The limitations will be even more stringent if the phase shifts decrease with frequency. If the elements provide time delay instead of phase shift, these limitations will be removed and the antenna bandwidth will be limited by either the element factor or by other changes to the array factor, e.g., the appearance of grating lobes.

2.4 Lens Antennas

Lens antennas are, not surprisingly, antenna systems where the radiation characteristics of a feed are modified by the use of a lens. For microwave engineers, the term ‘lens’ is more encompassing than in common usage. As well as traditional dielectric lenses, any structure that converges or diverges a wave is considered a lens. This includes arrays of antenna elements, which selectively advance or delay portions of the wave’s phase front.

The simplest design of any focusing lens can be performed using ray tracing and geometric optics. The lens is designed to create equal electrical path lengths between a focal point and a planar wavefront. Since an array lens is discretized into elements, the electrical path length is designed to be equal for each element.

2.4.1 Dielectric Lenses

At microwave frequencies, dielectric lenses can be created from traditional bulk materials or artificial materials. Traditional artificial dielectrics consist of a lattice of discrete metal particles, e.g., metal strips, rods, or spheres [9, p.616]. More recent artificial materials, known as meta-materials, also consist of a metallic lattice; however, they can synthesize properties that are not commonly found in nature. The lattice spacing is much larger than the atomic structure of a bulk material dielectric, but smaller than a wavelength.

A dielectric lens consists of a material—bulk or artificial—whose shape refracts the radiation from a feed. The shape of the lens is described by the equations of the inner and outer surface. The simplest dielectric lenses have one refracting surface

[10, p.448]. The shape of the refracting surface is determined from the material's dielectric properties. The bandwidth for which the dielectric properties are constant determines the bandwidth of the lens. For large lenses, especially those with small F/D ratios, this type of lens can be quite bulky and heavy.

To reduce the weight of large lenses, sections of the lens can be removed creating a device known as a zoned lens or a Fresnel lens. Zoning removes material in multiples of one wavelength so that the phase of the electrical path length is unchanged. Since the shape of the lens is referenced to a specific wavelength, zoned lenses are not frequency independent. Zoning also introduces diffraction in the lens, especially for lenses zoned on the refracting surface.

Two-surface lenses are dielectric lenses with two refracting surfaces. This configuration allows an additional degree of freedom in lens design, as the second surface can be used to eliminate coma or other higher-order lens functions [8, p.18-5]. It is not often used at microwave frequencies as the performance advantages seldom outweigh the increased cost of machining two abnormal surfaces.

2.4.2 Bootlace Lens

A bootlace lens is an array lens in which the elements consist of an inner- and outer-surface radiator connected by a transmission line [8, p.18-17]. The transmission line length is chosen to create equal path lengths between the feed and a planar wavefront. Typically, the mode of propagation in the transmission line is non-dispersive so that it provides the correct phase shift over a wide bandwidth, i.e., the transmission line provides a constant time delay rather than a constant phase shift. The surfaces of a bootlace lens can be curved or planar; however, the lens must always delay the wave

propagating through the central elements using a meandering transmission line.

If no zoning is used, a bootlace lens is a wide-band antenna limited only by the bandwidth of the inner- and outer-surface radiators. Bootlace lenses are a type of constrained lens as the wave in the lens is constrained to propagate inside the transmission lines. It is a suitable choice for large antennas that require wide bandwidth; but, the traditional disadvantage is that each element must be fabricated and assembled independently, which can lead to expensive, bulky structures. Modern bootlace lenses, fabricated using printed circuit technology, are presented in Sec. 3.1.2.

2.4.3 Waveguide Lenses

Waveguide lenses consist of an array of metallic waveguides. Either a two-dimensional array of rectangular waveguides, or a one-dimensional array of parallel-plate waveguides can be used to converge an incident wave. These arrays are often known as fast lenses [9, p.607]; the incident wave excites a transverse-electric (TE) mode, and the phase velocity of this mode is faster than the phase velocity in free space. The one-dimensional waveguide lens must be oriented with the metal plates parallel to the electric field so that a TE mode is excited. The phase front of the wave is accelerated inside a fast lens, thus the lens is wider at the edges and narrower in the centre. Note that the group velocity of this mode is slower than in free space; thus, the phase front acceleration in a fast lens does not violate special relativity.

Like a bootlace lens, waveguide lenses are also constrained lenses because the metal structures constrain the wave propagation direction inside the lens [13, p.293]. In fact, the waveguide lens is a type of bootlace lens, but the transmission line is dispersive. The simplicity of this configuration is that a single waveguide acts as

both bootlace lens components. The open-ended waveguide acts as the inner- and outer-surface radiator, and the length of waveguide is the transmission line. Metal shorts were added to the outer ends of rectangular waveguide to create the first reflectarray [14]. Zoning can be used to reduce the weight of waveguide lenses; and furthermore, zoning can improve the bandwidth of these lenses [9, p.623].

2.5 Aperture-Coupled Microstrip Patch Antennas

A microstrip patch antenna is a resonant cavity on a printed circuit board (PCB). It consists of the metal patch—typically a rectangular shape—patterned on one side of the board and a ground plane on the other. It can be excited with many feed types, e.g., probe-feed, microstrip-feed, proximity-coupled feed, aperture-coupled feed. A probe-feed shields the transmission line from radiating but requires a via line through the circuit board. It is the most common feed for single patch applications [8, p.7-2]. Microstrip-feed patches are simple to manufacture, but the transmission line leading to the patch can create unwanted radiation. Both the proximity- and aperture-coupled feeds have no metallic connection to the patch, and require a second PCB.

Aperture-coupling has recently received a lot of interest because it is both simple to manufacture and it shields the transmission line from radiating. The transmission line is patterned on the outer surface of one PCB and the patch is patterned on the outer surface of the other. Between these two dielectrics is the ground plane. It can be patterned on either material but it acts as a ground plane for both the transmission line and the patch antenna. An aperture is cut out of the ground plane and it is dimensioned such that the antenna is matched to the transmission line.

Waves traveling along the transmission line are coupled through the aperture to excite the antenna.

The use of a second PCB benefits both the transmission line and the antenna. Typically, a transmission line’s performance is improved if the dielectric is thin and has a high permittivity. Conversely, a patch antenna is improved if the dielectric is thick and has a low permittivity. By separating these two components onto opposite sides of the ground plane, two appropriate PCBs can be used.

To radiate circular polarization from an aperture-coupled patch, two orthogonal modes can be coupled through the aperture. A cross-shaped aperture was first used in [15], and it is used again in this thesis. If a second patch—patterned on yet another circuit board—is placed above the first, the bandwidth of the element can be increased. This configuration is known as a stacked-patch antenna.

2.5.1 Aperture-Coupled Elements for Space-Fed Antennas

Aperture coupling can be used to excite space-fed array elements. For this application, the transmission line serves a different purpose. Instead of linking the source to the antenna, the transmission line creates an opportunity to alter the element’s array weight. This effect can be conceptually described as follows:

1. First, the microstrip patch receives the incident wave from the feed.
2. Next, the wave couples through the aperture and onto the transmission line.
3. Then, circuit components placed on the transmission line alter the magnitude and phase of the wave.
4. For reflectarrays, the wave reverses its direction along the transmission line; for array lenses, the wave proceeds along another length of transmission line

towards a second aperture-coupled patch element.

5. Finally, the wave couples through the aperture, excites the patch and radiates.

Passive or active components can be inserted onto the transmission line to change the element's array weight. Simply lengthening the transmission line between apertures can create a microstrip-patch version of a bootlace lens.

As with a stand-alone patch, the main advantage of aperture coupling for spaced arrays is the isolation of the transmission line and the radiating element. The disadvantage, especially for array lens elements, is the additional complexity of inserting the transmission line between the inner- and outer-surface radiators. Chapter 4 of this thesis presents a novel element that uses aperture coupling but does not require a transmission line.

2.6 Wollaston Prism

The Wollaston Prism is an optical device that splits a beam of light into its linear polarization (LP) components. As shown in Fig. 2.3, an incident beam having both horizontal and vertical polarization is separated into two beams, each one corresponding to one of the LP components. The divergence angles of the two beams are equal but opposite.

It consists of two wedges of birefringent material (typically calcite) cemented together. Due to its crystal structure, the phase velocity of light inside the birefringent material is anisotropic. For calcite, the velocity along one direction is about 11% faster than in the orthogonal directions; this direction is known as the optical axis. The Wollaston Prism is created by cutting the wedges such that their optical axes

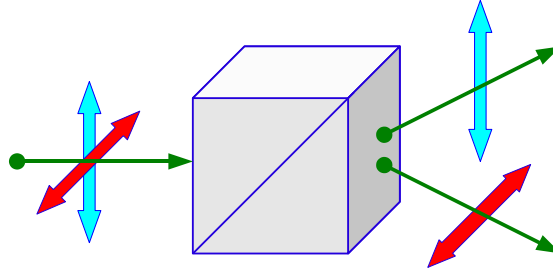


Figure 2.3: Wollaston prism

are in different directions: the axis must be parallel to the triangular face of one wedge, and perpendicular to the triangular face of the other wedge.

Although it provides a conceptually-simple function, the Wollaston prism is mainly used in very specific optical devices, such as differential-interference-contrast microscopes [16, p.154], interferometric ellipsometers [17, pp.262–265] and phase modulated ellipsometers [18, pp.307–308]. The array lens prototype designed in Sec. 5.2 acts a Wollaston prism, but for circular polarization (CP).

2.7 Floquet Modal Analysis

Floquet modal analysis is a mathematical tool that can be used for electromagnetic analysis of periodic structures. It can be used in situations where the magnitudes of the fields are periodic, but the phases of the fields have a constant shift between periods. In this work, Floquet analysis is used to model a plane wave incident at an angle on a planar periodic structure. Each element of the structure will receive the identical magnitude of the incident field, but the phase will be sequentially delayed between neighbouring elements. The value of the delay can be computed from the vector components of the plane wave phase constant (k_x and k_y) and from the spacing

between elements in the rectangular grid (u_x and u_y):

$$\zeta_x = -k_x u_x \quad (2.32a)$$

$$\zeta_y = -k_y u_y, \quad (2.32b)$$

where ζ_x and ζ_y are the incident field phase differences between neighbouring elements in the x and y directions.

When excited by a plane wave, each element's response will have the identical magnitude; but, the phase of the response will be influenced by the phase of the incident field. The phase differences between neighbouring elements must be equal to the phase delays of the incident field (ζ_x and ζ_y) plus an integer multiple of 2π . Each multiple of 2π corresponds to one Floquet mode excited by the structure. Since it is a planar array, the Floquet modes are 2-dimensional and are labeled using two indexes: m and n . The phase constants of each mode are:

$$k_{xmn} = \frac{-\zeta_x + 2m\pi}{u_x} \quad (2.33a)$$

$$k_{ymn} = \frac{-\zeta_y + 2n\pi}{u_y} \quad (2.33b)$$

$$k_{zmn} = \pm \sqrt{k_0^2 - k_{xmn}^2 - k_{ymn}^2}, \quad (2.33c)$$

where k_0 is the phase constant in free space:

$$k_0 = \omega \sqrt{\mu_o \varepsilon_o}, \quad (2.34)$$

and μ_o and ε_o are the permittivity and permeability of free space. Thus, k_{x00} and k_{y00} are the phase constants of the fundamental Floquet mode and are equal to the phase constants of the incident plane wave.

Floquet analysis allows the response of the structure to be decomposed into a set of spatially-harmonic modes. Only a finite number of modes represent propagating plane waves, while the remaining modes (of infinite number) represent fields that are evanescent along z . For antennas, this distinction is important as only the propagating modes influence the far-field radiation pattern.

The propagating modes satisfy:

$$k_{xmn}^2 + k_{ymn}^2 \leq k_0^2 \quad (2.35)$$

which, when compared to Eqn. 2.33c will result in a real number for k_{zmn} . The direction (θ_{mn}, ϕ_{mn}) associated with these propagating modes is given by:

$$k_{xmn} = k_0 \sin \theta_{mn} \cos \phi_{mn} \quad (2.36a)$$

$$k_{ymn} = k_0 \sin \theta_{mn} \sin \phi_{mn} \quad (2.36b)$$

$$k_{zmn} = k_0 \cos \theta_{mn}. \quad (2.36c)$$

The notation and equations in this section are all similar to those found in [19, Ch.2].

2.7.1 Computational Floquet Analysis

Computational electromagnetic codes can implement Floquet modal analysis to simplify the simulation of periodic structures. This is typically done by surrounding a single element with artificial surfaces known as Floquet boundaries. These boundaries allow for the simulation of the element's response when surrounded by the infinite periodic structure. From this response, the modes are extracted and identified as propagating or evanescent modes.

In this research, Floquet Modal Analysis is used to design and evaluate array lens elements. The first type of simulation models an infinite periodic structure by

surrounding a single array element with Floquet Boundaries. Since the elements are arranged in a $1/2$ wavelength square grid (at the centre frequency), the distance between boundaries is also $1/2$ wavelength:

$$u_x = u_y = \frac{1}{2}\lambda_0. \quad (2.37)$$

With this condition, the only set of indexes that will satisfy Eqn. 2.35 is:

$$m = n = 0. \quad (2.38)$$

Each set of (m,n) indexes corresponds to four electromagnetic modes. One pair of electromagnetic modes is associated with one of the roots of Eqn. 2.33c and corresponds to a mode propagating in either the $+z$ or $-z$ direction. The final distinction between modes is in the polarization of the electric field. Floquet modes are often decomposed into transverse-electric (TE) and transverse-magnetic (TM) modes.

This thesis focuses on circular polarization (CP); therefore, the fields in the propagating modes will be decomposed into left-hand circular polarization (LCP) and right-hand circular polarization (RCP) modes. The plane of the polarization circle is perpendicular to the direction of propagation. Since only one set of indexes satisfies Eqn. 2.35, only four electromagnetic modes can propagate in this simulation. For the lens element, these four modes are:

1. the transmitted LCP mode,
2. the transmitted RCP mode,
3. the reflected LCP mode,
4. the reflected RCP mode.

Note that for frequencies above the centre frequency, additional modes can propagate for large incidence angles; however, this condition does not occur for the range of incidence angles and the bandwidth of the simulations presented in this thesis.

The computational simulations determine the magnitude and phase of these modes with respect to the magnitude and phase of the incident wave. Since the incident wave is in fact one of the allowable modes, the result of the simulation is a 4-by-4 modal scattering matrix for each incidence angle. An element design is acceptable when the scattering matrix meets certain criteria over both a range of incidence angles and a specified frequency bandwidth.

2.7.2 Four Element Floquet Analysis

The second type of computational Floquet analysis in this thesis surrounds a line of four elements with Floquet boundaries. In this configuration, the separation between periodic boundaries is:

$$u_x = 2\lambda_0 \tag{2.39a}$$

$$u_y = \frac{1}{2}\lambda_0. \tag{2.39b}$$

To allow broadside modes, the boundaries are set to a phase difference of zero:

$$\zeta_x = \zeta_y = 0. \tag{2.40}$$

Just below the centre frequency the propagating modes are those with indexes:

$$(m, n) = (0, 0), (+1, 0), (-1, 0). \tag{2.41}$$

These are plane wave modes and all other modes are evanescent. Since the boundary separation in the x direction is exactly two wavelengths, the centre frequency is

the cutoff frequency for additional modes. Just above the centre frequency, the propagating modes are:

$$(m, n) = (0, 0), (+1, 0), (-1, 0), (+2, 0), (-2, 0). \quad (2.42)$$

Near the centre frequency, the scattering parameters associated with the additional modes must be used with caution.

In the $+z$ sense, two electromagnetic modes can propagate for each set of indexes: one LCP mode and one RCP mode. Their propagating direction will vary with frequency in accordance with Eqn. 2.36. Near the centre frequency, their nominal directions are:

$$(\theta_{00}, \phi_{00}) = (0^\circ, 0^\circ) \quad (2.43a)$$

$$(\theta_{+10}, \phi_{+10}) = (30^\circ, 0^\circ) \quad (2.43b)$$

$$(\theta_{-10}, \phi_{-10}) = (30^\circ, 180^\circ) \quad (2.43c)$$

$$(\theta_{+20}, \phi_{+20}) = (90^\circ, 0^\circ) \quad (2.43d)$$

$$(\theta_{-20}, \phi_{-20}) = (90^\circ, 180^\circ). \quad (2.43e)$$

For each set of indexes, two other electromagnetic modes can propagate in the $-z$ sense:

$$(\theta_{00}, \phi_{00}) = (180^\circ, 0^\circ) \quad (2.44a)$$

$$(\theta_{10}, \phi_{10}) = (150^\circ, 0^\circ) \quad (2.44b)$$

$$(\theta_{-10}, \phi_{-10}) = (150^\circ, 180^\circ) \quad (2.44c)$$

$$(\theta_{+20}, \phi_{+20}) = (90^\circ, 0^\circ) \quad (2.44d)$$

$$(\theta_{-20}, \phi_{-20}) = (90^\circ, 180^\circ). \quad (2.44e)$$

This results in twelve propagating electromagnetic modes below the centre frequency and twenty above. Thus, the computational simulation calculates a 20-by-20 scattering matrix for this structure.

2.8 Chapter Summary

This chapter has presented antenna theory that is applicable to the array lens research in this thesis. The first section examined horn antennas, which are used to feed the array lens prototypes. The horn's position is important, as it affects the spillover and taper efficiencies of the complete antenna system. Array lenses are space-fed arrays; thus, the derivations in Sec. 2.3 are used to calculate their radiation pattern, efficiency and bandwidth. The prototypes use array elements that are based on aperture-coupled microstrip patch radiators. The basic operation of these antennas was described in Sec. 2.5. Dielectric lenses, bootlace lenses, waveguide lenses, and Wollaston prisms were discussed in Secs. 2.4 and 2.6. Like an array lens, they can all be used to redirect an incident wave. Floquet Modal Analysis is a useful technique for periodic structures such as the array lens. A derivation of the allowable propagating directions for plane waves was given in Sec. 2.7. The next chapter reviews relevant literature published by other authors.

Chapter 3

Review of Relevant Literature

This chapter discusses the work of other researchers pertaining to the antenna developed in this thesis. Specifically, the target of this research is a passive array lens antenna using the rotational orientation of printed antenna elements to provide phase shift for circular polarization (CP). Much of the relevant literature is in the form of transaction papers or conference proceedings, and presents antenna concepts targeting a particular application or filling a certain niche. This review focuses on space-fed array antennas, especially those using the element rotation technique for CP. Concepts for linear polarization (LP) that can be easily modified for CP applications are also discussed; these use other phasing techniques, but are relevant as they use low-profile passive elements.

Array lenses are presented in Sec. 3.1, reflectarrays are presented in Sec. 3.2, and some additional configurations are presented in Sec. 3.3. For those papers that present prototype measurements, the antenna characteristics and performance metrics are summarized in Table 3.1 at the end of this chapter. In Sec. 3.4, the prototype designed in this thesis is compared to those reviewed in this chapter.

3.1 Array Lenses

Although it is equally applicable to both array lenses and reflectarrays, the element rotation technique is not well represented in array lens literature. Other than the

work in this thesis, only three concepts appear to have been presented. Prototypes for these three CP concepts are reviewed in Sec. 3.1.1; array lenses for LP that can be easily modified for CP are reviewed in Sec. 3.1.2.

3.1.1 Array Lenses Using Element Rotation

The first array lens using element rotation was presented by authors from the United States Naval Research Laboratory in the 1960s as a patent [20] and a paper [21]. The complete antenna is composed of a feed and a planar array of elements. Each element consists of two spiral antennas—one on either side of a ground plane—connected by a coaxial transmission line. Prototype lenses were presented in the paper; each spiral was manufactured individually and assembled onto the ground plane. In this configuration, the spiral antennas are similar to the inner- and outer-surface radiators of the bootlace lens discussed in Sec. 2.4.2. However, unlike a bootlace lens, the length of transmission line is identical for each element. Since the spirals transmit and receive circular polarization, the phase shift is created by selecting the rotational orientation angle of each pair of spirals in the plane of the array.

A spiral antenna is circularly polarized; the handedness of CP is determined by the windings of the spiral. One of the requirements for the element rotation technique is that the handedness of CP must change as it passes through the lens element (this will be derived in Sec. 4.1). With two spiral antennas, this is easily accomplished by designing one spiral of each pair to have left-hand (LH) windings and the other to have right-hand (RH) windings. The authors of this concept use the term “parasitic lens array” to describe their creation. This prototype is summarized in Table 3.1; although it achieved only 20% aperture efficiency, 40–50% should be possible. The

authors also note the trade-off between bandwidth and array diameter.

The second lens concept using element rotation is a variation of the first. It was presented in a 1977 conference paper [22] by authors from Hughes Aircraft Company. The element concept is fundamentally identical: counter-wound (one LH and one RH) radiators are connected by a coaxial transmission line. The difference is that helical radiators—rather than spiral—are used. Again, they are manufactured individually and then assembled into an array. The prototype array has a spherical inner surface so that the path length from the feed to each element is constant across the array. The element rotations correct for the spherical outer surface of the array and create a narrow beam at broadside. In the paper, the prototype’s performance is compared to a zoned waveguide lens; the authors conclude that element rotation generates smaller phase error and higher gain over a fixed bandwidth. The peak aperture efficiency is 54%, which is very good for an array lens. To my knowledge, this is the only paper that references [21] as an example of the element rotation technique. It is also the only other prototype using counter-wound radiators.

The third lens concept using element rotation is significantly different. It was presented in a conference paper in 2010 [23], and it was developed concurrently with the work presented in this thesis. The element consists of rectangular microstrip patch radiators on both sides of a ground plane. A via connects the patches through the ground plane. Since they are fabricated on printed circuit boards (PCBs), many elements can be fabricated simultaneously using an etching process.

Unlike the spiral- or helix-based concepts, this array is excited by an LP feed and the patch elements receive and transmit LP. Furthermore, the entire element is not rotated—only the outer-surface patch is rotated but the inner-surface patch is not.

All the inner-surface patches have the same rotational orientation; they are parallel to the feed polarization. The rotation of the outer-surface patches is used to create the CP phase shift distribution across the array. The inner-surface patch receives LP from the feed, the wave passes through the via line and is re-radiated from the outer-surface as LP. For each element, the transmitted LP tilt angle is equal to the rotation angle of the outer-surface patch, and the transmitted phase is due to the phase delay from the feed. By appropriately choosing the tilt angle to correspond to a particular phase delay, the sum of the LP fields transmitted by each element appear as CP transmitted by the entire array.

Using this concept will result in a reduced aperture efficiency; their prototype achieved only 24%. However, it has great potential for extension to actively phased elements as only the outer-surface patch needs to be rotated and the inner-surface patch can remain stationary. It can be phased by physically rotating the outer-surface patch using a micromotor or by effectively rotating it using electronic switches.

3.1.2 Array Lenses for Linear Polarization

In this section, array lens element concepts for LP on circuit boards are discussed; however, the nature of these elements allows them to be used for dual LP or for CP applications. Prototypes from these papers are summarized in Table 3.1.

The first lens concept using microstrip patch elements was published in 1986 [24]. It is simply a PCB implementation of a bootlace lens: microstrip transmission lines and a via line connect inner- and outer-surface patches. The length of transmission line is different for each element; it is selected so that the delay from the feed is compensated by the delay along the transmission line. A similar concept using

aperture coupled patches and varying lengths of stripline has also been presented [25]. For both of these elements, the transitions between transmission line and radiators are designed for LP patches; but, slight modifications would allow for CP patches.

A second element concept, presented in [26], consists of a patch over an aperture in a ground plane. To phase shift the transmitted wave, a stub is connected to the patch and its length is varied. This phasing technique had been common in reflectarray elements; but, the stubs are not as effective in providing a wide range of phase shift for an array lens.

A lens prototype fabricated on circuit boards was published in 2001 [27]. Each element contains cross-shaped radiators and its transmission phase is selected by scaling the overall size of the cross. By scaling the size of a radiator, its resonant frequencies vary. Typically, a phase gradient is associated with frequencies near a resonance; thus, slight variations in the resonant frequency will cause phase variations at a fixed frequency. The elements are usually designed so that variations in the resonant frequency result in 360° of phase shift at the antenna's centre frequency. For this element, three layers of cross radiators are required to attain 335° of phase shift. The prototype achieved 40% aperture efficiency.

Concurrent to the work presented in this thesis, other LP array lenses are being developed using a wide variety of elements. Concepts that vary the element's resonant frequency include: double square rings [28], square patches [29], and patches with resonant apertures [30]. These designs achieve good aperture efficiency (45–50%) and reasonable bandwidth (5.9–7.5% of the centre frequency). Improving the bandwidth while maintaining a thin structure is the main challenge when varying the element's resonant frequency.

Another bootlace lens using microstrip patches was recently presented [31]. The transmission line is patterned on a perpendicular circuit board to allow space for active components. A passive prototype was measured and it achieved 50% aperture efficiency.

Some elements, including [32] and [33] are being designed to provide active phase shift for scanning arrays. Other recent contributions combine array lens elements with amplifiers for spatial power combining [34], [35], [36]. Since this thesis concerns only passive FBAs, these active array elements are not discussed here.

3.2 Reflectarrays Using Element Rotation

The element rotation technique is well recognized in reflectarray literature. Most papers list it, along with lengths of transmission line and varying a resonant frequency, as one of the main phasing techniques. The concept originated in 1947 as phase shifter for cylindrical waveguide [37], and that application was recently revisited [38]. The introduction of element rotation into reflectarrays is most often traced back to [39] from 1976. All types of reflectarray antennas gained popularity with the introduction of microstrip elements on PCBs, and the element rotation technique was no exception. A design using rotated microstrip patch elements with delay stubs was presented in 1998 [40]. Since then, various passive reflectarray elements have been proposed for this technique: shorted ring slots [41], dipoles over a ground plane [42], edge-shortened disks [43], ring elements [44], loaded ring slots [45], and split square rings [46]. The prototype's performance from some of these element concepts is listed in Table 3.1. The aperture efficiencies are between 46–60%, and

bandwidths range from 3.5–7% depending on the bandwidth criteria.

Two similar reflectarrays are presented in [40]; both are listed in Table 3.1. They are the same size, operate at the same frequency, and are built using the same materials. The only difference is their phasing technique; one employs element rotation and the other uses different lengths of transmission line. The notable performance differences are aperture efficiency and cross-polarization discrimination ratio (XPD). The improved XPD performance of the element rotation technique will be discussed throughout this thesis. In fact, this is one of its main advantages over using lengths of transmission line or varying a resonant frequency. Some of the papers listed in this section observe a good XPD for their prototypes, but none analyze the cause.

As well as passive elements, some actively rotating reflectarray elements have also been presented: ring slots with pin-diode-switched radial stubs [47], bow-tie elements with MEMS switches [48], edge-shortened disks using electric motors [49], and dipoles over a ground plane using MEMS motors [50]. However, none of these active elements have been assembled into planar arrays. Many of these important contributions have been cited in a recent book on reflectarray antennas [12].

3.3 Other Similar Configurations

In addition to array lenses and reflectarrays, other antenna configurations that excite a passive array from a single element are currently being developed. In some of these, the feed element is placed in a cavity between the array and a reflective surface. In one such configuration, the array is considered to be a parasitic loading of the feed [51]; the feed is placed between an array of dipoles and a ground plane. Similar to

other space-fed arrays, the length of each dipole is selected to create a narrow beam. In another configuration, the antenna is considered to be a discretized Fabry-Perot resonator [52]. The feed is placed between a frequency-selective surface with partial reflectivity and a discretized high-impedance surface. The reflection phase from the high-impedance surface is selected to create a narrow beam. Neither of these configurations have been analyzed using array theory, but the discrete and periodic nature of both the parasitic loading and the high-impedance surface establish these antennas as space-fed arrays.

When compared to an array lens, the main advantage of these structures is their *overall* low profile. The spacing between the array and the reflective surface is typically less than one wavelength—much less than the focal length of an array lens. As listed in Table 3.1, the aperture efficiency (71%) published in [52] is very good. However, the disadvantage of these structures is their limited gain. They cannot be easily scaled to larger apertures since their operation depends on the interaction between the array, the reflective surface, and the feed.

Many other antenna configurations consisting of an incident wave and a planar surface have also been developed. In general, the scattering features on the planar surface are designed to add constructively in the desired beam direction and destructively in other directions. These configurations are not considered to be arrays since their scattering features are either irregularly spaced or they vary smoothly.

Holographic antennas are one example; they consist of an incident wave scattering from a holographic plate [53, pp.17-129–17-131]. The holographic plate is a circuit board where the metalization geometry relates to the interference pattern between the incident wave and the desired scattered wave. In general, the metalization is

irregularly spaced. The design process results in structures similar to leaky-wave and reflectarray antennas; however, the theory behind the design process is based on holographic principles.

3.4 Chapter Summary

This chapter has discussed the literature relevant to the array lens antenna developed for this thesis. Three lens elements that use rotation to phase the array are directly comparable; they were discussed in Sec. 3.1.1. Two of these use individually fabricated, bulky elements with counter-wound wire radiators. Although the antenna performance of [22] is quite good, its manufacturing cost, weight, and packed volume are undesirable. The third concept has the opposite benefits and detriments: since it is fabricated on PCBs, it is thin and its manufacturing cost and weight are good; however, its aperture efficiency is low.

Printed bootlace lenses phased using lengths of transmission line, and other passive array lens elements phased by varying a resonance frequency were discussed in Sec. 3.1.2. The recent prototypes are all lightweight, low profile, and achieve good aperture efficiency. They can be extended to CP; however, they would not provide the cross-polarization benefits associated with element rotation.

The reflectarrays listed in Sec. 3.2 are fabricated on PCBs and they are phased using element rotation. However, as mentioned in Sec. 2.3.1, reflectarrays can suffer from feed blockage and they have a reduced tolerance to manufacturing errors. Furthermore, for some applications the reflectarray feed may be difficult to conceal.

It would be beneficial to have an array lens concept that is phased using element

rotation, maintains good aperture efficiency over a wide bandwidth, and is fabricated on PCBs. This thesis presents such an antenna; a conceptual drawing of it is shown in Fig. 3.1. Its elements consist of stacked microstrip patches and a cross-shaped aperture patterned on PCBs. Since aperture coupling links the inner- and outer-surface radiators, no transmission line is required. The design of this element is one of the main contributions of this thesis. It is completely described in Sec. 4.3.

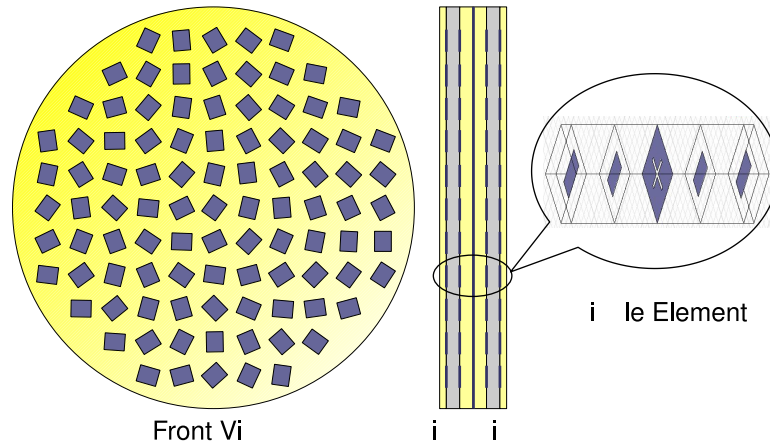


Figure 3.1: The array lens concept presented in this thesis. Front View: the array consists of rotated passive elements. Side View: the multi-layer structure consists of metal patterned on PCBs. Single Element: each element consists of microstrip patches and an aperture in the ground plane.

A prototype antenna using this element is presented in Sec. 5.1; its characteristics and measured performance are appended to Table 3.1. When compared to the others, the prototype in this thesis is impressive. At 48%, its aperture efficiency is comparable to other array lenses. Its cross-polarization discrimination ratio (20 dB) is within the XPD range of other measured CP prototypes. However, the -3 -dB bandwidth (17%) and the -1 -dB bandwidth (8.5%) are larger than those of all the relevant space-fed array prototypes discussed in this review.

Publication	Year	Frequency (GHz)	Polarization*	Array Lens / Reflectarray	Aperture Efficiency (%)	Array Thickness (mm)	Cross-Polarization Discrimination Ratio (dB)	-3-dB Bandwidth (%)	-1-dB Bandwidth (%)	40% Aperture Efficiency Bandwidth (%)	Phasing Technique**
[21]	1960	3.0	CP	AL	20	50	—	—	—	—	ER
[22]	1977	8.1	CP	AL	54	—	—	—	—	—	ER
[23]	2010	10	CP	AL	24	3.0	23	13	—	—	ER
[27]	2001	8.4	LP	AL	40	17	—	—	—	—	VR
[28]	2010	30	LP	AL	47	9.5	—	—	7.5	—	VR
[29]	2010	30	LP	AL	45	1.0	38	—	5.9	—	VR
[30]	2010	10	CP	AL	50	2.3	15	—	—	—	VR
[31]	2010	12	LP	AL	44	50	—	—	—	—	LT
[46]	2008	8.4	CP	RA	54	1.6	20	7	—	—	ER
[44]	2004	7.3	CP	RA	46	7.5	23	—	—	4	ER
[40]	1998	32	CP	RA	60	0.25	28	5.4	3.5	—	ER
[40]	1998	32	CP	RA	69	0.25	22	5.6	3	—	LT
[52]	2010	14	LP	—	71	12	21	9.9	8.0	—	VR
***	2010	12	CP	AL	48	7.1	20	17	8.5	7.0	ER

Table 3.1: Characteristics and measured performance of passive space-fed array prototypes published in literature.

*Measured polarization: circular (CP) or linear (LP)

**Phase shifts created by: element rotation (ER), lengths of transmission line (LT), or varying a resonance frequency (VR)

***This thesis work

— No data available or not applicable

Chapter 4

Analysis and Design of a Circularly Polarized Array Lens Element

As described in the previous chapter, much of the research on space-fed array antennas focuses on the design of the array's elemental unit cell. Many element designs have been presented; each have their own benefits and meet the author's electromagnetic, mechanical, or other criteria. Elements based on microstrip antennas are now the most common type for passive arrays with fixed radiation patterns. These arrays are fabricated by patterning the metal cladding of low-loss printed circuit board laminates.

To provide the necessary phase shifts, the geometry of each microstrip element can be varied from a nominal design. Many authors have scaled part of the geometry to slightly vary the resonance frequency; thus, changing the phase shift at the design frequency. For circularly-polarized space-fed arrays, the phase shifts can be created by changing the element's rotational orientation. This technique is prevalent in modern reflectarray antennas, but more obscure in array lenses. In fact, in 2009 I presented the first array lens element of this type based on a microstrip antenna [1]. The reflectarray elements of this type are all symmetric; one geometry will phase shift either right- or left-hand CP. The previous array lens elements of this type are not symmetric; they consist of counter-wound radiators.

The first section of this chapter presents the analysis of a generic but symmetric

array lens element that uses rotation to provide phase shift for CP. From this analysis, the ideal relationships between the two *linear* polarization transmission coefficients are found. These relationships are used to examine the limiting factors of element bandwidth in Sec. 4.2.

A novel array lens element geometry is presented in Sec. 4.3. The design has many geometrical parameters; thus, the design process is thoroughly explained. Using computational simulations, the transmission coefficients are found to approximate the ideal values over an 18% bandwidth and for incidence angles up to 40° . These simulations analyze a single element; the connection between single-element performance and array properties is discussed.

Finally, a four-element periodic simulation is presented in Sec. 4.4. The results are similar to the single-element simulation; however, they clearly show the lensing effect of the array.

4.1 Using Rotation to Alter Transmission Phase

Under specific conditions, the phase of a wave transmitted through a planar surface can be shifted by in-plane rotation of that surface. The wave must have circular polarization, and the handedness of polarization must change as it passes through the surface. If the surface is discretized into an array lens, the phase of the array weight (ζ_i in Eqn. 2.16) can be selected by the appropriate rotational orientation of that element in the array lattice. These conditions are derived in this section and represent one of the main contributions of this thesis.

4.1.1 Scattering Parameters of a Rotated Array Lens Element

An infinite planar structure discretized into periodic elements is shown in Fig. 4.1. The array is in the xy -plane and has a square lattice of lens elements. Waves traveling in the $-z$ direction are incident on Side 1 of the array. For the periodic analysis of this structure, a single element is surrounded by Floquet boundaries in the x and y directions.

The reflection and transmission properties of this structure can be represented as a scattering matrix. This representation considers each side of the element as a port through which wave energy can enter or exit the system. At each port, the wave energy is typically decomposed into a set of modes—often TE and TM modes. The modal scattering matrix relates the modal amplitudes leaving each port to the modal amplitudes incident on each port. For some problems, not only the propagating modes but also the evanescent modes must be represented in the scattering matrix. However, for a typical array lens antenna, the array is far enough from the feed that only the scattering parameters of propagating modes are required.

As derived in Sec. 2.7.1, when the periodicity of the infinite array is $1/2$ wavelength, only the modes with Floquet index $(0, 0)$ can propagate away from the array. This index corresponds to four electromagnetic modes since one TE and one TM mode can be scattered from each port.

Initially, incidence will be restricted to plane wave modes propagating along the z -axis. The Floquet boundaries are simplified to pure periodic boundaries:

$$\zeta_x = 0 \tag{4.1a}$$

$$\zeta_y = 0. \tag{4.1b}$$

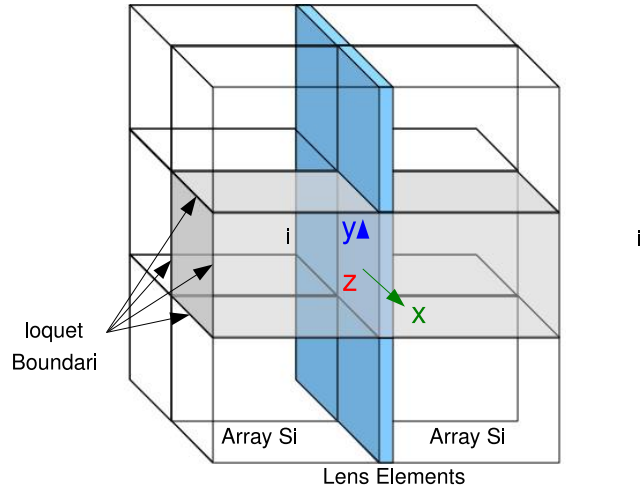


Figure 4.1: The coordinate system of the periodic array lens.

With this restriction, the TE and TM modes scattered from each port are transverse electromagnetic (TEM) to z . Thus, to distinguish between the two modes they are labeled as x -polarized and y -polarized wave modes.

The equation relating these modes is:

$$\mathbf{b}^{\mathbf{XY}} = \mathbf{S}^{\mathbf{XY}} \mathbf{a}^{\mathbf{XY}}, \quad (4.2)$$

where $\mathbf{a}^{\mathbf{XY}}$ is a vector representing the incident modes, $\mathbf{b}^{\mathbf{XY}}$ is a vector representing the scattered modes, and $\mathbf{S}^{\mathbf{XY}}$ is the scattering matrix. The superscript \mathbf{XY} reinforces that this scattering matrix relates linearly polarized wave modes.

If the element is symmetric about all three principle planes, the expanded form of Eqn. 4.2 is:

$$\begin{bmatrix} b_1^x \\ b_1^y \\ b_2^x \\ b_2^y \end{bmatrix} = \begin{bmatrix} \Gamma_x & 0 & T_x & 0 \\ 0 & \Gamma_y & 0 & T_y \\ T_x & 0 & \Gamma_x & 0 \\ 0 & T_y & 0 & \Gamma_y \end{bmatrix} \begin{bmatrix} a_1^x \\ a_1^y \\ a_2^x \\ a_2^y \end{bmatrix}. \quad (4.3)$$

The superscript of each vector component labels the mode as either an x - or y -polarized wave. The subscript of each vector component indicates the port; 1 is the port on the $+z$ side of the element, and 2 is the port on the $-z$ side. In the scattering matrix, Γ_x and Γ_y are the reflection coefficients to x - and y -polarized modes, and T_x and T_y are the transmission coefficients. The zeros in the scattering matrix are due to the symmetry of the element about the xz and yz planes; no energy is scattered into cross-polarized modes for ideal, symmetric elements. The reflection coefficients at Port 1 and Port 2 are equal due to the symmetry about the xy plane.

When the entire structure is rotated about the z -axis by an angle ψ , the transformation to the scattering matrix is:

$$\mathbf{S}_\psi^{\mathbf{XY}} = [\mathbf{R}_\psi^{\mathbf{XY}}]^{-1} [\mathbf{S}^{\mathbf{XY}}] [\mathbf{R}_\psi^{\mathbf{XY}}], \quad (4.4)$$

where $\mathbf{R}_\psi^{\mathbf{XY}}$ is a rotation matrix:

$$\mathbf{R}_\psi^{\mathbf{XY}} = \begin{bmatrix} \cos \psi & \sin \psi & 0 & 0 \\ -\sin \psi & \cos \psi & 0 & 0 \\ 0 & 0 & \cos \psi & \sin \psi \\ 0 & 0 & -\sin \psi & \cos \psi \end{bmatrix}. \quad (4.5)$$

Another scattering matrix can be defined so that it relates circularly-polarized wave modes:

$$\mathbf{b}^{\mathbf{CP}} = \mathbf{S}_\psi^{\mathbf{CP}} \mathbf{a}^{\mathbf{CP}}. \quad (4.6)$$

In expanded form, the vector components are labeled with a superscript that indicates the handedness of polarization; l indicates left-hand circular polarization (LCP)

and r indicates right-hand circular polarization (RCP):

$$\begin{bmatrix} b_1^l \\ b_1^r \\ b_2^r \\ b_2^l \end{bmatrix} = \begin{bmatrix} S_{11}^{lr} & S_{11}^{ll} & S_{12}^{ll} & S_{12}^{lr} \\ S_{11}^{rr} & S_{11}^{rl} & S_{12}^{rl} & S_{12}^{rr} \\ S_{21}^{rr} & S_{21}^{rl} & S_{22}^{rl} & S_{22}^{rr} \\ S_{21}^{lr} & S_{21}^{ll} & S_{22}^{ll} & S_{22}^{lr} \end{bmatrix} \begin{bmatrix} a_1^r \\ a_1^l \\ a_2^l \\ a_2^r \end{bmatrix}. \quad (4.7)$$

For mathematical convenience, the modes in each vector are ordered so that the component that rotates from $+x$ to $-y$ precedes the component that rotates from $+x$ to $+y$. Thus, the components of vectors \mathbf{a}^{CP} and \mathbf{b}^{CP} seem out of order when labeled as l and r . The superscript of each CP scattering parameter is labeled in a similar fashion to the subscript: for example S_{21}^{lr} relates the left-hand component scattered at Port 2 to the right-hand component incident on Port 1.

The scattering matrix for linearly-polarized modes can be transformed into the matrix for circularly-polarized modes by:

$$\mathbf{S}_{\psi}^{\text{CP}} = \mathbf{T}^{\text{XY CP}} \mathbf{S}_{\psi}^{\text{XY}} \mathbf{T}^{\text{XY CP}}^{-1}, \quad (4.8)$$

where $\mathbf{T}^{\text{XY CP}}$ is the coordinate transformation from Cartesian to circular unit vectors:

$$\mathbf{T}^{\text{XY CP}} = \frac{1}{2} \begin{bmatrix} 1 & -j & 0 & 0 \\ 1 & j & 0 & 0 \\ 0 & 0 & 1 & -j \\ 0 & 0 & 1 & j \end{bmatrix}. \quad (4.9)$$

By combining Eqns. 4.4 and 4.8, the values of each CP scattering parameter are

determined:

$$S_{11}^{lr} = S_{11}^{rl} = S_{22}^{rl} = S_{22}^{lr} = \frac{1}{2}(\Gamma_x + \Gamma_y) \quad (4.10a)$$

$$S_{12}^{ll} = S_{12}^{rr} = S_{21}^{rr} = S_{21}^{ll} = \frac{1}{2}(T_x + T_y) \quad (4.10b)$$

$$S_{11}^{rr} = S_{22}^{ll} = \frac{1}{2}(\Gamma_x - \Gamma_y)e^{+j2\psi} \quad (4.10c)$$

$$S_{11}^{ll} = S_{22}^{rr} = \frac{1}{2}(\Gamma_x - \Gamma_y)e^{-j2\psi} \quad (4.10d)$$

$$S_{12}^{rl} = S_{21}^{lr} = \frac{1}{2}(T_x - T_y)e^{+j2\psi} \quad (4.10e)$$

$$S_{12}^{lr} = S_{21}^{rl} = \frac{1}{2}(T_x - T_y)e^{-j2\psi}. \quad (4.10f)$$

Note that the above formulas indicate that when the array lens element is oriented at a rotation angle ψ , four of the above parameters are phase advanced by twice the rotation angle, four are phase delayed by twice the rotation angle, and eight remain unchanged. The phase shifted components are all due to the polarization anisotropy of the element; they are proportional to the difference between T_x and T_y , or Γ_x and Γ_y . The scattering parameters that are unchanged by rotation are all equal to the average of T_x and T_y , or Γ_x and Γ_y .

4.1.2 Ideal Phase-Shifting Element Characteristics

To create a lens using an array, each element is required to alter the phase of the transmitted CP modes. The ideal passive lens element will have no reflection:

$$\Gamma_x = \Gamma_y = 0, \quad (4.11)$$

and lossless transmission:

$$|T_x| = |T_y| = 1. \quad (4.12)$$

As well, the polarization anisotropy will eliminate the scattered fields that are unchanged by rotation angle:

$$T_y = -T_x \quad (4.13)$$

If the lens element properties conform to Eqns. 4.11–4.13 then the scattering matrix is:

$$\mathbf{S}_{\psi}^{\text{CP}} = e^{j-T_x} \begin{bmatrix} 0 & 0 & 0 & e^{-j2\psi} \\ 0 & 0 & e^{j2\psi} & 0 \\ 0 & e^{-j2\psi} & 0 & 0 \\ e^{j2\psi} & 0 & 0 & 0 \end{bmatrix} . \quad (4.14)$$

Circular polarization incident on one port of this element will be scattered from the other port as circular polarization of the *opposite* handedness and phase shifted by an amount proportional to the element's rotation angle. A lens is created by combining many elements into an array and by selecting the rotational orientation angle of each element to provide a phase shift distribution across the array.

4.1.3 Practical Element Characteristics

Practical elements can be designed to approximate the ideal characteristics of Eqns. 4.11–4.13. When practical elements are combined into an array, the lens antenna's performance depends on the quality of the approximation. Furthermore, a practical array will introduce the additional non-ideal conditions described in this section.

The derivation of the scattering parameters in Eqn. 4.10 considers an element contained in an infinite array of identical elements, and it requires that the array lattice rotate along with the element. It also considers only broadside incidence along the z -axis. When used in a lens, these ideal conditions do not exist. Although

the array contains identical elements, the rotation angle of neighboring elements will change their mutual coupling. Therefore, a practical element is one that can be placed in a fixed array lattice, and it will provide phase shift that is proportional to its rotation angle regardless of the rotation of its neighbours. It will maintain acceptable performance across the required bandwidth and for the necessary range of incidence angles. In Sec. 4.3, computational simulations model a novel element designed to approximate Eqns. 4.11–4.13. The incidence angle and frequency are varied to determine the element’s practical limits. In Sec. 4.4, four neighbouring elements with different rotation angles are modeled together in one simulation. This simulation is used to determine if acceptable performance is maintained when the coupling to neighbouring elements is changed.

4.1.4 From Scattering Parameters to Array Weights

Section 4.1.1 derived the scattering parameters of a rotated array lens element. From an antenna design perspective, the important result is the ability to compute the array weight from the scattering matrix. If the mode incident on the lens is a_1^r and the desired scattered mode is b_2^l , the array weight due to each element will correspond to that element’s S_{21}^{lr} parameter:

$$A_i^e = (S_{21}^{lr})_i = \frac{1}{2}(T_{x_i} - T_{y_i})e^{j2\psi_i}, \quad (4.15)$$

If acceptable performance is maintained across the array, the magnitude of the weight is approximately equal for each element:

$$|A_i^e| \approx \frac{1}{2}|T_x - T_y|, \quad (4.16)$$

and the relative phase shift between any two elements is strictly due to the difference in their rotational orientation angles. The relative phase shift between any element i and element 1 is:

$$\zeta_i - \zeta_1 = 2\psi_i - 2\psi_1. \quad (4.17)$$

For convenience, the phase of element 1 is chosen as the phase reference angle, and the orientation of element 1 is chosen as the rotation reference angle:

$$\zeta_1 = 0 \quad (4.18a)$$

$$\psi_1 = 0. \quad (4.18b)$$

Substituting Eqn. 4.18 into Eqn. 4.17 yields the simple, fundamental relationship of the element rotation technique:

$$\zeta_i = 2\psi_i. \quad (4.19)$$

The 2:1 ratio between phase shift and rotational orientation angle holds regardless of the magnitude $|T_x - T_y|$; thus, it will hold over a wide bandwidth. This relationship is used to design the array lens prototypes in Ch. 5.

4.1.5 Scattering Parameters of a Rotated Reflectarray Element

The derivation of the scattering parameters in Eqn. 4.10 also applies to rotated reflectarray elements if they are symmetrical 2-port devices. For a typical 1-port reflectarray element, a similar analysis yields a 2-by-2 scattering matrix that is equal to the upper-left quadrant of the 2-port scattering matrix:

$$\begin{bmatrix} b_1^l \\ b_1^r \end{bmatrix} = \begin{bmatrix} S_{11}^{lr} & S_{11}^{ll} \\ S_{11}^{rr} & S_{11}^{rl} \end{bmatrix} \begin{bmatrix} a_1^r \\ a_1^l \end{bmatrix}. \quad (4.20)$$

The important difference between rotated reflectarray and array lens elements is their ideal characteristics. To create a CP reflectarray, the ideal passive element will have lossless reflection:

$$|\Gamma_x| = |\Gamma_y| = 1, \quad (4.21)$$

and eliminate the reflected modes that are unchanged by rotation:

$$\Gamma_y = -\Gamma_x \quad (4.22)$$

If the reflectarray element properties conform to Eqns. 4.21–4.22, its 1-port scattering matrix is:

$$\mathbf{S}_\psi^{\text{CP}} = e^{j-\Gamma_x} \begin{bmatrix} 0 & e^{-j2\psi} \\ e^{j2\psi} & 0 \end{bmatrix}. \quad (4.23)$$

Circular polarization incident on this element will be reflected as circular polarization of the *same* handedness and phase shifted by an amount proportional to the element's rotation angle. Reflectarray elements are used as examples in Sec. 4.2 to demonstrate the bandwidth for both types of rotated space-fed array elements.

4.1.6 Element Factor

As described in Sec. 2.3.2, the distinction between element factor and array factor is blurred when the element itself is used to phase the array. In this analysis, the element's rotational orientation and transmission coefficients are regarded as part of the array factor and not as part of the element factor. Instead, the element factor is a circularly symmetric pattern that is equal for each element. However, the element pattern does affect the polarization of the radiation pattern. For arrays fabricated on planar PCBs, current in the conductors can only flow in the plane of the array.

A first-order approximation of the current distribution is that it rotates at a single point in the centre of each element. This approximation is good for calculating the polarization of the element factor, but not its shape. Recall from Sec. 2.2 that for large arrays of low-gain elements, the element factor determines the polarization of the far-field radiation pattern whereas the array factor has the largest influence on its shape. Thus, this approximation of the element factor is appropriate for the far-field radiation pattern.

If the desired scattered mode is b_2^l , the element factor is that of an infinitesimal current dipole circulating on the xy plane in the LH sense:

$$(EF)_2^l = \frac{1}{2} \left(\cos \theta \hat{\boldsymbol{\theta}} + j \hat{\boldsymbol{\phi}} \right) e^{-j\phi}, \quad (4.24)$$

where $\hat{\boldsymbol{\theta}}$ and $\hat{\boldsymbol{\phi}}$ are unit vectors in the θ and ϕ directions. The $e^{-j\phi}$ term is simply due to the rotational nature of the coordinate system. At broadside, the element factor is LCP; but, the θ component is decreased in all other directions resulting in elliptical polarization. This effect is typical of CP planar antenna arrays. The elliptical polarization consists of a desired LCP component and an undesired RCP component. Unfortunately, the RCP level will increase as the major lobe is scanned away from broadside, even if the currents on the array are purely LH. The element factor associated with the b_2^r mode is given by:

$$(EF)_2^r = \frac{1}{2} \left(\cos \theta \hat{\boldsymbol{\theta}} - j \hat{\boldsymbol{\phi}} \right) e^{+j\phi}. \quad (4.25)$$

4.2 Element Bandwidth

The bandwidth of array antennas is determined by two factors. First, the array bandwidth is the range of frequencies over which the array factor provides a sat-

isfactory radiation pattern. For space-fed arrays, this limitation was discussed in Sec. 2.3.4. Second, the element bandwidth is the range over which the element performance is satisfactory. For standard arrays, performance is often limited by the input impedance; but for space-fed arrays, it is often limited by the ability of the element to provide the correct phase shift. For reflectarrays and array lenses using element rotation, Eqn. 4.19 indicates that rotation will always give the same phase shift to the desired mode. Therefore, the bandwidth is limited by the ability of the element to scatter a sufficient magnitude of the desired CP mode.

The rotated array lens element will scatter into the desired mode over the frequency range where Eqns. 4.11–4.13 are approximated. Likewise, the reflectarray element bandwidth is limited by the approximation of Eqns. 4.21–4.22. Due to this similarity, a quantitative analysis of element bandwidth is derived for rotated reflectarrays in Sec. 4.2.1, and the result is applied to rotated array lenses in Sec. 4.3.

4.2.1 Rotated Reflectarray Element Bandwidth

The element bandwidth of a rotated space-fed array element is limited by its ability to scatter into the desired CP mode. In this section, a simple reflectarray element is used to illustrate that effect.

A reflectarray element can achieve the conditions expressed by Eqns. 4.21–4.22 if $\Gamma_x = -1$ and $\Gamma_y = +1$. These criteria were used by other authors to design their elements presented in Sec. 3.2.

A conceptually simple element designed to meet these criteria is shown in Fig. 4.2; it consists of a narrow rectangular patch spaced $1/4$ wavelength over a ground plane. The narrow patch acts as a short-circuit dipole and the length of the dipole is chosen

so that $\Gamma_x = -1$. Due to the $1/4$ wavelength separation, the ground plane appears as an open and $\Gamma_y = +1$. This element was first presented in [42].

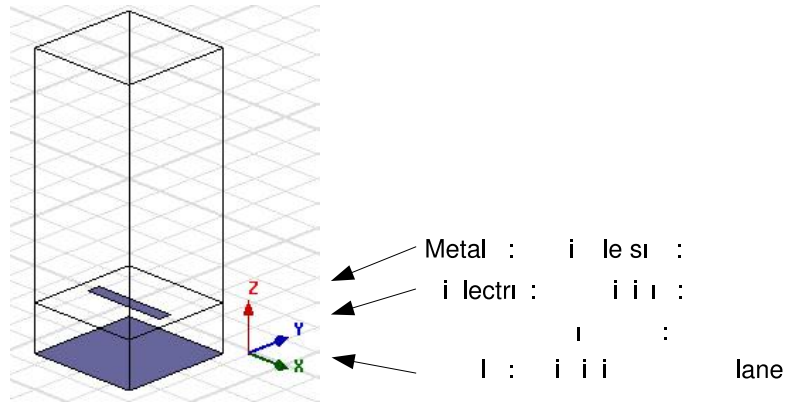


Figure 4.2: Axis and geometry definitions of the reflectarray element. The large box represents the Floquet boundaries and the CP plane wave is incident from the top.

The reflection coefficients will vary with frequency. Modern fixed-beam reflectarray antennas are typically fabricated on PCBs. The use of a ground plane and a low-loss dielectric material allows for the magnitudes of Γ_x and Γ_y to be nominally equal to 1 over a very wide bandwidth. It is the *phase* of Γ_x and Γ_y that have significant variation with frequency. Under these conditions the reflection coefficients can be expressed as:

$$\Gamma_x = e^{j-\phi_x} \tag{4.26a}$$

$$\Gamma_y = e^{j-\phi_y} \tag{4.26b}$$

where $-\phi_x$ and $-\phi_y$ are the reflection coefficient phase angles at a particular frequency.

Substituting Eqn. 4.26 into Eqn. 4.10 gives:

$$S_{11}^{lr} = S_{11}^{rl} = \cos\left(\frac{-\Gamma_x - \Gamma_y}{2}\right) e^{j\frac{1}{2}(-\phi_x - \phi_y)} \quad (4.27a)$$

$$S_{11}^{rr} = j \sin\left(\frac{-\Gamma_x - \Gamma_y}{2}\right) e^{j\frac{1}{2}(-\phi_x - \phi_y)} e^{+j2\psi} \quad (4.27b)$$

$$S_{11}^{ll} = j \sin\left(\frac{-\Gamma_x - \Gamma_y}{2}\right) e^{j\frac{1}{2}(-\phi_x - \phi_y)} e^{-j2\psi} \quad (4.27c)$$

Note that the magnitude of all four scattering parameters depend only on the reflection coefficient phase angle *difference*: $(-\Gamma_x - \Gamma_y)$.

For a_1^r incidence, the desired scattered mode is b_1^r and the undesired cross-polarization mode is b_1^l . Thus, acceptable performance is associated with a magnitude of S_{11}^{rr} near 0 dB and a small magnitude of S_{11}^{lr} . The element bandwidth is the range of frequencies over which these scattering parameters are within specific limits. Four examples of element bandwidth criteria are listed in Table 4.1, and the range of phase difference that fulfills each criteria is calculated from Eqn. 4.27. The range of phase difference that fulfills other bandwidth criteria can be calculated in a similar way. In this analysis, the bandwidth criteria is chosen as $|S_{11}^{rr}| > -1$ dB, which corresponds to a range of phase difference of 126° to 234° . Whichever the choice, bandwidth is not limited to where Γ_x and Γ_y are near -1 and $+1$, but instead to where their phase angle difference is near 180° .

This derivation has reduced the analysis of a rotated reflectarray element to the analysis of its reflection coefficient phase angle difference. However, it should also be noted that the phase average term $(e^{j\frac{1}{2}(-\phi_x - \phi_y)})$ will create dispersion as $-\Gamma_x$ and $-\Gamma_y$ vary, even if their difference remains 180° . For some communication systems, dispersion from the antenna may degrade performance.

Element Bandwidth Criteria	Range of $(-\Gamma_x - \Gamma_y)$
Cross-polarization magnitude: $ S_{11}^{lr} < -20$ dB	$180^\circ \pm 11^\circ$
Cross-polarization magnitude: $ S_{11}^{lr} < -10$ dB	$180^\circ \pm 37^\circ$
Desired polarization magnitude: $ S_{11}^{rr} > -1$ dB	$180^\circ \pm 54^\circ$
Desired polarization magnitude: $ S_{11}^{rr} > -3$ dB	$180^\circ \pm 90^\circ$

Table 4.1: Range of phase difference for common bandwidth criteria

4.2.2 Reflectarray Element Bandwidth Simulation

To illustrate element bandwidth, computational simulation of the reflectarray element in Fig. 4.2 is performed using Ansoft HFSSTM. The parameters for operation at 30 GHz are listed in Table 4.2. The variation of $-\Gamma_x$, $-\Gamma_y$, and their difference are shown in Fig. 4.3. At 30 GHz the reflection coefficients achieve their nominal phase values and the phase difference is 180° . Fig. 4.4 shows the CP reflection magnitudes; as expected, the limits of the -1 -dB- S_{11}^{rr} bandwidth correspond to the frequencies where the phase difference is 126° and 234° . These frequencies are 26.0 GHz and 34.1 GHz corresponding to a fractional bandwidth of 27%.

Table 4.2: Reflectarray element parameters for $1/4$ wavelength separation

Parameter	Value
P_x	4.55 mm
P_y	0.2 mm
ϵ_r	$1.0\epsilon_0$
d	2.5 mm
square lattice	6 mm

The bandwidth analysis can be extended to other geometries. For instance, a dielectric thickness of exactly $1/4$ wavelength may not be feasible or desired; but, this element configuration can still fulfill Eqn. 4.22. Since only the phase *difference* is

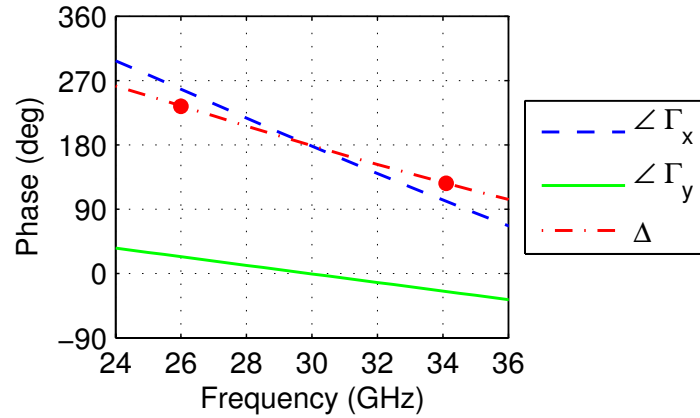


Figure 4.3: Phase of the linear polarization reflection coefficients and their phase difference (Δ). Circles indicate phase difference of 126° and 234° .

important, other thicknesses and dipole lengths can be used. For a $3/8$ wavelength thickness, $\angle \Gamma_y$ is -90° and the dipole must be lengthened to achieve an inductive $+90^\circ$ reflection for $\angle \Gamma_x$. Table 4.3 lists the geometrical parameters and Fig. 4.5 shows the simulated results for this configuration. At 30 GHz, the phase difference is again 180° ; however, the sharper curve of $\angle \Gamma_x$ has increased the frequency at which the phase difference is 234° , and decreased the frequency at which the phase difference is 126° . From Eqn. 4.27, the -1 -dB bandwidth will be the range between these frequencies: 27.4–31.3 GHz (13%). It is interesting to note that the curve has skewed the bandwidth towards lower frequencies.

Table 4.3: Reflectarray element parameters for $3/8$ wavelength separation

Parameter	Value
P_x	5.3 mm
P_y	0.2 mm
ϵ_r	$1.0\epsilon_0$
d	3.75 mm
square lattice	6 mm

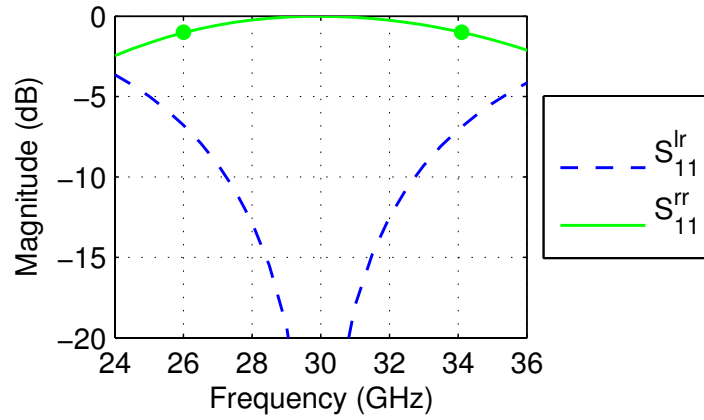


Figure 4.4: Circular polarization scattering parameter magnitudes. Circles indicate the limits of the -1 dB bandwidth.

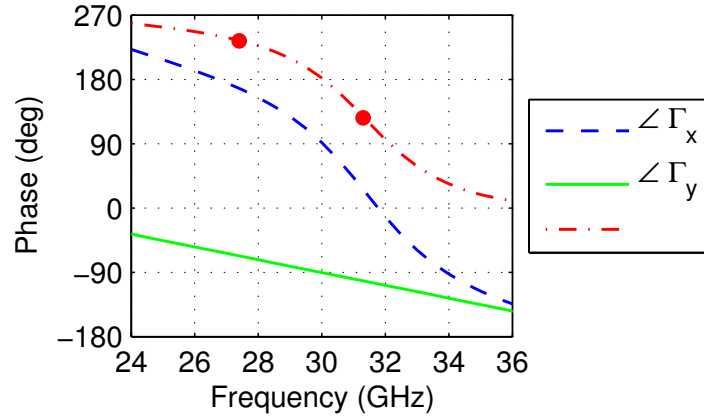


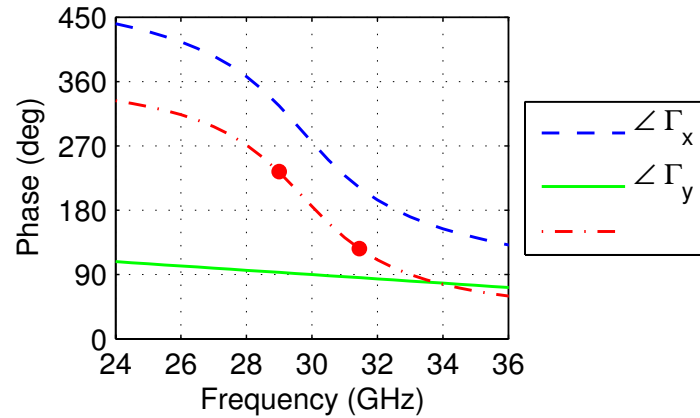
Figure 4.5: Reflection coefficient phases using a $3/8$ wavelength separation. Circles indicate phase difference of 126° and 234° .

For a $1/8$ wavelength thickness, $\angle \Gamma_y$ is 90° and the dipole must be shortened to achieve a capacitive 270° reflection for $\angle \Gamma_x$. As shown in Fig. 4.6, the bandwidth is now 29.0–31.4 GHz (8%). The parameters for this configuration are listed in Table 4.4.

These three configurations of the dipole length and ground-plane separation were

Table 4.4: Reflectarray element parameters for $1/8$ wavelength separation

Parameter	Value
P_x	4.4 mm
P_y	0.2 mm
ε_r	$1.0\varepsilon_0$
d	1.25 mm
square lattice	6 mm

**Figure 4.6:** Reflection coefficient phases using a $1/8$ wavelength separation. Circles indicate phase difference of 126° and 234° .

intuitively designed by creating a phase difference of 180° . The bandwidth was different for each version, but the curves in Figs. 4.3–4.6 give insight into potential approaches for increasing the bandwidth. Unlike other array elements, the bandwidth of rotated reflectarray elements cannot be increased by simply adding another resonance. Instead, the geometry modification must extend the frequency range over which the phase difference is between 126° and 234° . Qualitatively, the modifications must alter the curves of $\angle \Gamma_x$ and $\angle \Gamma_y$ to have similar slope while maintaining a difference of 180° . This design approach is extended to array lens elements in the following sections.

4.2.3 Rotated Array Lens Element Bandwidth

An analysis similar to Sec. 4.2.1 is used to examine the bandwidth of rotated array lens elements. For RCP incidence on Port 1, the desired array lens mode is due to the S_{21}^{lr} parameter. Unlike the reflectarray, the linear polarization transmission coefficients T_x and T_y cannot be immediately assigned nominal magnitudes of 1. The lens elements must be designed to achieve this goal over the required bandwidth. If the definition of acceptable performance is chosen to be: $|S_{21}^{lr}| > -1$ dB, the transmission coefficients must satisfy:

$$\frac{1}{2}|T_x - T_y| > -1 \text{ dB.} \quad (4.28)$$

This is the definition of acceptable performance chosen for this analysis; however, a more stringent or a more relaxed definition could be used if required. Regardless of the choice, acceptable performance requires that the transmission coefficients have magnitudes close to 1 and a phase difference close to 180° .

From this result, two bandwidths are defined for the array lens element: the transmission bandwidth is the range of frequencies over which $|T_x|$ and $|T_y|$ are both above -1 dB; the phase bandwidth is the range over which their phase difference is between 126° and 234° . The overall element bandwidth can be limited by either one. When designing an element, examination of the transmission and phase bandwidths will give insight as to which geometrical modifications can increase the overall array lens element bandwidth.

4.3 Aperture-Coupled Stacked-Patch Element

In Sec. 4.1 it was shown how an array lens element's rotational orientation can shift the phase of its array weight. The element must approximate Eqns. 4.11–4.13 across the required bandwidth and over the necessary range of incidence angles.

One of the contributions of this thesis is an element designed to meet these criteria. As shown in Fig. 4.7, it consists of five metal layers patterned on low-loss PCBs (note that in Fig. 4.7 the separation between layers has been scaled dramatically to illustrate the design). The middle layer is a cross-shaped aperture in a ground plane, and the outer layers are metal rectangles centered on the aperture.

The entire structure acts as an aperture-coupled microstrip-patch antenna, whose operation was described in Sec. 2.5. Here, the aperture does not couple a patch to a transmission line; instead, it simply couples the pair of patches on one side of the ground plane to the pair on the other side. With this geometry, one side of the element can be considered as the inner-surface radiator and the other side as the outer-surface radiator.

To provide phase change, all four patches and the aperture must be rotated together. The geometrical parameters for an element designed to operate at 12.4 GHz are listed in Table 4.5.

The next section presents an analysis of this element. The conceptual operation is supported by computational simulations. Following the analysis, the design process is described in Sec. 4.3.6 and guidelines are given for modifying the element for fabrication on other circuit boards or for use in another frequency band.

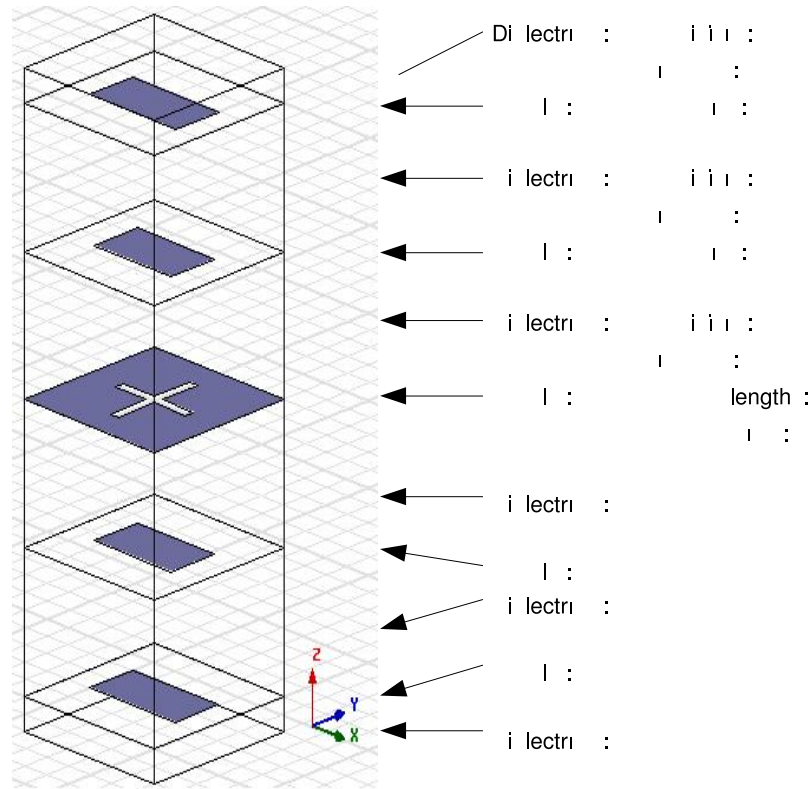


Figure 4.7: Geometry of the aperture-coupled patch element. Parameter values for operation at 12.4 GHz are given in Table 4.5. For these values, the patches and aperture in the image are to scale but the dielectric thicknesses have been exaggerated by a factor of 5.

4.3.1 Patch Element Transmission Bandwidth

The transmission bandwidth is defined as the range over which the magnitude of both linear polarization transmission coefficients are greater than -1 dB. This is achieved by sizing the patches close to half-wave resonance and by dimensioning the aperture to match the element to the incident plane wave.

Computational simulation of a single element is performed in HFSSTM using Floquet excitation and boundaries. The simulation accounts for the loss tangent

Table 4.5: Parameter values of the aperture-coupled patch element

Parameter	Value	Parameter	Value
ε_{r3}	$2.2\varepsilon_0(1 - 0.0004j)$	P_{y1}	4.00 mm
d_3	0.381 mm	ε_{r1}	$2.2\varepsilon_0(1 - 0.0004j)$
P_{x2}	8.00 mm	d_1	1.575 mm
P_{y2}	4.00 mm	A_x	6.46 mm
ε_{r2}	$1.06\varepsilon_0(1 - 0.0001j)$	A_y	7.34 mm
d_2	1.588 mm	A_w	0.75 mm
P_{x1}	7.14 mm	square lattice	12.08 mm

of the dielectrics and the finite conductivity of the copper metal. For broadside incidence, the resulting linear polarization coefficients are shown in Fig. 4.8. Below 6 GHz, neither polarization couples well through the lens element; $|\Gamma_x|$ and $|\Gamma_y|$ are close to 0 dB and $|T_x|$ and $|T_y|$ are low. At 9.3 GHz, the x -polarization is matched; this match is associated with the resonance between the long edge of the patch on Metal 1 and the aperture. At 12.4 GHz, the x -polarization is matched again; this match is associated with the resonance between the long edges of the patches on Metal 1 and Metal 2. The first match for the y -polarization is at 12.5 GHz; this match is associated with the resonance between the short edge of the patch on Metal 1 and the aperture. As this analysis develops, it will be shown that the position of these three resonances—two in x -polarization and one in the y -polarization—are crucial to the element’s operation.

The second y -polarization match associated with the resonance between the short edges of the patches on Metal 1 and Metal 2 occurs around 20 GHz (not shown). A third x -polarization match at 14.3 GHz is associated with a higher-order resonance between the patch on Metal 1 and the aperture. The set of these resonances creates an x -polarization transmission bandwidth of 8.1–14.5 GHz and a y -polarization

transmission bandwidth of 11.8–20 GHz (although the y -polarization does fall slightly below -1 dB). The intersection of these two ranges makes the element’s transmission bandwidth 11.8–14.5 GHz (21%).

The lower end of the transmission bandwidth is limited by T_y , and the upper end by T_x . The transmission bandwidth would be greatly improved by using square patches and equal aperture lengths; however, as discussed in Sec. 4.2.3, the overall element bandwidth is limited by either the transmission or the phase bandwidth. Square patches would not have any phase bandwidth as there would be no phase difference between T_x and T_y .

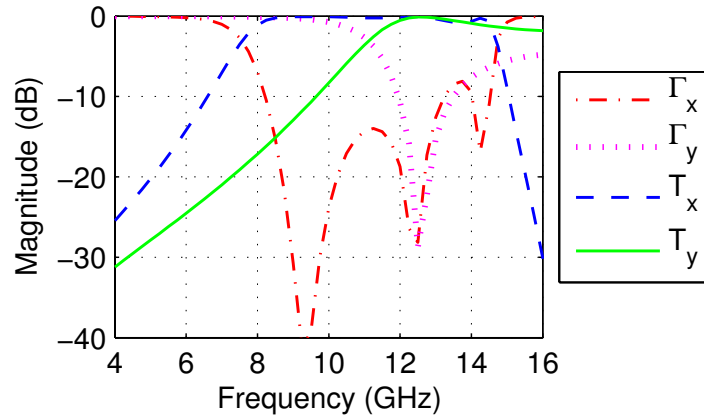


Figure 4.8: Linear polarization reflection and transmission coefficient magnitudes.

4.3.2 Patch Element Phase Bandwidth

By carefully sizing all geometrical parameters, the phase bandwidth can be roughly coincident with the transmission bandwidth. Using rectangular patches allows the phase difference to reach the $180^\circ \pm 54^\circ$ range that defines the phase bandwidth. As the aspect ratio of a rectangular patch increases, the frequencies of the x - and

y -polarized resonances move further apart; the transmission bandwidth decreases but the phase difference between T_x and T_y increases. With a single patch on each side of the ground plane, the resonant frequency shifts required to obtain a phase bandwidth are too large, i.e., the transmission bandwidth becomes narrow before a 180° phase difference is reached.

Using two patches on either side of the ground plane adds another resonance to each linear polarization. The second resonance provides two benefits that enable the element to approximate ideal behaviour over a wide frequency range. First, the extra resonance can increase the transmission bandwidth for each polarization. Second, it adds more phase variation to each transmission coefficient allowing a difference of 180° to be reached more easily.

The simulated transmission coefficient phases, along with their phase difference (Δ), are shown in Fig. 4.9. The transmission coefficients' phase curves follow appropriately from their magnitude curves. Below 6 GHz, neither polarization couples well through the lens element; T_x and T_y are roughly equal. For clarity on the graph, their difference is shown as 360° . The first resonance (9.3 GHz) is for the x -polarization; T_x starts to decrease in the familiar 'S' shape associated with a pole of a transfer function. The phase difference moves towards 180° . As indicated by the circle on the graph, the phase bandwidth begins at 8.8 GHz where the difference crosses 234° . Note that this is *outside* of the transmission bandwidth as the y -polarization is not yet matched. When it is matched at 12.5 GHz, T_y decreases with the same 'S' shape. If each polarization had only a single resonance, the phases would return to being equal and their difference would quickly move away from 180° . However, the second resonance of the x -polarization (12.4 GHz) is placed near the

first resonance of the y -polarization. Although it is difficult to distinguish on the graph, $\angle T_x$ undergoes another ‘S’-shaped decrease. With both $\angle T_x$ and $\angle T_y$ having a similar shape around 12.4 GHz, the phase difference remains at 180° over a wide range. The third resonance of the x -polarization (14.3 GHz) increases the transmission bandwidth above 14 GHz; however, it also adds a final ‘S’ shape to the $\angle T_x$ curve, which pulls the phase difference away from 180° . The circle on the graph at 14.3 GHz indicates the crossing of 126° and the end of the phase bandwidth.

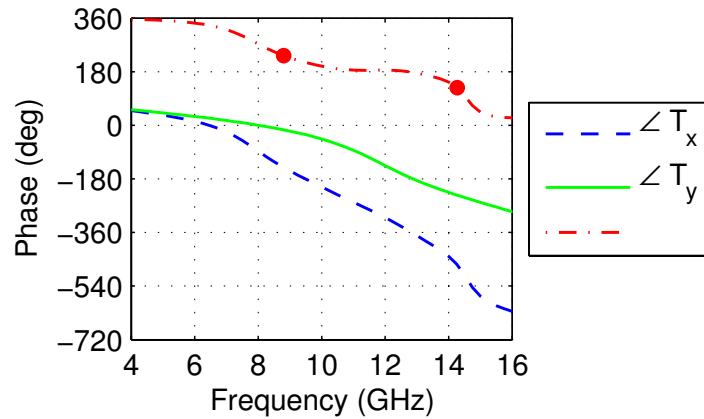


Figure 4.9: Linear polarization transmission coefficient phases and their phase difference (Δ).

The union of the phase bandwidth (8.8–14.3 GHz) and the transmission bandwidth (11.8–14.5 GHz) signifies that the conditions expressed by Eqns. 4.11–4.13 are *all* approximated by the element between 11.8 and 14.3 GHz.

From these linear polarization results, the CP scattering matrix ($\mathbf{S}_\psi^{\text{CP}}$) of this element can be computed from Eqn. 4.10. Magnitudes of four of the CP scattering parameters are shown in Fig. 4.10. These four parameters all relate scattered fields due to RCP incidence on Port 1 (a_1^r). The results shown on this graph can be asso-

ciated with the results of the previous two graphs. Below 6 GHz, the S_{11}^{lr} parameter dominates. The incident RCP does not couple well through the lens; instead, it is reflected as LCP and the element acts as a ground plane. Around 8 GHz, all four parameters are roughly equal. The element acts as linear polarization selective surface: the x -polarization passes through the lens and the y -polarization is reflected.

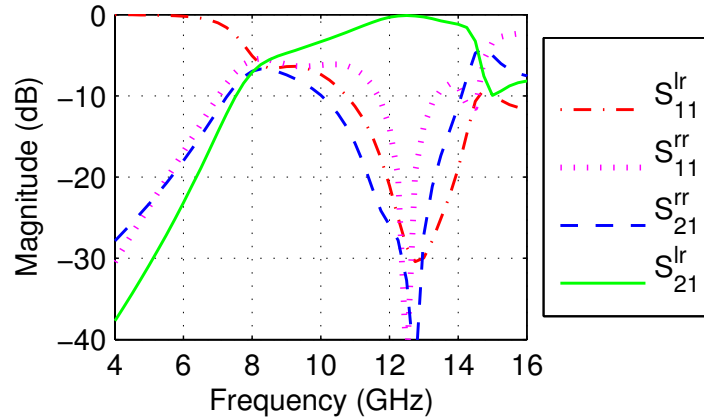


Figure 4.10: Magnitude of the four circular polarization scattering parameters due to a_1^r incidence.

Between 12.4–12.5 GHz the element is very close to ideal. Both linear polarizations are matched and their phase difference is 180° ; thus, the S_{21}^{lr} parameter dominates. The wave is transmitted through the lens and scattered as CP of the *opposite handedness*. Scattering in the other three modes is below -20 dB. The element bandwidth definition given by: $|S_{21}^{lr}| > -1$ dB corresponds to a range of 11.4–13.7 GHz (18%).

This coincides reasonably well with the union of the transmission and phase bandwidths. Over this frequency range, the phase of the array weight due to each element will be twice its rotational orientation angle.

From 15 to 16 GHz an interesting effect is observed. The S_{11}^{rr} parameter is the largest of the four. It corresponds to a *reflection* phase difference close to 180° ; thus, in this range the element acts as the rotated reflectarray element from Sec. 4.2.1.

4.3.3 Effect of Incidence Angle

In the previous section, the practical limits of this element's bandwidth were found to be 11.4–13.7 GHz. Additional simulations are used to determine the practical limits of extending the incidence angle away from broadside. Figure 4.11 shows the variation of $|S_{21}^{lr}|$ due to incidence angle; the polar angle is the angle from broadside, and the azimuth angle is measured from x to y in the xy plane. Due to the symmetry of the element, azimuth angles beyond 180° are not simulated. Note that the transmission magnitude is better than -1 dB for polar angles up to 40° . Thus, the practical limit definition given by $|S_{21}^{lr}| > -1$ dB corresponds to a polar incidence angle limit of 40° .

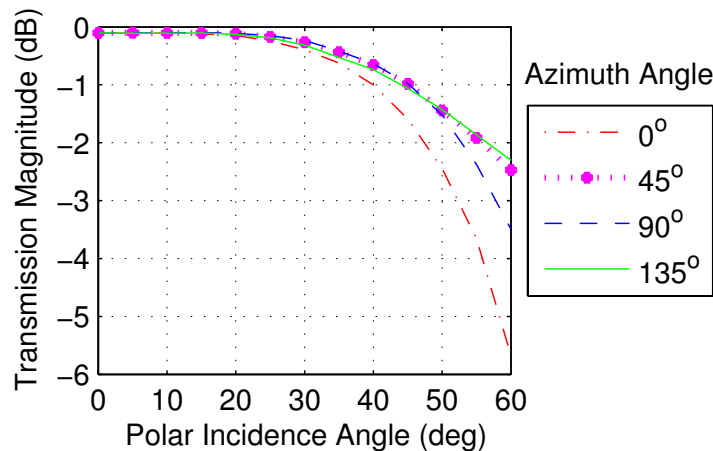


Figure 4.11: Variation of the magnitude of S_{21}^{lr} with incidence angle.

The associated phase variation is shown in Fig. 4.12. The large variation due

to azimuth angle is expected as changing the azimuth angle of the incident field is equivalent to a negative rotation of the element. The phase variation due to polar angle is less than 30° for polar angles up to 40° . These results (Figs.4.11 and 4.12) demonstrate that this element operates successfully over a wide range of incidence angles.

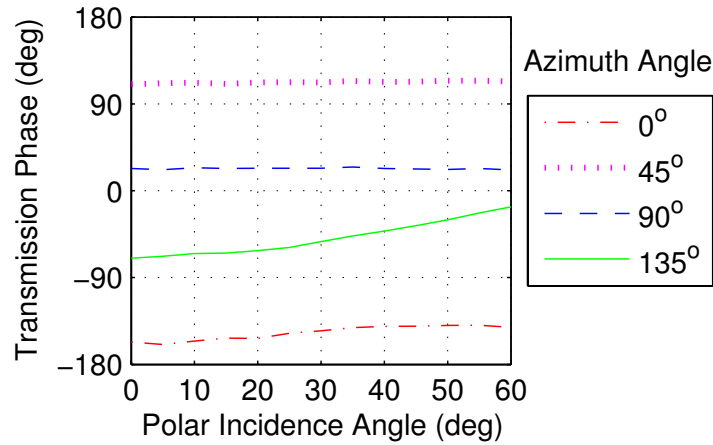


Figure 4.12: Variation of the phase of S_{21}^{lr} with incidence angle.

4.3.4 Effect of Rotation in a Fixed Array Lattice

The previous section showed how the magnitude of the CP scattering parameter limits the polar incidence angle to 40° . Those simulations were performed using an element aligned with the array lattice. In this section, the element's rotational orientation is changed to confirm that the transmitted phase is shifted by twice the rotation angle over a range of incidence angles. The phase shift error is shown in Fig. 4.13. It is calculated by subtracting twice the rotation angle from the transmitted phase angle, and comparing the result to the transmitted phase angle for broadside incidence. At a polar angle of 5° , the relationship between phase and ro-

tation is very close to ideal as the maximum phase error is 3° . The relationship at a 35° polar incidence angle is further from ideal; but, the maximum phase error is still only 16° . These results reinforce that the element approximates ideal behaviour over a wide range of incidence angles.

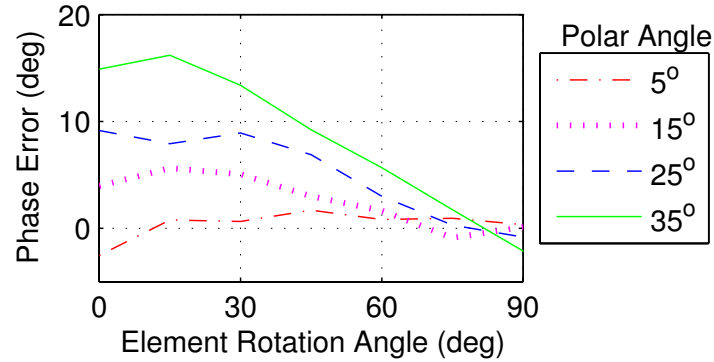


Figure 4.13: Error between the phase of S_{21}^{lr} and the linear phase shift relationship.

4.3.5 Tolerance to Fabrication Errors

Another set of simulations examines the tolerance of the element to fabrication errors. When the dielectric layers are assembled, misalignment can occur between the patches and the aperture. Alignment errors up to 2 mm are examined for each patch in both directions. The largest variation in S_{21}^{lr} occurs when the patch on Metal 1 is misaligned in the x direction. For a 25° polar incidence angle, its magnitude and phase variation are shown in Fig. 4.14; misalignment by 1 mm alters the phase by an additional 4° .

The variations due to layer misalignment in the xy plane are quite small compared with those due to layer separation in the z direction. The aperture is designed to have the same dielectric material on both sides; however, an air gap can form between

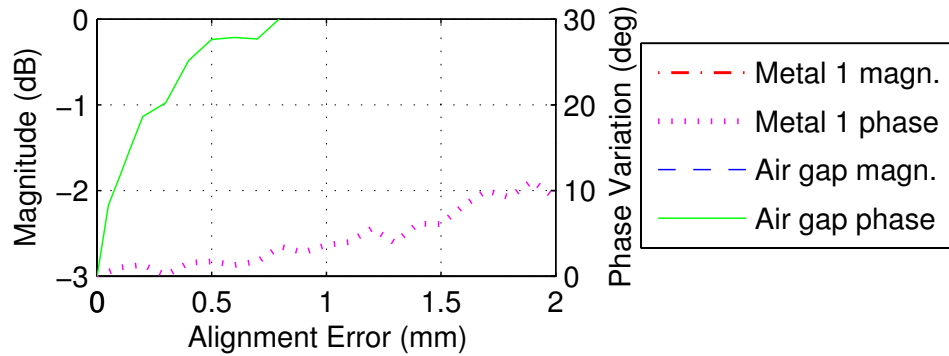


Figure 4.14: Simulation results for 25° polar incidence. Variation of the magnitude and phase of S_{21}^{lr} due to fabrication errors. Two error types are shown: the misalignment in the x direction of the patch on Metal 1, and an air gap between the two Dielectric 1 layers.

the two Dielectric 1 layers during bonding. As shown in Fig. 4.14, this gap can cause a significant variation in both the magnitude and phase of S_{21}^{lr} ; an air gap of 0.5 mm alters the phase by 28° . The results of these simulations indicate that this element has good tolerance to layer misalignment; but, care must be taken to laminate the layers without introducing an air gap.

The simulation results presented in these sections confirm that the aperture-coupled stacked-patch element is a good candidate for a CP array lens. Acceptable performance is maintained over an 18% bandwidth and for incidence angles up to 40° . In these ranges, the magnitude of S_{21}^{lr} is better than -1 dB.

4.3.6 Patch Element Design Process

The parameters of the aperture-coupled stacked-patch element must be chosen carefully. The values presented in Table 4.5 represent a finalized configuration resulting from both knowledgeable design and numerical optimization. The procedure used

to design the element is presented in this section; this procedure can be repeated for use in another frequency band.

There are 14 parameters: three dielectric thicknesses d_1 , d_2 , and d_3 ; three dielectric permittivities ε_{r1} , ε_{r2} , and ε_{r3} ; four patch edge lengths P_{x1} , P_{y1} , P_{x2} , and P_{y2} ; three aperture dimensions A_x , A_y and A_w ; and the square array lattice spacing between elements.

The square array lattice is selected to be $1/2$ wavelength at 12.4 GHz. This element spacing is common in array antennas: it avoids grating lobes, reduces mutual coupling, and provides enough space for the resonant patches. The parameters for Dielectric 1 and Dielectric 2 are selected upon examination of other aperture-coupled and stacked-patch antennas from the literature. Many authors have had success using a low permittivity ($2\varepsilon_0-3\varepsilon_0$) circuit board for Dielectric 1 and a foam sheet for Dielectric 2. The permittivities and thicknesses for these two layers are selected from the readily available stock of microwave material suppliers Rogers Corporation and Emerson and Cuming. Dielectric 3 is designed for functional considerations. Since Dielectric 2 is foam, it is not easy to pattern a metal layer on it. Instead, the Metal 2 layer is patterned on another circuit board: Dielectric 3. This board is selected to have very little electromagnetic influence on the element; it is thin and it has low permittivity. However, it provides a surface upon which to pattern the the Metal 2 layer and it provides structural rigidity for supporting the foam sheet.

With these parameters chosen, the remaining seven parameters are the dimensions of the aperture and patches. The metal itself is the copper cladding of the circuit boards. The aperture width is chosen by scaling the aperture width from [15]. The lengths P_{x1} , P_{x2} , and A_y are chosen to place the first two resonances in

the x -polarization at specific frequencies. The second resonance is placed to create a match at 12.4 GHz—the design frequency—and the first resonance is placed below the design frequency to create the 180° phase difference. The first resonance is influenced mainly by P_{x1} and A_y , whereas the second resonance is influenced mainly by P_{x1} and P_{x2} . Nominal values for these three parameters can be determined by sweeping them individually and observing their effects.

The lengths P_{y1} , P_{y2} , and A_x are chosen to match the y -polarization at the design frequency and maintain a 180° phase difference across a wide frequency band. To ensure the phase difference reaches 180° , the first resonance in y is placed at a slightly higher frequency than the second resonance in x . This resonance is influenced mainly by P_{y1} and A_x ; nominal values for these parameters can be determined by sweeping them individually and observing their effects.

It is well known that the width of a microstrip patch influences its radiation impedance [7, p.734]; thus, varying P_{y1} and P_{y2} will influence the matching of the x -polarization and vice versa. For this reason, the final dimensions of the metal layers cannot be determined individually; instead, they are optimized collectively. The result of the optimization is the set of geometrical parameters listed in Table 4.5. The ‘round’ numbers obtained for P_{x2} , P_{y1} and P_{y2} suggest that these three parameters have a smaller overall impact than the parameters P_{x1} , A_x and A_y . This is consistent with the analysis: P_{x1} influences both x -polarization resonances; A_x influences a resonance and the matching of the y -polarization; and A_y influences a resonance and the matching of the x -polarization. All of these dimensions can be easily fabricated using a photo-lithographic etching process.

One final point should be reinforced: although modification of the geometrical

parameters is used to change resonant frequencies and attain the 180° phase difference, this element does not use variable sizes to create the phase shift distribution across the array. Only one size of element is designed; when its rotational orientation is changed, it can provide any CP phase shift between 0° and 360° .

4.4 Four-Element Periodic Array Lens Simulation

In order to show that a set of rotated elements will create an array lens, four elements are simulated together. As shown in Fig. 4.15, the four elements are arranged in a line and surrounded by Floquet boundaries. Once again, this arrangement simulates an infinite array; however, the additional elements enable the simulation to demonstrate a lens effect rather than simply computing reflection and transmission coefficients. The lens effect is to redirect an incident plane wave into a plane wave travelling in another direction. This effect is created by sequentially rotating each element by 45° , and it is observed by examining the Floquet modal scattering parameters.

This four-element simulation is also used to investigate the coupling between neighbouring elements. The effect that is specifically investigated is the change in scattering properties when the neighbouring elements have different rotation angles. The single-element periodic simulations presented in Sec. 4.3 only modeled arrays where the neighbouring elements had identical rotation angles. For this element to be used in an array lens, the interaction between elements must be sufficiently small such that each element's phase shift depends only on its own rotation angle and not on the rotation angles of its neighbours.

If the element properties depend considerably on the neighbours' having identical

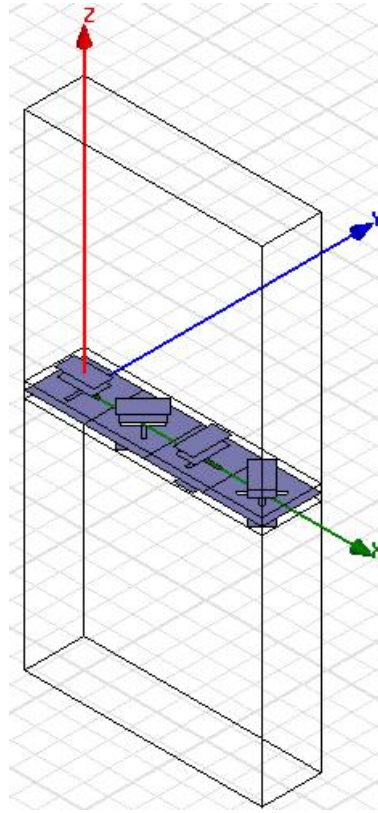


Figure 4.15: Configuration of the four-element simulation. The large box is surrounded by Floquet boundaries.

rotation angles, the change in coupling will be evident in the the four-element periodic simulation. However, if the interaction between elements is small, the scattering from each element in the four-element simulation will be related to the scattering observed in the single-element simulations. For RCP incidence on Port 1 of the array, the scattering parameter magnitudes of all four elements will be given by the data in Fig. 4.10. The phases of the S_{21}^{lr} and S_{11}^{rr} scattering parameters will be different for each element: they will be advanced by twice the element's rotation angle as a result of Eqn. 4.10. These phase changes create scattering in directions other than the incidence and the specular reflection directions. If the element rotations are selected

appropriately, the incident plane wave can be redirected into a desired direction. In the four-element simulation, scattering in another direction is observed as scattering in a mode that has Floquet indexes different from those of the incident mode. The phase of the S_{21}^{rr} and S_{11}^{lr} scattering parameters will be equal for each element since they are unchanged by element rotation.

The four-element structure is analyzed from 10–14 GHz. At the design frequency of 12.4 GHz, the element spacing is $1/2$ wavelength; thus, with four elements in a line the boundaries are separated by:

$$u_x = 2\lambda \quad (4.29a)$$

$$u_y = \frac{1}{2}\lambda. \quad (4.29b)$$

The phase delay between boundaries can be chosen to allow for any incidence angle. In this analysis, they are set to 0° so that broadside incidence is always one of the propagating modes:

$$\zeta_x = 0 \quad (4.30a)$$

$$\zeta_y = 0. \quad (4.30b)$$

The set of propagating modes for this configuration was derived in Sec. 2.7.2. Twelve electromagnetic modes propagate over the entire 10–14 GHz range. These are three Floquet modes for each of the two ports and for both left- and right-hand CP. The Floquet mode indexes are:

$$(m, n) = (0, 0), (+1, 0), (-1, 0) \quad (4.31)$$

The design frequency is the cutoff frequency for the $m = \pm 2$ modes; above it they propagate and below it they are evanescent.

The scattering matrix of propagating modes is 12-by-12 when only the $m = 0, \pm 1$ modes are considered, and 20-by-20 when $m = \pm 2$ are also considered. Rather than examining all 400 scattering parameters, only three incident modes are examined in this section. All are RCP modes propagating in the $-z$ direction and incident on Port 1; but, they are incident at different angles. Using Eqn. 2.44 from Sec. 2.7.2, the $m = 0$ mode is incident at broadside $(\theta_{0,0}, \phi_{0,0}) = (180^\circ, 0^\circ)$ over all frequencies. At the design frequency, the $m = +1$ mode is incident at $(\theta_{+1,0}, \phi_{+1,0}) = (150^\circ, 0^\circ)$ and the $m = -1$ mode is at $(\theta_{-1,0}, \phi_{-1,0}) = (150^\circ, 180^\circ)$. The θ angle of these modes will scan slightly with frequency: from 142° at 10 GHz to 154° at 14 GHz. The incident and scattered modes are labeled by adding the Floquet indexes to the superscript, i.e., the three incident modes are $a_1^{r(m,n)}$ modes. The scattering of each of these modes will be simulated and discussed in the following sections.

4.4.1 $a_1^{r(0,0)}$ Incidence

Ideally, the rotational arrangement in Fig. 4.15 should convert an incident $a_1^{r(0,0)}$ mode into a $b_2^{l(-1,0)}$ mode. From a lens perspective, it should redirect a wave propagating towards $-z$ by 30° . The electric field at a point in time is shown in Fig. 4.16. Specifically, the normal component of the electric field on the Floquet boundary is shown. Both the wave incident at broadside $(180^\circ, 0^\circ)$ and the transmitted wave at $(150^\circ, 180^\circ)$ are clearly visible.

Although all 20 propagating modes are excited by $a_1^{r(0,0)}$ incidence, only four are greater than -10 dB at any frequency from 10–14 GHz. These four modes are shown in Fig. 4.17. The curves in this figure resemble those in Fig. 4.10; this is expected as each of the four dominating modes from this simulation can be attributed to one

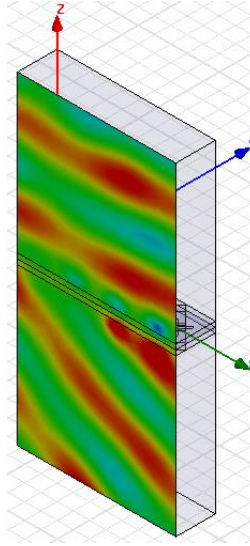


Figure 4.16: The electric field intensity from the four-element simulation. The $a_1^{r(0,0)}$ Floquet mode, incident from the top of the image, is transmitted as a $b_2^{l(-1,0)}$ mode.

of the four modes in the single-element simulation. Note that the four dominating modes consist of one reflected LCP ($b_1^{l(0,0)}$), one reflected RCP ($b_1^{r(-1,0)}$), one transmitted RCP ($b_2^{r(0,0)}$), and one transmitted LCP ($b_2^{l(-1,0)}$) mode. These can be attributed to the single-element scattering parameters S_{11}^{lr} , S_{11}^{rr} , S_{21}^{rr} , and S_{21}^{lr} respectively.

In this four-element simulation, the dominating b_1^r and b_2^l modes are both $m = -1$ modes as they arise from the single-element scattering parameters that are phase shifted by rotation. The $b_2^{l(-1,0)}$ mode is the desired array lens mode. At 12.4 GHz the incident wave at broadside is redirected into this mode with all other modes below -10 dB. This result confirms that these elements can be combined to create an array lens. The $b_1^{r(-1,0)}$ mode is the reflectarray mode generated by the component of reflection in the same handedness as the incidence.

The dominating b_1^l and b_2^r modes are both $m = 0$ modes as they are due to

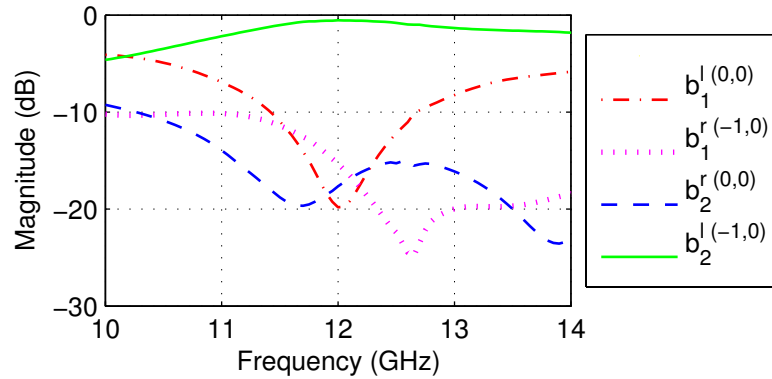


Figure 4.17: Four resulting Floquet mode magnitudes for $a_1^{r(0,0)}$ incidence.

the single-element scattering parameters that are unchanged by rotation. The $b_1^{l(0,0)}$ mode is the specular reflection mode; it is due to the reflection of the element acting as a ground plane. The $b_2^{r(0,0)}$ mode is the direct transmission mode generated by the component of transmission in the same handedness as the incidence.

4.4.2 $a_1^{r(+1,0)}$ Incidence

Ideally, at 12.4 GHz the rotational arrangement in Fig. 4.15 should convert an incident $a_1^{r(+1,0)}$ mode into a $b_2^{l(0,0)}$ mode at broadside. The electric field from this simulation is shown in Fig. 4.18; qualitatively, the lens redirects the wave as required. This confirms that the practical limit of the polar incidence angle is greater than 30° .

Again, all 20 modes are excited but only four are shown in Fig. 4.19. The dominating b_2^l and b_1^r modes are both $m = 0$ modes as they are the array lens mode and the reflectarray mode. The dominating b_1^l and b_2^r modes are both $m = +1$ modes. They maintain the index of the incident mode as they are the specular reflection mode and the direct transmission mode. The four curves are slightly different from

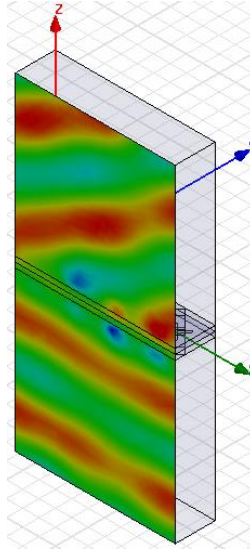


Figure 4.18: The electric field intensity from the four-element simulation. The $a_1^{r(+1,0)}$ Floquet mode, incident from the top of the image, is transmitted as a $b_2^{l(0,0)}$ mode.

those in Fig. 4.17 but they are generally the same shape and level. Since the elements are operating within their practical limits, each of the four dominating modes can again be attributed to the scattering parameters from the single-element simulation. The specular reflection is attributed to S_{11}^{lr} ; the reflectarray mode to S_{11}^{rr} , the direct transmission mode to S_{21}^{rr} , and the array lens mode to S_{21}^{lr} .

These results indicate that the behaviour of a lens whose periodicity spans multiple elements can be approximated by the periodic simulation of a single element. This approximation can be extended to finite or non-periodic array lenses if the incidence angle and the scan angle are kept within the practical limit.

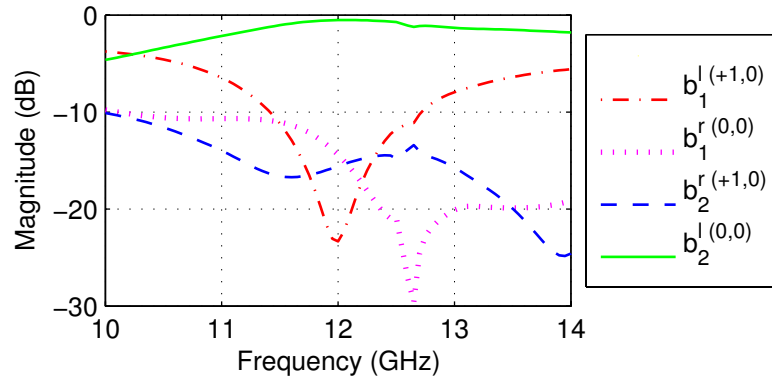


Figure 4.19: Four resulting Floquet mode magnitudes for $a_1^{r(+1,0)}$ incidence.

4.4.3 $a_1^{r(-1,0)}$ Incidence

The rotational arrangement in Fig. 4.15 is attempting to convert an incident $a_1^{r(-1,0)}$ mode into a $b_2^{l(-2,0)}$ mode. At the design frequency, this mode is at the cutoff between end-fire propagation and evanescent wave. Below 12.4 GHz, propagating energy must be scattered into other modes or dissipated in the lens material. Above 12.4 GHz, the desired mode will propagate near end-fire; however, there are two issues to consider. First, the practical limit of the scan angle is exceeded in this configuration. Using reciprocity, it is expected that the practical limit of the scan angle is equal to the 40° limit of the incidence angle. Secondly, this excitation configuration will produce grating lobes.

The electric field is shown in Fig. 4.20. On Side 1 of the array, a standing-wave pattern is observed; on Side 2, the evanescent wave is visible. The excited modes that exceed -10 dB are shown in Fig. 4.21; these curves do not resemble those in Figs. 4.17 and 4.19. The practical limits of the element have been exceeded; thus, it is not possible to maintain an association between the scattering of the four-element

periodic lens and the scattering parameters of a single-element periodic lens. Above 13 GHz the dominant modes are the specular reflection mode, the desired array lens mode, and the grating lobe mode.

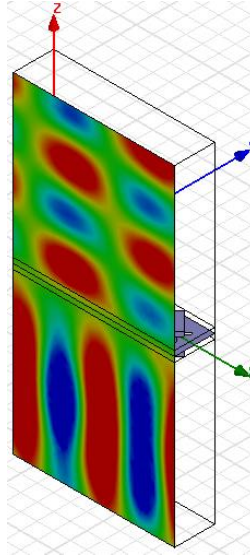


Figure 4.20: The electric field intensity on a surface of the four-element simulation. The $a_1^{r(-1,0)}$ Floquet mode, incident from the top of the image, creates a standing wave on Side 1 and an evanescent wave on Side 2.

4.5 Chapter Summary

Throughout this chapter, the scattering from space-fed array antenna elements was analyzed. The general scattering was represented by a scattering matrix, and then the scattering specific to RCP incidence was examined in further detail.

In Sec. 4.1 a general array lens element was analyzed as a two-port system in which two electromagnetic modes can propagate from each port. When the element's rotational orientation in the xy -plane is changed, half of the scattering parameters are

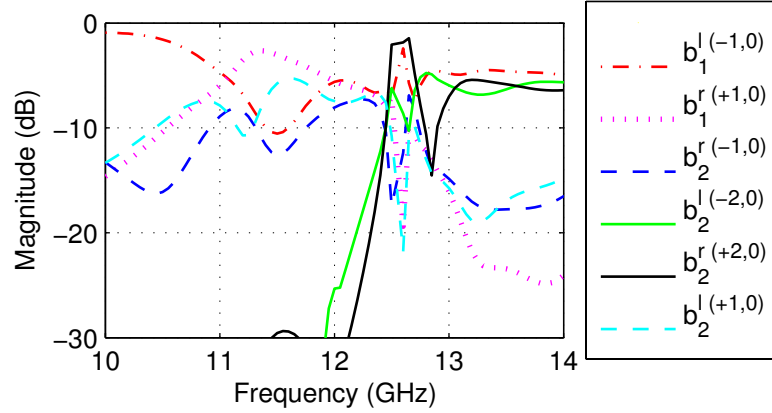


Figure 4.21: Six resulting Floquet mode magnitudes for $a_1^{r(-1,0)}$ incidence.

phase shifted and half are unchanged. The analysis showed that the phase shifting parameters can be attributed to the polarization anisotropy of the element, e.g., the difference between T_x and T_y . This result led to the ideal properties (Eqns. 4.11–4.13) that would allow a rotated lens element to act as a phase shifter.

For right-hand incidence at broadside, phase shift will occur if the element transmits the wave as LCP. The phase shift will be twice the rotational orientation angle; thus, the phase of the array weights can be selected by simply orienting each element at the appropriate angle. Over the entire array, a phase shift distribution will create a lens effect.

The bandwidth for this type of array element was analyzed in Sec. 4.2. As in the previous section, it was noted that the difference between T_x and T_y is crucial to the element's operation. Specifically, the phase difference must be close to 180° over the required bandwidth.

This result provided the insight that led to the development of the aperture-coupled stacked-patch element presented in Sec. 4.3. This element consists of five

metal layers on four low-loss PCBs, as well as two foam sheets. It acts as an aperture-coupled patch antenna for both x - and y -polarization. The cross-shaped aperture does not couple to a transmission line. Instead, the aperture couples the pair of patches on one side of the ground plane to the pair of patches on the other side.

The patches are rectangular; this results in different frequency variation of the two linear polarization transmission coefficients. The bandwidth of this element can be limited by either the magnitude or the phase response of the transmission coefficients. The difficulty in designing the element was to create a 180° phase difference between T_x and T_y while transmitting both components over the same bandwidth. This was accomplished by placing three of the element's resonances at specific frequencies. One resonance to x -polarization and one to y -polarization are placed near the design frequency of 12.4 GHz. An additional resonance to x -polarization is placed at a lower frequency to create the 180° phase difference.

The practical limits of this element were examined. It was found that a single element scatters into the desired mode over an 18% bandwidth and for incidence angles up to 40° . The effects of fabrication errors were studied. The element shows good tolerance to layer misalignment.

The results shown in Sec. 4.4 clearly demonstrate the lens action of an array of rotated elements. The simulations in that section consisted of a periodic array of four elements in a line. If the rotational orientation of each element is selected appropriately, the four-element periodic lens can redirect an incident wave into a different propagating direction. Both the incidence angle and the scan angle of the transmitted wave must be within the 40° practical limit. Under these conditions, the four scattered modes of largest magnitude can be associated with the scattering

parameters from the single-element simulation. This result suggests that the scattering from each element in a finite array lens can be approximated by the periodic simulation of a single element.

In the next chapter, these results are applied to prototype antennas. The lens element used in the prototypes is identical to the one presented in this chapter. The antenna gain, radiation pattern, bandwidth, and cross-polarization level are predicted based on single-element scattering parameters.

Chapter 5

Design, Modeling, and Measurement of Two Prototype Lenses

The previous chapter has shown that the aperture-coupled stacked-patch element satisfies the criteria for use in an array lens. In this chapter, two prototypes are designed using planar arrays of these elements.

The first array, presented in Sec. 5.1, functions as a modified convex lens; it collects radiation from a feed antenna and re-radiates it into a high-gain beam. The complete space-fed array antenna is modeled using a custom three-part simulation technique based on single element scattering parameters. This technique is used to predict the radiation pattern in Sec. 5.1.2, and the aperture efficiency in Sec. 5.1.3. The cross-polarization level and bandwidth of this lens are analyzed in Secs. 5.1.4 and 5.1.5. The prototype is measured in an anechoic chamber and its characteristics (radiation pattern, aperture efficiency, cross-polarization and bandwidth) are presented in Sec. 5.1.6. Guidelines for extrapolating the properties of larger arrays from the prototype results are discussed in Sec. 5.1.7.

The second prototype functions as a Wollaston-type prism; it splits an incident wave into two beams according to the ratio of its CP components. This lens is analyzed in Sec. 5.2 and its measured radiation pattern is presented in Sec. 5.2.1.

Both arrays are designed for operation at 12.4 GHz and their elements have the geometrical parameters listed in Table 4.5. The total thickness of the six di-

electric layers is 7.1 mm. The materials used to assemble the lenses are: Rogers RT/duroid® 5880 for Dielectric 1 and Dielectric 3, and Emerson and Cuming® Eccostock PP-4 foam for Dielectric 2. With these materials, the mass per unit area of each lens is 0.91 g/cm².

5.1 Modified Convex Lens Prototype

This lens is designed to collect the RCP radiation from a horn antenna and redirect it into a high-gain LCP beam. The array elements are spaced by a half wavelength (12.08 mm) in a square lattice. The boundary of the array is circular and 349 elements are needed to fill the 254 mm diameter circle. The array of square elements creates a staircase approximation to the circle; thus the actual area of the aperture is:

$$s = 349(12.08 \text{ mm})^2 = 509 \text{ cm}^2 \quad (5.1)$$

Each element's rotational orientation is selected to provide a phase shift distribution across the array. For this specific lens, the phase shift has two functions: firstly, it compensates for the spatial delay between the feed horn and the array surface; and secondly, it creates a linear phase gradient which directs the major lobe to $(\theta_d, \phi_d) = (160^\circ, 0^\circ)$, which is 20° from broadside transmission. To accomplish this, the phase shift distribution of A_i (the array weight provided by each element) is selected according to Eqn. 2.19. Any phase shift distribution can be synthesized, including distributions that create multiple-beam or contoured-beam radiation patterns. Choosing the distribution created by Eqn. 2.19 demonstrates the ability of an array lens to provide a specialized fixed-beam pattern.

From this equation, the largest relative phase shift between two elements is 1330° . Element rotation can provide a relative phase shift of 0° to 360° ; thus, the phase shift provided by the array is similar to that of a zoned lens. To achieve this phase shift distribution, each element's rotational orientation is set according to:

$$\psi_i = \frac{\omega_0}{2c} \left(\sqrt{F^2 + x_i^2 + y_i^2} - x_i \sin 160^\circ \cos 0^\circ \right), \quad (5.2)$$

where ψ_i is the rotation of element i at position (x_i, y_i) , the design frequency is ω_0 , c is the speed of light and F is the lens focal length. The $1/2$ multiplier compensates for the 2:1 relationship between phase shift and rotation (Eqn. 4.19). The left image in Fig. 5.1 shows the geometrical pattern of the Metal 2 layer for this array.

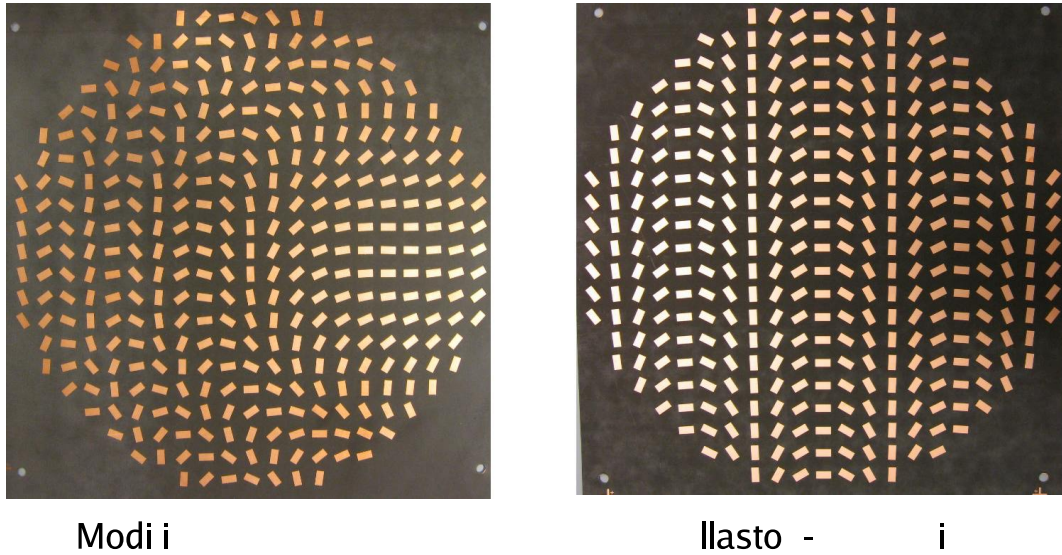


Figure 5.1: The entire Metal 2 layer of each lens. The element rotations are set according to Eqn. 5.2 and Eqn. 5.16. The diameter of both lenses is 254 mm.

The feed antenna is a pyramidal horn with a gain of 15 dB at 12.4 GHz. It is placed such that it is in line with the centre of the array and the F/D ratio of the

space-fed antenna is 0.81. Note that the horn was not designed as a feed antenna but that the F/D ratio of the array was selected specifically for use with this horn. The median polar incidence angle onto an element is 24° and the maximum angle is 32° , which is less than the 40° limit determined in Sec. 4.3.3.

As shown in Fig. 5.2, a rigid plastic frame is used to mount both the lens and the feed horn for anechoic chamber measurements. To facilitate mounting, the lens is printed on rectangular circuit boards; but, the metalization of the lens (including the ground plane) is contained within the staircase approximation of a circle.

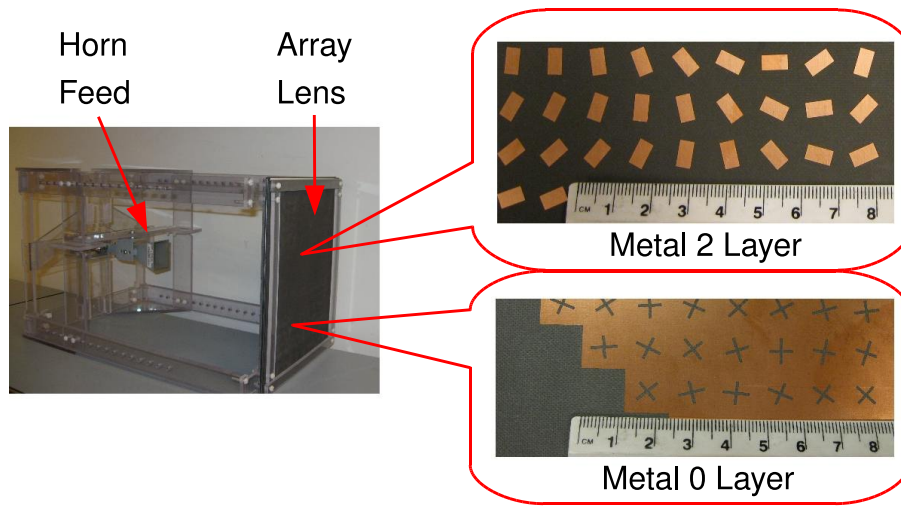


Figure 5.2: The modified convex lens and feed horn are mounted in a plastic frame. Details of the Metal 0 and Metal 2 layers are shown. The ruler measures centimetres.

5.1.1 Antenna Simulation

The array lens is an electrically large antenna but each element has fine geometrical details. This range of sizes makes it difficult to perform a computational electromagnetic simulation of the entire antenna. In this work, the analysis is broken down

into smaller tasks by assuming local periodicity for each element. The elements are considered to be in their own infinite array environment and they are analyzed individually. The simulation consists of three steps:

1. Radiation from the feed horn is modeled to determine the incident fields on each element
2. A scattering matrix is calculated for each element
3. Finally, the scattered fields from each element are combined to determine the antenna radiation pattern and gain.

Full-wave commercial software packages are used to simulate both the feed and the array elements. These two tasks require two different types of analysis: simulation of the feed models a source radiating into free space; whereas simulation of each element models plane wave excitation of a periodic surface. Many software packages can perform both of these tasks. In this work, I chose to use two different packages (one for each task) as I have more experience in using one package for each of the two types of problems.

5.1.2 Radiation Pattern Calculation

The FEKOTM software package is used to simulate the feed horn transmitting into free space. Electric and magnetic field components are determined in the plane of the array, specifically at the 349 points that will be at the centre of each element. The Poynting vector is computed at these points and its direction is used as the element's incidence angle. The fields at each point are translated into a coordinate system aligned with the Poynting vector at that point. In this coordinate system, the

incident electric fields are decomposed into a transverse RCP wave (a_1^r), a transverse LCP wave (a_1^l), and a radial field component parallel to the Poynting vector. The radial field component is always at least 30 dB smaller than the other components confirming that the array is placed outside of the horn's near field region.

The discussion on radiation pattern of space-fed arrays in Sec. 2.3.2 considered the array weight *due to the feed* as the magnitude and phase of the electric field in the desired polarization incident on each element (Eqn. 2.12). For this lens, it is:

$$A_i^f = (a_1^r)_i \quad (5.3)$$

The amplitude and phase of the simulated a_1^r are illustrated in Fig. 5.3a)–b). These patterns are typical of a horn antenna.

For each element, calculation of a unique scattering matrix ($\mathbf{S}_\psi^{\text{CP}}$) is required. Every matrix is unique as each element has a different incidence angle and has been rotated to provide a different phase shift. The four element simulation discussed in Sec. 4.4 demonstrated that the scattering properties of one element can be approximated using the results of a single element periodic simulation even if its neighbours have different rotation angles. This result implies that the coupling between elements is small enough that the neighbours' specific rotation angles can be ignored. Thus, to analyze the prototype lens, each element's scattering matrix is calculated using results of single element periodic simulations in Ansoft HFSSTM.

For a typical application, this type of antenna could have many thousands of elements and so a method is devised to approximate each element's scattering matrix using only a small number of simulations. The first approximation is to consider the effect of counter-clockwise element rotation to be equal to the effect of clockwise

change in azimuth incidence angle. To determine each scattering matrix, the difference between the actual azimuth incidence angle and the actual element rotation angle is used as the simulated azimuth incidence angle, and the simulated rotation angle is set to 0° . This is a good approximation; however, the coupling to neighboring elements is not represented exactly in this approach.

The second approximation is to simulate only specific incidence angles and interpolate the results. Polar angles from 0° to 35° in 5° steps, and azimuth angles from 0° to 165° in 15° steps requires 96 simulations. Due to the geometrical symmetry, azimuth angles beyond 180° need not be simulated, as they are equivalent to those below 180° . From these 96 simulations, the scattering matrices for 96 incidence angles are determined. The scattering matrix for the specific incidence angle associated with each element of the lens is found using a two-dimensional interpolation between four of the 96 simulated incidence angles. By interpolating, the scattering matrices for the thousands of elements in a typical application could be quickly evaluated.

In Sec. 4.1.4, the array weight *provided by the element* was identified as the S_{21}^{lr} scattering parameter (Eqn. 4.15). Interpolated values of S_{21}^{lr} for each element are illustrated in Fig. 5.3c)–d). For most elements, the magnitude of S_{21}^{lr} is close to 0 dB; however for some elements near the edge of the array it is below -0.5 dB. The interesting phase shift pattern is required to steer the resulting beam to 20° off of broadside.

The *total* array weight is the magnitude and phase of the LCP component transmitted through the array.

$$A_i = (b_2^l)_i \quad (5.4)$$

For the *ideal* element, b_2^l results from a single scattering parameter:

$$(b_2^l)_i = (S_{21}^{lr})_i (a_1^r)_i. \quad (5.5)$$

Thus, the total array weight of the ideal element is simply the product of the array weight due to the feed and the array weight provided by the element. On the contrary, b_2^l of the *practical* element results from the scattering matrix. For incidence on only Side 1, it consists of two terms:

$$(b_2^l)_i = (S_{21}^{lr})_i (a_1^r)_i + (S_{21}^{ll})_i (a_1^l)_i. \quad (5.6)$$

The first term is the desired component of the total array weight. The additional term consists of the cross-polarized a_1^l incidence from the feed multiplied by the direct transmission scattering parameter S_{21}^{ll} .

Equation 5.6 is used to combine each element's incident field from the FEKOTM simulation and its scattering matrix interpolated from the HFSSTM simulations. This calculation is performed using a custom software code. Values of b_2^l are illustrated in Fig. 5.3e)–f). The amplitude distribution is similar to that of the feed horn and the horizontal phase gradient will steer the major lobe to 20° from broadside. The custom code also transforms the scattered fields into a radiation pattern. Cuts from this calculated pattern are compared to measurements in Sec. 5.1.6.

5.1.3 Aperture Efficiency Calculation

This antenna is designed to have high gain but there are many factors that decrease its aperture efficiency. The main factors are: power spillover from the feed, tapered amplitude distribution, scanning loss, and non-ideal transmission through the lens.

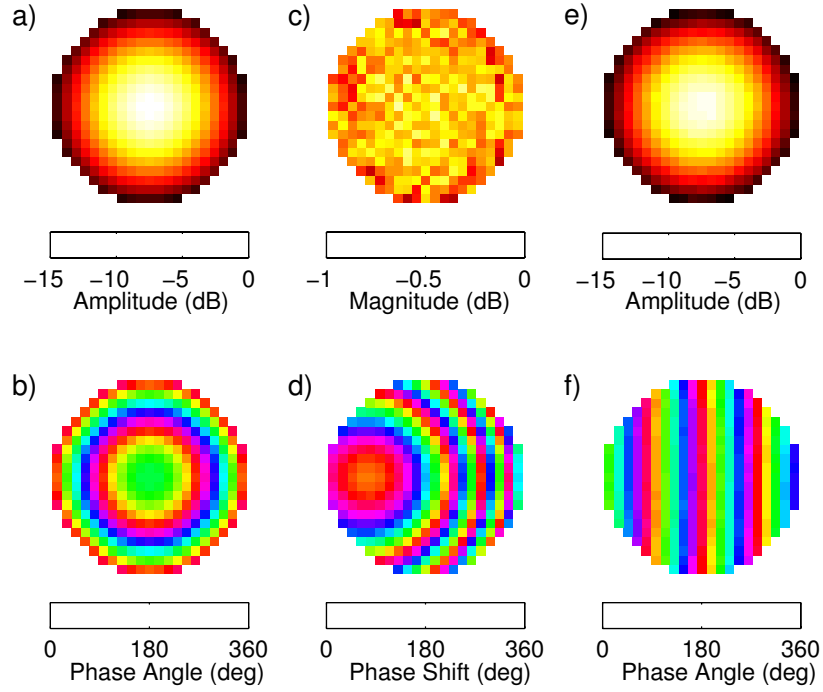


Figure 5.3: Simulation of the lens when excited by the feed horn. Each pixel represents one of the 349 elements. a) Magnitude of a_1^r . b) Phase of a_1^r . c) Amplitude of S_{21}^{lr} . d) Phase of S_{21}^{lr} . e) Amplitude of b_2^l . f) Phase of b_2^l .

Results from the simulations used to predict the radiation pattern are reused to predict these efficiencies. The spillover efficiency is calculated by applying Eqn. 2.20:

$$\epsilon_{sp} = \frac{\sum_{i=1}^{349} [\mathbf{W}_f(\mathbf{p}_i) \cdot \hat{\mathbf{z}}] (12.08 \text{ mm})^2}{P_{rad}}. \quad (5.7)$$

Both $\mathbf{W}_f(\mathbf{p}_i)$, the radiation power density at each element, and P_{rad} , the total power radiated by the horn, are obtained from the FEKOTM simulation.

The remaining efficiencies are calculated by applying the 349 elemental scattering matrices onto the incident fields. The transmission efficiency is determined by comparing the total power scattered on Side 2 of the array to the power incident on

Side 1:

$$\epsilon_{tr} = \sum_{i=1}^{349} \left(\frac{|b_2^r|_i^2 + |b_2^l|_i^2}{|a_2^r|_i^2 + |a_2^l|_i^2} \right). \quad (5.8)$$

The polarization efficiency considers only the power scattered in the desired component:

$$\epsilon_{po} = \sum_{i=1}^{349} \left(\frac{|b_2^l|_i^2}{|b_2^r|_i^2 + |b_2^l|_i^2} \right). \quad (5.9)$$

The phase error efficiency is calculated from the b_2^l components according to [10, p.138].

$$\epsilon_{ph} = \frac{(1 + \cos 20^\circ)^2}{4} \frac{\left| \sum_{i=1}^{349} (b_2^l)_i e^{j \frac{\omega}{c} (x_i \sin 20^\circ)} \right|^2}{\left(\sum_{i=1}^{349} |b_2^l|_i \right)^2}. \quad (5.10)$$

Note that this definition of phase error includes the 20° scanning loss. Finally, the taper efficiency is calculated from Eqn. 2.21:

$$\epsilon_{ta} = \frac{\left(\sum_{i=1}^{349} |b_2^l|_i \right)^2}{349 \sum_{i=1}^{349} |b_2^l|_i^2}. \quad (5.11)$$

The total aperture efficiency is simply the product of the constituents:

$$\epsilon_{ap} = \epsilon_s \epsilon_{tr} \epsilon_{po} \epsilon_{ph} \epsilon_{ta}, \quad (5.12)$$

and the predicted gain is:

$$G = G_{ap} \epsilon_{ap} = \left(4\pi \frac{S}{\lambda_0^2} \right) \epsilon_{ap}. \quad (5.13)$$

A summary of the calculated constituents for this antenna are listed in Table 5.1. As discussed in Sec. 2.1.1, the F/D ratio of 0.81 was chosen as a trade-off between the

Table 5.1: Calculated constituents of aperture efficiency

Efficiency Type	Value (%)	Loss (dB)
spillover	84	0.8
transmission	93	0.3
polarization	95	0.2
phase error	93	0.3
taper	81	0.9
total aperture	56	2.5

spillover and taper efficiencies; together, they reduce the potential gain by 1.7 dB. Reflection and loss in the lens material reduce the power transmitted through the lens by 0.3 dB. Cross-polarization transmission causes a further reduction of 0.2 dB. The total phase error loss is 0.3 dB; but, choosing to scan the major lobe to 20° reduces the effective area to 94% of the physical area. This reduction constitutes the majority of the phase error efficiency. The sum of all the losses is 2.5 dB, which corresponds to an aperture efficiency of 56% and a gain of 27.9 dB at 12.4 GHz. These values are compared to measurements in Sec. 5.1.6.

5.1.4 Cross Polarization Selectivity

A convex lens using an array of rotated elements will be circular polarization selective. Only one handedness of CP will be focused and the other handedness will not, i.e., the lens must be designed to focus either RCP or LCP. However, this limitation can improve the cross-polarization level of the entire antenna. This effect is described in this section.

The modified convex lens prototype is designed to focus incident RCP from Side 1 into an LCP beam on Side 2. Thus, the cross polarization is the RCP component scattered from Side 2 (b_2^r). As with the desired LCP component (Eqn. 5.6), the RCP

is due to two terms:

$$(b_2^x)_i = (S_{21}^{rr})_i(a_1^r)_i + (S_{21}^{rl})_i(a_1^l)_i. \quad (5.14)$$

The first term consists of the desired a_1^r incidence from the feed multiplied by the direct transmission scattering parameter S_{21}^{rr} . This cross-polarization term is due to non-ideal properties of the element. Recall that the phase of the S_{21}^{rr} parameter is not changed by element rotation (Eqn. 4.10). Thus, between two elements the relative phase of their scattered field is equal to the relative phase of their incident field. Across the array, the transmitted phase distribution will be the same as the phase distribution from the feed. Thus, the cross-polarization term due to non-ideal properties of the element will not be focused by the lens.

The second term consists of the cross-polarized a_1^l incidence from the feed multiplied by the array lens scattering parameter S_{21}^{rl} . This cross-polarization term is due to non-ideal properties of the feed. Recall that the phase of S_{21}^{rl} is changed by element rotation; but it has the *opposite* sign as S_{21}^{lr} . Instead of correcting the phase delays from the spatial feed, this scattering parameter will change the phase in the opposite direction. Thus, the cross-polarization due to the feed will be diffused by the lens.

Neither cross-polarization term will be focused by the lens. As the area of the lens increases, the gain of the desired polarization will increase proportionally according to Eqn. 5.13. On the other hand, the gain of the cross polarization will not increase proportionally as it will remain spatially diffused. The ratio of the lens gain to the cross-polarization level should improve as the area of the lens increases. This ratio is known as the cross-polarization discrimination (XPD) of the antenna. Due to this effect, the XPD of a focusing array lens can be better than the XPD of a

single element. The cross polarization selectivity provided by the element rotation technique is a major advantage over other array phasing techniques. This selectivity was first observed in a reflectarray prototype [40]. This section has presented an analysis of the cross-polarization selectivity, and it has shown that it also applies to array lenses.

5.1.5 Prototype Bandwidth

Recall that the antenna bandwidth of a space fed array can be limited by either the array bandwidth (Sec. 2.3.4) or the element bandwidth (Sec. 4.2). Eqn. 2.29 predicts a limit on the product of array bandwidth and aperture diameter to be a function of the F/D ratio and the maximum acceptable value of phase difference between centre and edge elements. The diameter of the modified convex lens is 10.5 wavelengths and the F/D ratio is 0.81. For a maximum acceptable phase difference of $\pi/2$, the array bandwidth is limited by:

$$10.5B \leq \frac{1}{2}(0.142)^{-1}, \quad (5.15)$$

corresponding to a maximum array bandwidth of 34%. In Sec. 4.3.2 the single-element simulations predicted an element bandwidth of 18% (11.4–13.7 GHz). Thus the prototype bandwidth is expected to be limited by the element bandwidth.

5.1.6 Antenna Measurements

The lens assembly is mounted in a 3.4 m far-field anechoic chamber that is available to me at the University of Calgary; however, for this antenna, the boundary between the radiating near-field region and the far-field region occurs at 5.3 m [7, p.33]. To

compare the measured radiation pattern with the pattern predicted by the simulation in Sec. 5.1.2, the fields scattered from the array in the simulation are transformed into a radiation pattern that is also calculated at a 3.4 m distance. This is done by accounting for the length difference between each element and the observation point at 3.4 m. For a true far field calculation, the distance from each element to the observation point (at infinity) is equal.

Azimuth and elevation cuts of the radiation pattern are shown in Figs. 5.4 and 5.5. The angular coordinate system of the measurement is selected so that both radiation pattern cuts pass through the major lobe. The azimuth pattern cut is in the xz plane and contains the broadside direction. The elevation cut is perpendicular to the azimuth cut but it is not in any principle plane; it passes through the major lobe but not through broadside. In this coordinate system, the desired beam direction is at a -20° azimuth angle and a 0° elevation angle.

For both cuts, the LCP component shows the major lobe pointing in the desired direction. The measured 7° half-power beamwidth matches that predicted from simulation; however, the side-lobe levels are higher. This is potentially due to two types of errors. First, the assembled lens may deviate from the simulated lens geometry. Misalignment of the dielectric layers, and air gaps between layers have negative effects. Secondly, the infinite periodicity simulations may not correctly model the perimeter elements.

The cross-polarization component (RCP) is 6 dB higher than predicted in the beam pointing direction, and is even further from predicted in other directions. However, across both pattern cuts it is at least 20 dB below the level of the major lobe. As discussed in Sec. 5.1.4, low cross-polarization levels are predicted for this

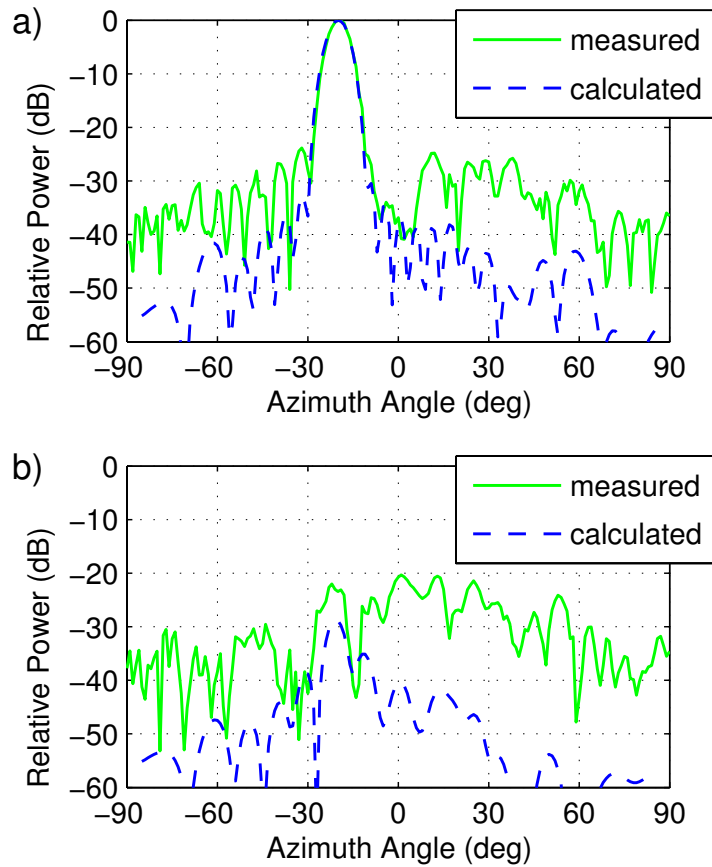


Figure 5.4: Azimuth cut of the radiation pattern: a) LCP component, b) RCP component.

antenna as the associated scattering parameters (S_{21}^{rr} and S_{21}^{rl}) do not apply the phase shifts necessary to compensate for the spatial delay between the feed and the array surface.

The reflection coefficient at the input to the horn was measured both with and without the lens. It is shown in Fig. 5.6 and includes the effect of the coax-to-waveguide adapter. The additional nulls confirm that a wave does reflect from the lens back into the horn.

Although the major lobe points to an azimuth angle of -20° at 12.4 GHz, that

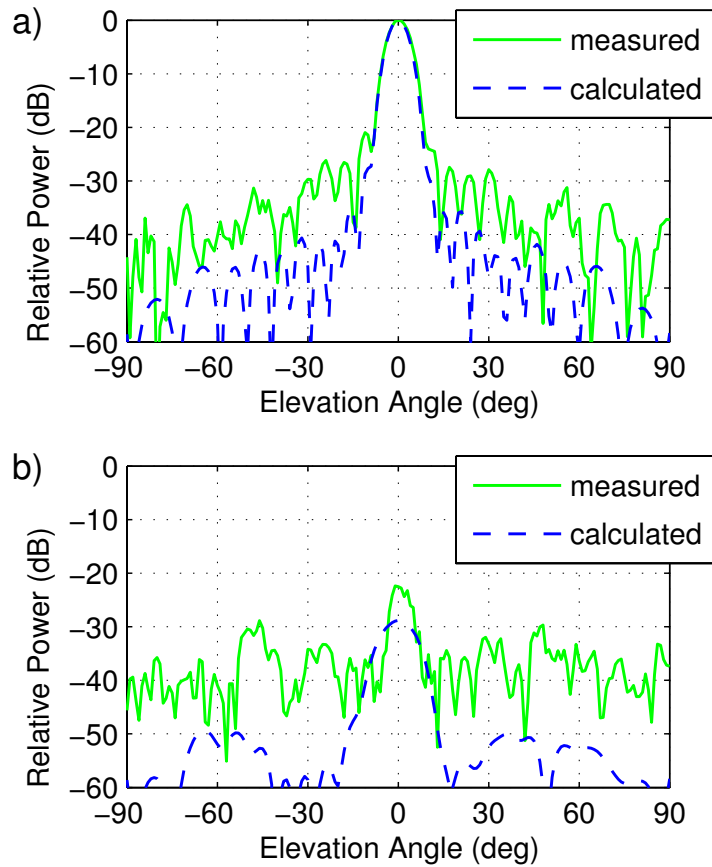


Figure 5.5: Elevation cut of the radiation pattern: a) LCP component, b) RCP component. The cut is located so that it passes through the major lobe.

angle will scan with frequency. The beam direction is defined as the angle with the largest measured radiation intensity. Since the mechanical step size of the azimuth turntable is 1° , the beam direction is measured to the nearest degree. As shown in Fig. 5.7, it points to -22° at 11.0 GHz and at 13.5 GHz it has scanned to -18° . This curve should be monotonically increasing; the oscillations are due to measurement errors.

The antenna gain, aperture efficiency, and axial ratio are calculated in the beam

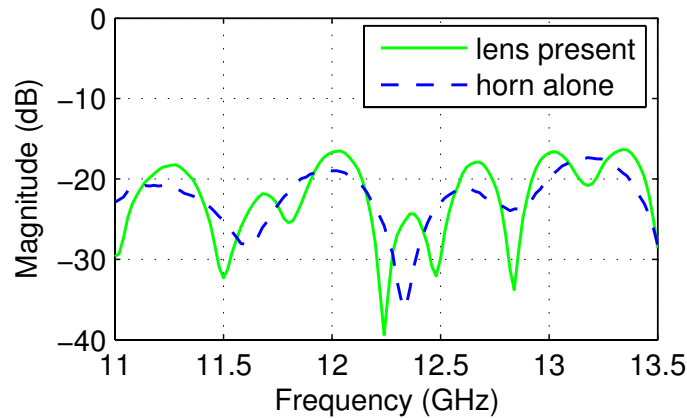


Figure 5.6: Reflection coefficient measured at the coax connector to the horn.

direction. The gain is shown in Fig. 5.7; it reaches a peak of 27.6 dB at 12.9 GHz. This is close to the predicted peak gain of 27.9 dB, but it occurs above the 12.4 GHz design frequency. The gain is relatively constant over the measured range of frequencies. The lower end of the -3 -dB-gain bandwidth (11.4 GHz) coincides with the lower end of the predicted bandwidth. However, it should be noted that these two bandwidths are limited by different criteria. The upper limit of the -3 -dB-gain bandwidth is not evident in the measurements; setting the limit at 13.5 GHz corresponds to a bandwidth of 17%.

The aperture efficiency and axial ratio are shown in Fig. 5.8. Throughout the -3 -dB-gain bandwidth the aperture efficiency is better than 30% and the axial ratio is better than 3 dB. Thus, the performance of the antenna is shown to be acceptable between 11.4–13.5 GHz.

Other bandwidth criteria result in the following frequency ranges: the -1 -dB-gain bandwidth is from 12.4–13.5 GHz (8.5%); better than 40% aperture efficiency

is maintained between 12.4–13.3 GHz (7.0%).

The maximum aperture efficiency of 48% is reached at 12.9 GHz and corresponds to a gain reduction of 3.2 dB. The aperture efficiency at 12.4 GHz is 42%, which is 1.2 dB below the 56% efficiency predicted for this frequency in Table 5.1. Some of this discrepancy is associated with the local periodicity assumption of the computational analysis. Additional losses are likely due to the prototype’s construction, most notably from misalignment of the metal layers, an air gap at the aperture, misalignment of the horn, and from the mounting structure that is located near the elements at the edge of the array.

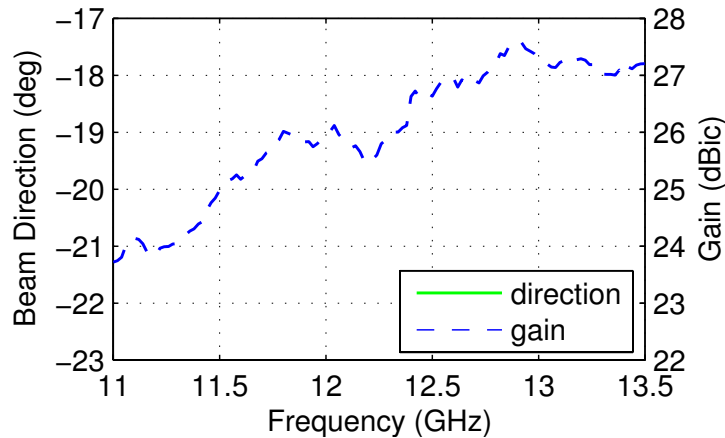


Figure 5.7: Measured beam direction and gain in that direction.

This prototype antenna shows the potential for array lenses to be used as thin, lightweight, high-gain antennas. The maximum measured aperture efficiency is 48% and the measured bandwidth is 17%. At the design frequency, a loss of 1.7 dB is associated with the feed horn; 0.3 dB is lost to direct the major lobe off broadside; 0.6 dB is lost from the lens; and 1.2 dB is lost to other minor factors.

Significant improvements can be made to the aperture efficiency by changing the

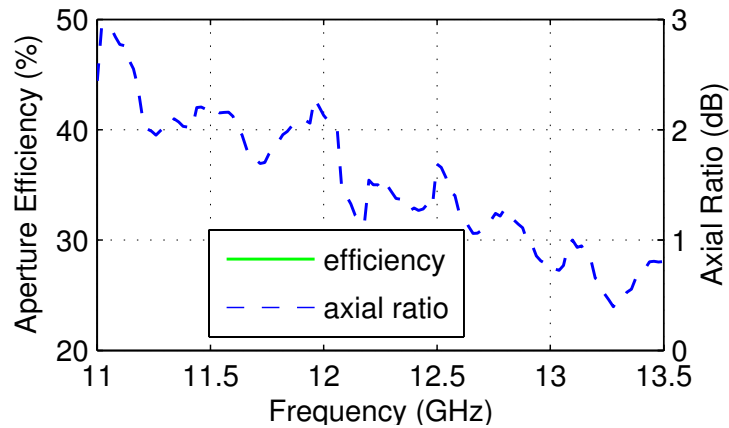


Figure 5.8: Measured aperture efficiency and axial ratio in the beam pointing direction.

feed and the beam pointing direction. The phase error efficiency would be improved by 0.3 dB if the beam was pointed to broadside, i.e., the 0.3 dB scanning loss would be eliminated. Since the horn was not designed to be used as a feed, the loss from the combination of spillover and taper efficiencies (1.7 dB) is quite high. For comparison, the spillover and taper efficiencies of a comparable reflectarray only contribute a loss of 1.1 dB [46]. A horn specifically designed for this lens prototype should provide an improvement of at least 0.6 dB. These two changes have the potential to improve the total aperture efficiency to 60%.

5.1.7 Extrapolating to Larger Arrays

The similarities between the analysis and measurement of the modified convex lens prototype can be extrapolated to predict the radiation characteristics of larger arrays. Importantly, the bandwidth of large arrays will be limited by the array bandwidth rather than the element bandwidth. It will decrease with increasing array size as predicted by Eqn. 2.30. The aperture efficiency should be independent of array size.

None of the five constituents in Table 5.1 are adversely affected for an increased array size. If the aperture efficiency remains constant, the gain should increase proportionally with aperture area (Eqn. 5.13) and the beamwidth should decrease. As discussed in Secs. 4.1.6 and 5.1.4, the cross-polarization discrimination ratio should improve for larger arrays provided that their major lobe points near broadside. This effect should occur at least to the point where the cross polarization level is not due directly to either the feed or the single element properties. Improving the cross-polarization discrimination is equivalent to improving the axial ratio. Note that the focal length of a large array must increase so that the F/D ratio is maintained. A much smaller F/D ratio would increase the perimeter elements' polar incidence angle beyond their practical limit. The side-lobe level should be independent of array size since the magnitude taper of the array weights across the lens is mainly due to the feed. To summarize: a larger array will have increased gain but decreased bandwidth; the aperture efficiency and side-lobe level should be maintained; and the axial ratio should improve.

5.2 Wollaston-Type Prism

The second lens prototype is designed to split an incident wave according to its CP components. The effect is similar to a Wollaston prism, which separates an incident wave (at optical frequencies) into two linearly polarized beams. As shown in Fig. 5.9, the prototype array lens decomposes an incident plane wave into its CP components and redirects the power from each component into two separate beams. The Wollaston prism is typically used at optical frequencies and consists of two

triangular pieces of birefringent material.

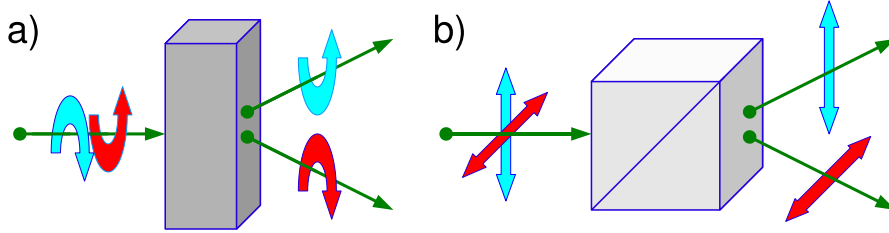


Figure 5.9: Beam splitting action of: a) the array lens described in this section, and b) the Wollaston prism.

Again, the prototype lens contains 349 elements and their rotation is selected to provide a phase shift distribution across the array. The prism effect occurs because of the CP selectivity of the element: S_{21}^{lr} and S_{21}^{rl} have equal magnitudes but opposite phase shifts (Eqn. 4.10). Element rotations are set to:

$$\psi_i = -\frac{\omega_0}{2c} x_i \sin 160^\circ, \quad (5.16)$$

which results in the geometrical pattern shown in the right image of Fig. 5.1. This pattern creates a linear phase shift gradient across the array; however, the gradient will have opposite signs for the scattered fields associated with S_{21}^{lr} and S_{21}^{rl} . This effect is unique to element rotation; it does not occur for other space-fed array phasing techniques.

As mentioned, the prism is designed to split an incident plane wave according to its CP components. When LCP and RCP modes are incident from the same direction, they will scatter into two beams in different directions. Each CP component can be associated with a different array weight. For true plane wave incidence at broadside, the array weight *due to the feed* will be identical for each element. Thus, for ideal elements, the *total* array weight is simply equal to the array weight *provided*

by the element. The incident RCP component will be transmitted as LCP, and the associated array weights will have the following phase shifts:

$$\zeta_i^{lr} = -\frac{\omega_0}{c}x_i \sin 160^\circ, \quad (5.17)$$

Conversely, the incident LCP component will be transmitted as RCP; its array weights will have the opposite phase shifts:

$$\zeta_i^{lr} = +\frac{\omega_0}{c}x_i \sin 160^\circ, \quad (5.18)$$

These two phase distributions will result in two beams on Side 2 of the array. In the array coordinate system (Fig. 4.1) the beams are at (θ_d, ϕ_d) angles of $(160^\circ, 0^\circ)$ and $(160^\circ, 180^\circ)$; in the measurement system they are at $\pm 20^\circ$ azimuth angles. Fields scattered in the $+20^\circ$ beam are mostly associated with the S_{21}^{lr} parameter; fields in the -20° beam are mostly associated with the S_{21}^{rl} parameter.

Because the element is not ideal, scattered fields on Side 2 will also be associated with the S_{21}^{rr} and S_{21}^{ll} parameters. The phase of these parameters is unaffected by element rotation and the fields they scatter will always form beams in the same direction as the incident wave. Ray diagrams associated with these four scattering parameters are shown in Fig. 5.10.

5.2.1 Radiation Pattern Measurement

The prism effect is demonstrated by illuminating the lens with linear polarization and measuring the radiation pattern. To approximate plane wave incidence, the lens is placed in front of a large reflector antenna as shown in Fig. 5.11. A metal sheet with a large circular aperture surrounds the lens to prevent spillover of the incident field from appearing in the measured radiation pattern.

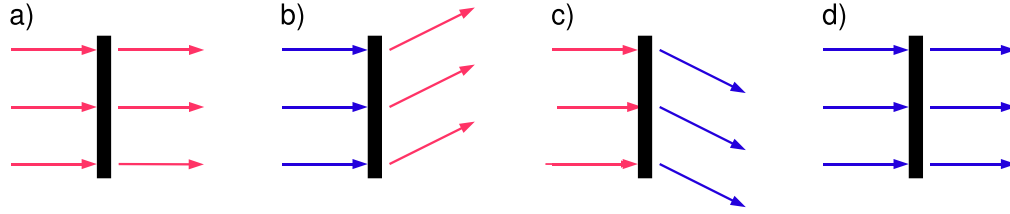


Figure 5.10: Ray diagram representation of the waves transmitted through an infinite array lens configured to split circular polarization. Scattering associated with: a) S_{21}^{rr} , b) S_{21}^{rl} , c) S_{21}^{lr} , d) S_{21}^{ll}

The radiation pattern is measured with the array lens in the aperture, but also with an empty aperture for reference. The azimuth cut of the radiation pattern *without* the lens is shown in Fig. 5.12. In this configuration, the linearly polarized wave simply passes through an electrically large circular aperture. The resulting pattern is linearly polarized with a major lobe at broadside. The CP measurement decomposes the linear polarization into LCP and RCP patterns, which are identical with major lobes at broadside.

The radiation pattern *with* the array lens in the aperture is shown in Fig. 5.13. The major lobe of each polarization points in a different direction. As expected, these directions are at $\pm 20^\circ$ azimuth angles. By comparing Figs. 5.12 and 5.13, it is clear that the array lens has a Wollaston-type prism effect; it splits an incident wave according to its CP components. Note, however, that the gain in the split patterns is 3.0 dB lower than the gain of each polarization through the empty aperture. Furthermore, the half-power beamwidth has increased from 6° to 7° .

The expected gain reduction with the lens in the aperture can be calculated using the analysis from Sec. 5.1.3: 0.3 dB is lost by scanning to 20° ; 0.3 dB is lost in transmission through the lens elements; and 0.2 dB is lost to polarization errors.

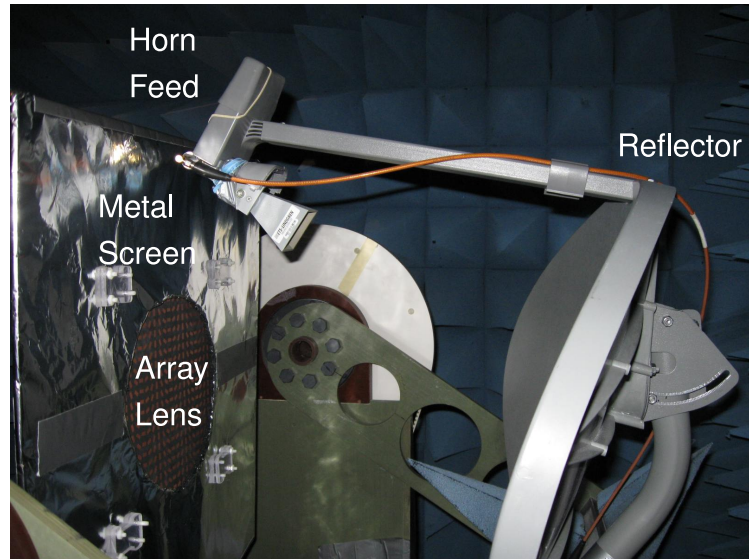


Figure 5.11: The Wollaston-type prism array lens mounted in the anechoic chamber. For the picture, part of the lens is removed so that elements are visible in the aperture.

The measured gain reduction is 3.0 dB; thus, 2.2 dB is lost to other factors, which is 1 dB more than for the modified convex lens. Part of this increase can be attributed to the measurement setup: 15% of the elements lie on the perimeter of the array and are partially covered by the metal screen. If these elements have poor transmission it would explain the increased loss and the change in beamwidth.

Excitation from a linearly polarized plane wave demonstrates the beam splitting effect of the prism lens. When the incident plane wave is circularly polarized, only one beam results. The two beams have different amplitudes when it is elliptically polarized: the major lobe amplitude of the RCP pattern is proportional to the LCP component of the incident field; and conversely, the major lobe amplitude of the LCP pattern is proportional to the RCP component of the incident field.

For broadside incidence, the scattered beams are always pointing in equal but

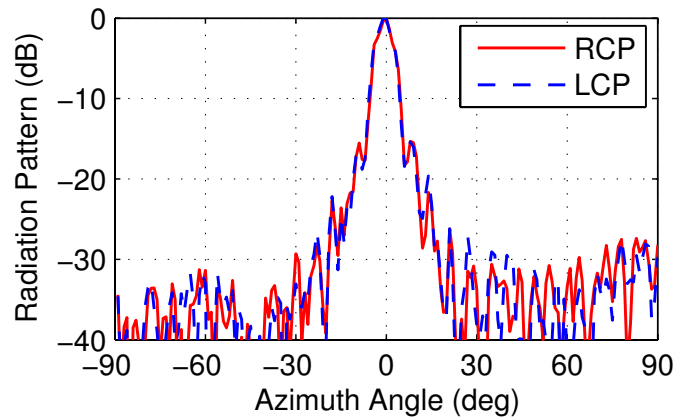


Figure 5.12: Azimuth cut of the radiation pattern without the lens

opposite azimuth directions. If the incidence is from a different azimuth angle, the phase gradient of the incident field projected on the array is added to the gradient provided by the element rotations. For example, incidence at 20° on the prototype lens will create beams at 0° and 43° . By increasing the incidence angle, it may be possible to push one of the beams to an angle beyond the scanning capability of the array element while maintaining the other beam. In this configuration the prism would act as a circular polarization filter.

5.3 Chapter Summary

This chapter has presented two prototype antennas that consist of planar arrays of aperture-coupled stacked-patch elements. Each prototype's design and measurement corresponds to one of the six main contributions of this thesis.

The modified convex lens antenna, presented in Sec. 5.1, creates a narrow beam in the desired off-broadside direction. It demonstrates that focusing lenses for circular polarization can be composed of rotated passive elements. The peak aperture

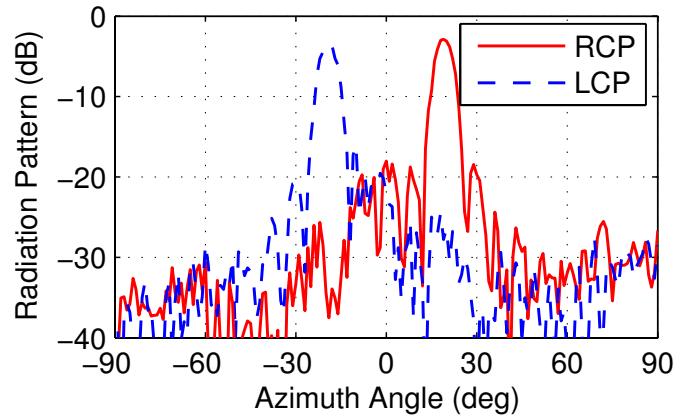


Figure 5.13: Azimuth cut of the radiation pattern through the Wollaston-type prism array lens

efficiency (48%), and cross-polarization discrimination ratio (20 dB) are comparable to those of the relevant prototypes reviewed in Ch. 3. The -3 -dB-gain bandwidth is at least 17%, which is more than that of any published space-fed array prototype fabricated on PCB.

The Wollaston-type prism was presented in Sec. 5.2; it separates an incident wave according to its circular polarization components. The prism effect occurs because the S_{21}^{lr} and S_{21}^{rl} scattering parameters have equal magnitude, but opposite phase shift for any rotational orientation angle. This prototype demonstrates that phase shifts due to element rotation are fundamentally different from those created by varying the element's resonant frequency, and those created using lengths of transmission line. Neither of those other phase shifting techniques can be used to create a Wollaston-type prism effect.

Both antennas are electrically large, but the elements contain electrically small features. This range of scale makes it difficult to simulate the entire array. A mod-

eling technique that breaks the analysis into smaller tasks is presented in Sec. 5.1.1. It assumes local periodicity for each element of the array. The radiation pattern of the modified convex lens prototype was calculated using this technique in Sec. 5.1.2. It predicts the major lobe of the measured radiation pattern, but not the side-lobe level. The aperture efficiency was predicted by calculating five efficiency constituents in Sec. 5.1.3. An explanation for the 1.2 dB difference between calculated and measured aperture efficiency was offered in Sec. 5.1.6. This modeling technique is also one of main contributions of this thesis. It was presented in a general way so that any size of array, or any lens configuration can be analyzed using a small set of single element simulations.

Three main contributions were presented in Ch. 4 and three were presented in this chapter. These six contributions represent the advance in knowledge I have made to the field of antenna engineering. The next chapter concludes this document. The contributions are summarized in the context of the thesis goals that were outlined in Sec. 1.2.

Chapter 6

Future Work, Contributions, and Conclusion

6.1 Future Work

Although this document presents a completed project, it has generated some additional ideas. In this section, I suggest some options for interesting future work in this area. The research I foresee can be divided into three categories: element modifications, additional antenna prototypes, and improvements to the simulation technique.

Possible element modifications are:

- Increasing the design frequency. This can be done by scaling the element or by using the design guidelines in Sec. 4.3.6. This work has shown successful operation in the Ku band (12–18 GHz), it could be interesting to demonstrate operation in the Ka band (26.5–40 GHz).
- Optimizing the element at a 24° polar incidence angle. In Ch. 4, the element was numerically optimized for broadside incidence, and its performance slowly degrades as the incidence angle increases. For the modified convex lens prototype, only one element has broadside incidence; the median polar incidence angle is 24° . A small improvement in aperture efficiency could be achieved by designing the element for the median incidence angle.
- Designing an element that is not symmetrical about the ground plane. The element presented in this work has symmetrical stacked patches on either side

of the ground plane. An asymmetric element may be useful. It could reduce the number of metal layers if different resonances were created on either side. Furthermore, it would allow the inner- and outer-surface radiators to have individual designs, e.g., the inner-surface radiator could be designed for the large range of incidence angles from the feed, but the outer-surface radiator could be optimized at the desired beam direction.

- Developing an actively rotating element. The elements in this work are passive and create fixed-beam arrays. However, actively rotating elements would provide controllable phase shift and create scanning or pattern-reconfigurable arrays. The element can be physically rotated using micromotors, or it can be effectively rotated using electronic switches.

Suggested array prototypes include:

- A larger array. In Sec. 5.1.7, predictions were made regarding the bandwidth, aperture efficiency, gain, and axial ratio of larger arrays. It would be interesting to test these predictions in a large anechoic chamber or an antenna range.
- A contoured beam array. Since this work is most applicable to direct broadcasting satellite antennas, it would be appropriate to fabricate a prototype contoured beam array. The beam contour could be designed for a specific geographic coverage area.
- A conformal array. The prototype arrays in this work are both planar; however, only the 40° incidence angle limit restricts the possible array geometry. Arrays using multiple planar panels at various angles, or elements on curved surfaces could be used to conform the array to a unique shape.

- A custom-designed feed. The spillover and taper efficiencies of the feed horn reduced the potential gain of the modified convex lens by 1.7 dB. Although this is quite large, it was expected as the horn was not designed for use as a feed antenna. A custom-designed horn should improve the aperture efficiency. Other CP feed types, such as a patch, spiral, or helical antenna, could also be interesting.
- A CP filter using a Wollaston-type prism. At the end of Sec. 5.2.1, the possibility of using the element rotation technique to design a filter was presented. It would be interesting to develop this concept.

Potential enhancements to the simulation technique are:

- Improved simulation of the perimeter elements. Each element was modeled assuming local periodicity, which is a reasonable approximation for the elements near the centre of the array, but not for those on the edge. It would be useful to model the perimeter elements with their appropriate surroundings.
- Actual simulation of the coupling between neighbouring elements. Although modeling each element assuming local periodicity is a reasonable approximation for most of the elements, it does not consider the change in coupling when the neighbouring elements have different rotation angles. Other simulation techniques, including the Surrounded Element Approach [54], have been proposed to calculate a scattering matrix that considers the neighbouring elements. It would also be interesting to know the severity of the error introduced by the local periodicity assumption.
- Full prototype simulation. Specific full-wave simulation codes, such as [55],

are currently being developed to analyze entire array lens and reflectarray structures. For layered, planar structures, these codes will be simple enough to analyze large antennas with fine geometrical details. The assumption of local periodicity will no longer be required and the lens can be more accurately modeled. It would be interesting to perform this simulation and compare the radiation pattern with the measured pattern and with the pattern calculated assuming local periodicity.

6.2 Goals and Contributions

In Sec. 1.2, the goals of this research were outlined as five investigative questions and two engineering design objectives. These questions and design objectives led to the six contributions I have made to antenna engineering. The questions inquired about the properties of circularly polarized array lens antennas—specifically into the concept of using element rotation to select the phase of the array weights. The answers to these questions were presented throughout the thesis, and they are summarized in the following list:

- *Both qualitatively and analytically, how does rotation create phase shift for an array element?* Qualitatively, the phase shift occurs because the handedness of circular polarization is changed. When the element is rotated, the inner surface radiator receives a phase advanced signal for an incident RCP wave. The outer surface radiator transmits a phase advanced signal only if the wave is scattered as LCP. Thus, the phase is advanced twice and the relative phase shift between elements is twice the relative rotation angle. The outer surface

radiator transmits a phase delayed signal if the wave is scattered as RCP; in this case, the phase is advanced once but delayed once resulting in no net phase shift. An analytical formulation of the phase shift was derived by treating a single element as a periodic surface from which only certain modes can scatter. Using rotational and coordinate transformations, it was shown that some of the CP scattering parameters are phase shifted by rotation.

- *What limits the bandwidth for this type of element?* The element bandwidth is limited by either the transmission bandwidth or the phase bandwidth. The transmission bandwidth is the range of frequencies over which both linear polarizations are transmitted through the element; the phase bandwidth is the range over which the phase shift difference between linear polarizations is close to 180° .
- *What effect does the angle of incidence have on the element response?* The aperture-coupled stacked-patch element was designed to maximize the desired scattering parameter at broadside incidence. For other incidence angles, that parameter's magnitude is reduced and its phase does not exactly satisfy the 2:1 ratio of phase to rotation. However, it was shown that the results are acceptable for polar incidence angles up to 40° .
- *What is the effect of scanning the array away from the direct transmission direction?* The array weights of the modified convex lens scan the beam to a direction 20° from broadside. Two effects were observed. First, the aperture efficiency is reduced as the projected area in the beam direction is less than the physical area of the aperture. This effect is common to all aperture antennas. Secondly, circular currents on a planar surface combine into elliptically polar-

ized beams off broadside. This effect increases the axial ratio as the beam is scanned away from broadside.

- *Are there any additional advantages or disadvantages to the rotation technique?*

This work has uncovered one significant advantage of the rotation technique: its cross-polarization selectivity. This selectivity causes the phase shift to be equal but opposite for each handedness of incident polarization. For a focusing lens, this effect will improve the axial ratio of the major lobe. The desired polarization is collimated into a high-gain beam, but the cross polarization remains spatially diffused. The cross-polarization selectivity can also be exploited to create a Wollaston-type prism effect.

The engineering goals of this thesis were selected to demonstrate that lenses for circular polarization can consist of planar arrays of rotated elements. The accomplishment of these goals was as follows:

- *Develop a suitable element that can be fabricated using printed circuit technology.* The aperture-coupled stacked-patch element was shown to be suitable for incidence angles up to 40° and over an 18% bandwidth. It is fabricated using photo-lithographic etching and layer bonding, which are both standard processes from printed circuit technology.
- *Design, analyze, fabricate, and test a prototype array.* A modified convex lens was designed, analyzed, fabricated and tested. The design process results from the simplicity of the 2:1 ratio between phase shift and element rotation. It can be easily modified for any desired radiation pattern. Analysis of the prototype was performed using a custom three-part computational analysis. The gain,

radiation pattern, axial ratio, and bandwidth were measured in an anechoic chamber.

In answering these questions and completing the design goals, six contributions were made:

1. The derivation of the circular polarization scattering parameters for a rotated element (Sec. 4.1.1). This identified the parameters that are phase shifted by rotation.
2. An analysis of the element bandwidth (Sec. 4.2). This analysis helps in designing a suitable lens element.
3. The design of the aperture-coupled stacked-patch lens element (Sec. 4.3). This invention demonstrates the feasibility of a lens using rotated elements.
4. The modified convex lens prototype (Sec. 5.1). It demonstrates the versatility and practicality of a focusing lens using rotated elements.
5. The simulation technique that was applied to the prototype (Sec. 5.1.1). Since this technique can be used for much larger arrays, it allows for a quick prediction of the antenna's properties.
6. The Wollaston-type prism prototype (Sec. 5.2). It demonstrates the cross-polarization selectivity of rotated elements.

6.3 Conclusion

Lenses can be used to redirect, converge, or diverge electromagnetic radiation. In this thesis, lenses using planar arrays of rotated passive elements were studied. Two prototype lenses were measured: one was designed to converge radiation from a feed

horn, and the other was designed to redirect plane wave radiation.

In communication systems design, there is a choice of technologies for large, fixed-beam antennas. The work presented in this thesis has shown that an array lens antenna phased by rotated passive elements is a suitable choice for certain applications. Its electromagnetic properties, including radiation pattern, gain, side-lobe level, bandwidth, and aperture efficiency are all comparable to those of existing technologies. The important advantages it provides are its mechanical properties. The prototype lens is neither bulky nor heavy: is 7.1 mm thick and it weighs 0.91g/cm². The packed volume of a large array can be small if the aperture consists of multiple planar panels. The mass-production costs are low: it consists of readily available low-loss PCBs and dielectric foam, and it is manufactured using photo-lithographic etching and layer bonding. No via holes, lumped components, or tedious assembly is required. This type of antenna is tolerant to manufacturing errors: each element's transmission coefficient has only small variation with misaligned layers. Furthermore, an array lens is more tolerant to deviations in surface flatness than a reflectarray. By providing these benefits without compromising the electromagnetic properties, the flat lens presented in this thesis is a competitive solution for large, fixed-beam antennas.

Bibliography

- [1] R. Phillion and M. Okoniewski, “Array lens antenna using element rotation,” in *Proc. 13th International Symposium on Antenna Technology and Applied Electromagnetics and the Canadian Radio Science Meeting ANTEM/URSI 2009*, 15–18 Feb. 2009, pp. 1–4.
- [2] —, “Bandwidth of circularly polarized reflectarray and array lens elements,” in *Proc. IEEE Antennas and Propagation Society International Symposium APSURSI '09*, 1–5 June 2009, pp. 1–4.
- [3] —, “An array lens for circular polarization with emphasis on aperture efficiency,” in *Proc. 4th European Conference on Antennas and Propagation EuCAP 2010*, 2010, pp. 1–4.
- [4] —, “Analysis of a transmit-array antenna for circular polarization,” in *Proc. 26th International Review of Progress in Applied Computational Electromagnetics*, 2010, pp. 1–4.
- [5] —, “Using an array lens as a circular polarization splitting prism,” in *Proc. IEEE Antennas and Propagation Society International Symposium APSURSI '10*, 2010, pp. 1–4.
- [6] —, “Lenses for circular polarization using planar arrays of rotated passive elements,” *IEEE Trans. Antennas Propagat.*, 2010, accepted for publication.
- [7] C. Balanis, *Antenna Theory: Analysis and Design*, 2nd ed. John Wiley & Sons, 1997.

- [8] J. L. Volakis, Ed., *Antenna Engineering Handbook*, 4th ed. McGraw Hill, 2007.
- [9] J. D. Kraus and R. Marhefka, *Antennas: For All Applications*. McGraw Hill, 2002.
- [10] T. A. Milligan, *Modern Antenna Design*, 2nd ed. John Wiley & Sons, 2005.
- [11] P. Hannan and M. Balfour, "Simulation of a phased-array antenna in waveguide," *IEEE Trans. Antennas Propagat.*, vol. 13, pp. 342–353, May 1965.
- [12] J. Huang and J. A. Encinar, *Reflectarray Antennas*. John Wiley & Sons, 2008.
- [13] A. W. Rudge, K. Milne, A. D. Olver, and P. Knight, *Handbook of Antenna Design*. IEEE, 1982.
- [14] D. Berry, R. Malech, and W. Kennedy, "The reflectarray antenna," *IEEE Trans. Antennas Propagat.*, vol. 11, pp. 645–651, 1963.
- [15] S. Targonski and D. Pozar, "Design of wideband circularly polarized aperture-coupled microstrip antennas," *Antennas and Propagation, IEEE Transactions on*, vol. 41, no. 2, pp. 214–220, feb 1993.
- [16] E. M. Slayter and H. S. Slayter, *Light and Electron Microscopy*. Cambridge University Press, 1992.
- [17] R. M. A. Azzam and N. Bashara, *Ellipsometry and Polarized Light*. North-Holland, 1977.
- [18] H. Tompkins and E. A. Haber, *Handbook of Ellipsometry*. William Andrew, 2005.

- [19] A. K. Bhattacharyya, *Phased Array Antennas*. John Wiley & Sons, Inc., 2006.
- [20] A. Marston, “Antenna system having beam control members consisting of array of spiral elements,” U.S. Patent 3,045,237, 1962.
- [21] R. Brown and R. Dodson, “Parasitic spiral arrays,” in *IRE International Convention Record*, vol. 8, Mar 1960, pp. 51 – 66.
- [22] D. Nakatani and J. Ajioka, “Lens designs using rotatable phasing elements,” in *Proc. Antennas and Propagation Society Int. Symp*, vol. 15, 1977, pp. 357–360.
- [23] H. Kaouach, L. Dussopt, R. Sauleau, and T. Koleck, “X-band transmit-arrays with linear and circular polarization,” in *Proc. 4rd European Conference on Antennas and Propagation EuCAP 2010*, 2010.
- [24] D. McGrath, “Planar three-dimensional constrained lenses,” *IEEE Trans. Antennas Propagat.*, vol. 34, no. 1, pp. 46–50, 1986.
- [25] D. Pozar, “Flat lens antenna concept using aperture coupled microstrip patches,” *Electronics Letters*, vol. 32, no. 23, pp. 2109–2111, 1996.
- [26] K.-W. Lam, S.-W. Kwok, Y. Hwang, and T. K. Lo, “Implementation of transmitarray antenna concept by using aperture-coupled microstrip patches,” in *Proc. Asia-Pacific Microwave APMC '97*, vol. 1, 1997, pp. 433–436.
- [27] S. Datthanasombat, J. Prata, A., L. R. Arnaro, J. A. Harrell, S. Spitz, and J. Perret, “Layered lens antennas,” in *Proc. IEEE Antennas and Propagation Society Int. Symp*, vol. 2, 2001, pp. 777–780.

- [28] C. G. M. Ryan, M. R. Chaharmir, J. Shaker, J. R. Bray, Y. M. M. Antar, and A. Ittipiboon, "A wideband transmitarray using dual-resonant double square rings," *IEEE Trans. Antennas Propagat.*, vol. 58, no. 5, pp. 1486–1493, 2010.
- [29] N. Gagnon, A. Petosa, and D. A. McNamara, "Thin microwave phase-shifting surface lens antenna made of square elements," *Electronics Letters*, vol. 46, no. 5, pp. 327–329, 2010.
- [30] R. Shibayama, H. Deguchi, and M. Tsuji, "Flat thin polarizer-lens based on multiple resonance behavior," in *Proc. IEEE Antennas and Propagation Society International Symposium APSURSI '10*, 2010, pp. 1–4.
- [31] P. Padilla, A. Munoz-Acevedo, and M. Sierra-Castaner, "Passive microstrip transmitarray lens for ku band," in *Proc. 4rd European Conference on Antennas and Propagation EuCAP 2010*, 2010.
- [32] J. Lau and S. Hum, "A low-cost reconfigurable transmitarray element," in *Proc. IEEE Antennas and Propagation Society International Symposium APSURSI '09*, 2009, pp. 1–4.
- [33] A. Munoz-Acevedo, P. Padilla, and M. Sierra-Castaner, "Ku band active transmitarray based on microwave phase shifters," in *Proc. 3rd European Conference on Antennas and Propagation EuCAP 2009*, 2009, pp. 1201–1205.
- [34] F.-C. E. Tsai and M. E. Bialkowski, "Investigations into the design of a spatial power combiner employing a planar transmitarray of stacked patch antennas," in *Proc. MIKON-2004 Microwaves, Radar and Wireless Communications 15th Int. Conf*, vol. 2, 2004, pp. 509–512.

- [35] S. Ortiz, J. Hubert, L. Mirth, E. Schlecht, and A. Mortazawi, “A high-power ka-band quasi-optical amplifier array,” *IEEE Trans. Microwave Theory Tech.*, vol. 50, no. 2, pp. 487–494, 2002.
- [36] S. Hollung, A. Cox, and Z. Popovic, “A bi-directional quasi-optical lens amplifier,” *IEEE Trans. Microwave Theory Tech.*, vol. 45, no. 12, pp. 2352–2357, 1997.
- [37] A. Fox, “An adjustable waveguide phase changer,” *Proc. Institute of Radio Engineers*, vol. 35, pp. 1489–1498, Dec 1947.
- [38] A. Martynyuk, N. Martynyuk, S. Khotiaintsev, and V. Vountesmeri, “Millimeter-wave amplitude-phase modulator,” *IEEE Trans. Microwave Theory Tech.*, vol. 45, pp. 911–917, Jun 1997.
- [39] H. Phelan, “Spiraphase- a new, low cost, lightweight phased array,” *Microwave J.*, vol. 19, pp. 41–44, Dec 1976.
- [40] J. Huang and R. Pogorzelski, “A Ka-band microstrip reflectarray with elements having variable rotation angles,” *IEEE Trans. Antennas Propagat.*, vol. 46, pp. 650–656, May 1998.
- [41] A. Martynyuk and J. Martinez Lopez, “Reflective antenna arrays based on shorted ring slots,” in *IEEE Int. Microwave Symp. Digest, MTT-S 2001*, vol. 2, May 2001, pp. 1379–1382.
- [42] B. Subbararo, V. Fusco, and R. Cahill, “Spatial phase shifter for reflect array

- (circular polarisation) applications,” in *Proc. 7th IEEE High Frequency Post-graduate Student Colloquium*, V. Fusco, Ed., 2002, p. 6.
- [43] —, “Rotary spatial phase shifter for reflectarray beamsteering,” in *Proc. Int. Conf. on Antennas and Propagation, ICAP 2003*, Exeter, UK, 2003, pp. 341–344.
- [44] B. Strassner, C. Han, and K. Chang, “Circularly polarized reflectarray with microstrip ring elements having variable rotation angles,” *IEEE Trans. Antennas Propagat.*, vol. 52, pp. 1122–1125, Apr 2004.
- [45] A. Martynyuk, J. Lopez, and N. Martynyuk, “Spiraphase-type reflectarrays based on loaded ring slot resonators,” *IEEE Trans. Antennas Propagat.*, vol. 52, pp. 142–153, Jan 2004.
- [46] A. Yu, F. Yang, A. Elsherbeni, and J. Huang, “An x-band circularly polarized reflectarray using split square ring elements and the modified element rotation technique,” in *Proc. IEEE Antennas and Propagation Society International Symposium AP-S 2008*, 2008, pp. 1–4.
- [47] A. Martynyuk, J. Martinez Lopez, and N. Martyunuk, “Reflective passive phased array with open polarization phase shifters,” in *Proc. IEEE Int. Symp. on Phased Array Systems and Technology*, Oct 2003, pp. 482–487.
- [48] H. Legay, B. Pinte, M. Charrier, A. Ziaei, E. Girard, and R. Gillard, “A steerable reflectarray antenna with MEMS controls,” in *Proc. IEEE Int. Symp. on Phased Array Systems and Technology*, Oct 2003, pp. 494–499.

- [49] V. Fusco, “Mechanical beam scanning reflectarray,” *IEEE Trans. Antennas Propagat.*, vol. 53, pp. 3842–3844, Nov 2005.
- [50] R. Phillion, “A microfabricated rotating element for reconfigurable reflectarray antennas,” Master’s thesis, University of Calgary, 2007.
- [51] M. Alvarez-Folgueiras, J. A. Rodriguez-Gonzalez, and F. Ares-Pena, “Pencil beam patterns obtained by a planar array of parasitic dipoles fed by only one active element,” in *Proc. 4rd European Conference on Antennas and Propagation EuCAP 2010*, 2010.
- [52] Z.-H. Wu and W.-X. Zhang, “Broadband printed compound air-fed array antennas,” *IEEE Antennas Wireless Propagat. Lett.*, vol. 9, pp. 187–190, 2010.
- [53] Y. Lo and S. Lee, *Antenna Handbook: Applications*. Chapman and Hall, 1993.
- [54] M.-A. Milon, R. Gillard, D. Cadoret, and H. Legay, “Comparison between the infinite array approach and the surrounded-element approach for the simulation of reflectarray antennas,” in *Proc. IEEE Antennas and Propagation Society International Symposium 2006*, 2006, pp. 4339–4342.
- [55] P. De Vita, F. De Vita, A. Di Maria, and A. Freni, “An efficient technique for the analysis of large multilayered printed arrays,” *IEEE Antennas Wireless Propagat. Lett.*, vol. 8, pp. 104–107, 2009.